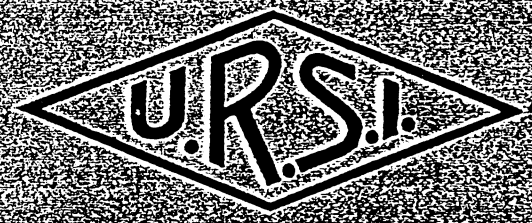# International

Reference

Ionosphere

1990

U.R.S.I.

COSPAR

Dieter Bilitza

with contributions by:

K. Rawer, L. Bossy, I. Kutiev
K. -I. Oyama, R. Leitinger
and E. Kazimirovsky

URSI/COSPAR Task Group on the International Reference Ionosphere

Steering Committee

L. Bossy (Belgium), *Chairman*
T. L. Gulyaeva (U.S.S.R.), D. Bilitza (U.S.A.), *Vice-Chairmen*

Executive Members

D. N. Anderson (U.S.A.)
P. Bradley (U.K.)
A. D. Danilov (U.S.S.R.)
K. Rawer (F.R.G.)
J. Taubenheim (G.D.R.)

Ordinary Members

A. D. Alcaydé (France)
K. Bibl (U.S.A.)
L. H. Brace (U.S.A.)
K. S. W. Champion (U.S.A.)
Y. K. Chasovitin (U.S.S.R.)
M. Friedrich (Austria)
G. S. Ivanov-Kholodny (U.S.S.R.)
E. Kazimirovsky (U.S.S.R.)
E. Kopp (Switzerland)
L. F. McNamara (Australia)
N. Matuura (Japan)
A. P. Mitra (India)
B. C. N. Rao (India)
B. W. Reinisch (U.S.A.)
M. J. Rycroft (U.K.)
K. Serafimov (Bulgaria)
J. J. Sojka (U.S.A.)
V. Wickwar (U.S.A.)

International Reference

Ionosphere 1990

Dieter Bilitza

Science Applications Research
Lanham, Maryland 20706, U.S.A.

November 1990

Contents

This document describes the International Reference Ionosphere 1990 (IRI-90). It is intended as a guide and handbook for the experienced as well as the new IRI user. IRI models are established by a joint working group of the Committee on Space Research (COSPAR) and the International Union of Radio Science (URSI). The composition of the COSPAR/URSI Working Group on IRI is listed on the inside front cover.

Close ties exist to the URSI Working Group G.3 on Ionospheric Modeling (C. M. Rush, U.S.A., Chairman) and G.4 on Ionospheric Informatics (B. W. Reinisch, U.S.A., Chairman) and to the SCOSTEP (Scientific Committee on Solar-Terrestrial Physics) Working Group on an Aeronomical Reference Ionosphere (R. W. Schunk, U.S.A., Chairman).

IRI describes monthly averages of the electron density, electron temperature, ion temperature, and ion composition in the altitude range from 50 km to 1000 km for magnetically quiet conditions in the non-auroral ionosphere.

Almost a decade has passed since the last comprehensive IRI handbook was published: IRI-79 was described in *Report UAG-82* of the World Data Center A for Solar-Terrestrial Physics (Rawer et al., 1981). Meanwhile, the IRI model has been significantly improved with ground and space data collected in the seventies. Work and studies that led to several IRI updates were presented and discussed at the annual IRI workshops and are published in a series of issues of *Advances in Space Research*: Volume 2, No. 10, 1982; Volume 4, No. 1, 1984; Volume 5, No. 7 and No. 10, 1985; Volume 7, No. 6, 1987; Volume 8, No. 4, 1988; Volume 10, No. 8 and No. 11, 1990. The list of contents of these reports is reproduced in Chapter 5.

The IRI-90 handbook summarizes the most important improvements and new developments. It includes a text part, a portion that explains the IRI formulas and expressions, and finally a collection of figures generated with IRI-90.

An interactive driver program for IRI-90 was developed at the National Space Science Data Center (NSSDC) and is distributed (together with the IRI-90 FORTRAN computer code and coefficients) on magnetic tape, on diskette, and on line on the Space Physics Analysis Network (SPAN) and connected computer networks. The diskette version can be executed on IBM compatible personal computers (XT, AT), no math co-processor required*.

Since 1988, IRI has also been part of NSSDC's Online Data and Information Service (NODIS), which can be accessed from a remote SPAN node: (1) SET HOST NSSDCA, (2) USERNAME=NODIS, (3) choose the GEOPHYSICAL MODELS option, and (4) follow the prompts and menus. You can (i) run the program, (ii) read the documentation, or (iii) get instructions on how to copy the IRI code and coefficients to your account.

IRI-90 on tape or diskette can be ordered from—

- For U.S. researchers:

  National Space Science Data Center
  Code 933.4
  Goddard Space Flight Center
  Greenbelt, Maryland 20771
  Telephone: (301) 286-6695
  Telex: 89675 NASCOM GBLT
  TWX: 7108289716
  FAX: (301) 286-4952
  SPAN: NSSDCA::REQUEST

- For researchers residing outside the U.S.:

  World Data Center A for Rockets and Satellites
  Code 930.2
  (Address same as above.)

Publication of this document was made possible through the support and encouragement of Joseph H. King and through the dedicated and untiring efforts of Miranda Knowles, Lynda Williams, and Maria Walters.

---

* With co-processor, the execution speed increases by a factor of ten. Recompilation is necessary if the user has a system with co-processor and wants to take advantage of the faster speed.

Chapter 2   History and New Developments

Contents

2.1 History of the International Reference Ionosphere

K. Rawer
Herrenstr. 43, 7806 March
Federal Republic of Germany

L. Bossy
Université Catolique de Louvain
174, avenue W. Churchill, 1180 Bruxelles
Belgium

Radio-observations of the very first satellites yielded some very important results concerning the upper atmosphere. Orbital period determinations via radio-location showed that temperature and density variations in the upper atmosphere are much greater than expected. Therefore, the newly-founded Committee on Space Research (COSPAR) decided that a set of empirically based tables describing these findings should be established. This task was considered of such high importance that a commission of specialists was established to carry it out. This group in 1961 presented its findings under the name of COSPAR International Reference Atmosphere (CIRA). The collection was widely used by the scientific community. Taking account of the increasing amount of measured data followed up by an increasing number of theoretical approaches, the continuous work of the CIRA Task Group culminated in the release of three more CIRAs in 1965, 1972, and 1986.

Realizing the success of CIRA, S. Bowhill proposed a few years later to establish a comparable reference for the ionized constituents of the atmosphere, to be called International Reference Ionosphere. According to the original terms of reference, it should contain empirically based tables describing monthly median vertical profiles of the main parameters of the ionospheric plasma. Like CIRA, IRI should be usable as a standard reference for the design of experiments, the estimation of environmental and other effects, for checking theories, etc. The profiles should be provided for suitably chosen locations, hours, seasons, and levels of solar activity. In contrast to theoretical models, the IRI should combine approved experimental results so as to be a useful reference with no dependence on theoretical assumptions.

To take care of this new task, COSPAR in 1968 established the "Task Group on IRI" and nominated K. Rawer for chairman. This group was given the task of promoting and coordinating the international efforts toward the goal described in the above terms of reference. In 1969, the International Union of Radio Science (URSI) decided to concur with COSPAR in the project. A preliminary set of tables (for two locations, noon and midnight, three seasons, and two levels of solar activity) was presented as an example to the URSI General Assembly 1975 in Lima, Peru.

The Task Group made two decisions at the very beginning of its work:

(1) Since most users have access to computer facilities, the results should be presented as a computer code rather than as a set of printed tables. Tables and figures could then be produced with this code.

(2) The peak of the ionosphere should not be modeled independently but should be determined by an existing computer code published in 1967 by the Comite Consultatif International des Radiocommunications (CCIR).

The CCIR code is based on a large set of measurements made by ionosonde technique at more than a hundred stations worldwide. This data base, however, contains large gaps over the oceans. In order to fill these gaps, Jones and Gallet (1965) had introduced a particular, coordinate-dependent, interpolation system that was bound to geographic coordinates. To give a more coherent picture, the CCIR version applies another, special latitudinal coordinate (MODIP) that was proposed by Rawer (1963).

The terms of reference asked for four parameters to be represented in IRI, namely, electron density, electron and ion temperature, and (positive) ion densities. In order to reach consistency with the independently obtained electron densities, the ion densities should be given as relative, not absolute, values. Consistency was also asked for between the plasma temperatures and the CIRA neutral temperature.

As a general philosophy a data set, before being introduced into the system, had to be critically evaluated by the experts. Comparing results of different techniques was one way of checking data reliability, a powerful one as was found out. In fact, critical comparison of different measuring methods turned out to become a major IRI task. For example, a special meeting on "Methods of Measurements and Results of Lower Ionosphere Structures" was initiated by the group and was held in 1973 at Konstanz, Federal Republic of Germany. With the guidelines established during the meeting in mind and in broad international cooperation, a great effort was started to gather relevant data from different techniques.

At the onset of IRI work, it had been expected that the amount of accessible and reliable data would be rather large for electron densities, much smaller for temperatures, and rather poor for ion composition. In general, this was found to be the case. However, even the electron density profile data showed rather important and unexpected gaps. In spite of the existence of an enormous amount of evaluated ionogram parameters, true height profiles were only available for a small number of stations providing by no means a worldwide coverage. The inversion technique, needed to obtain true height profiles, had been applied only at very few places at temperate latitude. Even there, some uncertainty remained because of the E-F-valley problem (Gulyaeva et al., 1990). Several stations run by U.S. institutions had produced so-called "composite profiles" obtained with an artificial "median

ionogram" (established month by month and hour by hour). Though the reliability of these results might be questionable, they were the only available input at lower latitudes. Also, the polar caps were de facto excluded because of the lack of specific information and because of the great variability encountered in this region. It was felt that under the extreme conditions in the polar caps the CCIR maps, which are based on monthly median station data, are unable to produce a representative picture.

As for the topside, mainly two sources of information were available at the time, namely, incoherent scatter observations (unfortunately at few stations only) and topside sounder profiles. In situ measured plasma densities could be used only for checking purposes. A very large number of topside ionograms taken by the two Alouette satellites had been inverted to density profiles. Unfortunately, an inquiry showed that these were incomplete because the peak electron density value was regularly missing. Thus, regrettably, the many profiles in the archives were not usable for the IRI purpose. Later Bent and Llewellyn (1973) established an empirical model description based mainly on about 10,000 topside ionograms obtained by Alouette above North and South America. While the influences of solar activity and F-peak density are given by simple formulas in this model, the latitudinal variation is described discontinuously considering only three geographic ranges. S. K. Ramakrishnan produced a continuous description for the Llewellyn and Bent (1973) model. There remained, however, serious problems in the region around the geomagnetic equator where the original description does not admit an explicit dependence on latitude (Bilitza, 1985a, 1986).

For the height of the F2-peak, $hmF2$, reliable data are obtained by the incoherent scatter technique; however, only a rather small number of stations operate worldwide. Fortunately, in view of propagational applications, ionosonde stations had regularly determined a parameter, $M(3000)F2$, which has some relation with $hmF2$. A large and worldwide thesaurus for this parameter was readily available in the form of the CCIR numerical maps similar to the CCIR peak density maps. From a compilation of ionogram data (under some simplifying assumptions) Shimazaki (1955) had found a linear relationship between the peak height $hmF2$ and $M(3000)F2$, a relationship that was later improved by different authors (Bradley and Dudeney, 1973; Bilitza et al., 1979). The improved formulas take account of additional parameters which influence the $hmF2$-$M(3000)F2$ relationship, in particular refraction in the E-region. With such relations the $M(3000)F2$ maps could be transformed into $hmF2$ maps. The results obtained by incoherent scatter had been taken into account for the improvement introduced by Bilitza et al. (1979).

Particular problems were encountered in comparisons of measurements in the lowest ionosphere (below 100 km) that had been obtained with different techniques. The data were so widely different that a special symposium was held (see above) in order to reach an agreement about general guidelines (Rawer, 1974). It was stated that in situ measurements, when combined

with radio propagation measurements between ground and rocket, would be used as the primary input. A compilation of acceptable D-region rocket data was made by Mechtly and Bilitza (1974). For the nighttime lower E-region and valley two differing compilations were available from Maeda (1969, 1970, 1971, 1972) and Soboleva (1972, 1973). Comparing both with Schumann resonances, H. G. Booker gave a strong vote in favor of the Maeda model.

The full (vertical) profile of plasma density was described by a set of mathematical expressions, each valid in a certain height range. This rather complex system allowed a correct representation of the most important inputs, like the peak densities of the main layers. On the other hand, it was not well suited for "full wave" computations. For such computations (at extremely low frequencies), Booker (1977) proposed the use of fully analytic functions of a type that P. S. Epstein had defined in the thirties. His proposal was, in fact, used in the topside description but for good reasons could not be realized for the full profile at that time.

At least by day the electron temperature can be much higher than that of the ions, the latter being also less variable. Ion temperature data observed with the retarding potential analyzer technique by Dumbs et al. (1979) were accepted as reliable inputs together with ground-based measurements made at a few places by the incoherent scatter technique. The in situ results were used to derive the latitudinal variation between the incoherent scatter stations. The difference to the lower CIRA neutral temperature values becomes quite appreciable above 400 km. Near the 100 km level agreement of both temperatures (as requested by COSPAR) was arranged for within the ion temperature formula.

The same data sources were used for the electron temperatures. The latitudinal variation was mainly taken from a compilation of data measured aboard the AEROS satellites (Spenner and Plugge, 1979). Later Bilitza et al. (1985) improved the temperature model by introducing Langmuir probe data compiled by Brace and Theis (1981) from the AE-C and ISIS 1 and 2 satellite missions. It is well documented that the electron temperature and density are closely anti-correlated in the daytime ionosphere (e.g., Bilitza, 1975; Brace and Theis, 1978). Therefore, in the formulas used at first, the electron temperature was coupled with the actual electron density. Later it was found that for monthly medians a correlation between the temperature and density profile was not meaningful. Density and temperature profiles were, therefore, established independently from the relevant monthly median data. In case, however, actual density profiles for a specific time and location are at hand, it is recommended to apply a correction to the median temperature profile via an empirical (inverse) relation specified in IRI (Bilitza et al., 1985).

The data base for (positive) ion composition was rather poor at the time. Most of the published rocket or satellite data had been given as absolute densities and did not provide the total plasma density needed to determine the relative ion composition. Further, a large set of simultaneous measurements with mass

spectrometers and a retarding potential analyzer (RPA) aboard the AEROS satellites had shown that while the spectral resolution is much better with mass spectrometers, the intensity indications are less reliable with the more involved spectrometer systems than with the simpler retarding potential method. The RPA data could be reasonably well evaluated in three groups: (1) hydrogen and helium ions, (2) oxygen and nitrogen (atomic) ions, and (3) the group of molecular ions: O_2^+, N_2^+, and NO^+. Satellite RPA measurements (Dumbs et al., 1979) were used for the model at heights above 220 km. A few ion mass spectrometer (IMS) data (Taylor, 1972) were also considered in building the model. Between 100 km and 250 km the model relies on rocket IMS data compiled by Danilov and Semenov (1978), including American, Russian, and a few European measurements.

The most difficult range to describe is below 100 km. Positive cluster ions appear below about 92 km and are the most abundant species below about 84 km. There were only three groups in the world that had developed techniques (with cooled spectrometers) as needed at heights at which collisions play an important role. It was not possible to establish a profile in agreement with all observations because cluster ions are often destroyed in the spectrometer itself (by the electric fields that are applied in the measuring system). After some discussion, data obtained with a particularly designed instrument (Kopp et al., 1978; Kopp, 1984) were taken as reference. Only the total sum of all clusters was given since the number of individual species is large and transitions between species is frequent.

A similar situation was encountered with negative ions that occur only at altitudes below about 80 km. These are also clusters. Only one group had made measurements in this difficult height range (Arnold et al., 1971). Their average daytime profile was incorporated into IRI.

After the first IRI was released in 1978 (Rawer et al., 1978a), it was critically tested with a wide variety of data. This testing period lasted about one decade. Since 1982, COSPAR in cooperation with URSI has organized yearly workshop meetings to discuss and improve the model (see Table 1). The computer code has been changed step by step and new features introduced as they have become available. COSPAR has published the papers presented at these meetings in its periodical, *Advances in Space Research*. The proceedings of seven of these workshops have appeared in the years from 1982 through 1990 (see Table 1). More than 300 scientists are listed as authors of more than 230 individual papers filling a total of 1,458 pages. The tables of contents of these reports are listed in Chapter 5.

Another result of these discussions is worth noting: For quite a number of unresolved questions, the existing data base was insufficient to give a well founded answer. As a reaction, special data analysis and collection efforts were undertaken in different countries. For example, the AEROS satellite team decided to organize the data reduction and evaluation scheme in such a way that a worldwide picture of electron and ion temperatures, and ion

Table 1: Workshop Meetings for Discussion of IRI

Year	Place	Published Year	Papers	Publication	Pages
1971	Seattle (USA)	1972	21	*Space Res.* XII	1229-1335
1973	Konstanz (FRG)	1974	52	See Rawer (1974)	1-460
1974	Sao Paulo (Brazil)	1975	5	*Space Res.* XV	295-334
1982	Ottawa (Canada)	1982	14	*Adv. in Space Res.* 2, # 10	181-257
1983	Stara Zagora (Bulgaria)	1984	24	*Adv. in Space Res.* 4, # 1	1-169
1984	Graz (Austria)	1985	18	*Adv. in Space Res.* 5, # 7	1-112
1985	Louvain (Belgium)	1985	23	*Adv. in Space Res.* 5, # 10	1-130
1986	Toulouse (France)	1987	22	*Adv. in Space Res.* 7, # 6	1-127
1987	Novgorod (USSR)	1988	53	*Adv. in Space Res.* 8, # 4	1-251
1988	Espoo (Finland)	1990	24	*Adv. in Space Res.* 10, # 8	1-132
1989	Abingdon (UK)	1990	17	*Adv. in Space Res.* 10, #11	-

composition could be obtained in a readily usable form. In the U.S.S.R. and in India several rocket campaigns were conducted to get a sound data base for an improved ion composition vs. height formula.

Not all steps taken in the course of discussions were found to be favorable. While originally an interrelationship between electron density and temperature was implemented, it was found that, in spite of clear experimental evidence for individual cases, this is not justified when dealing with monthly medians. Another unfortunate decision (in response to a request by the competent URSI Commission) was made with the temporary introduction of Chiu's (1975) simplified peak description as a second choice besides the numerical CCIR maps. This action was withdrawn later when it became apparent that this (regionally helpful) description is not acceptable in many parts of the world.

In their 1978 paper, Rawer et al. (1978b) noted a few open problems: checking by propagation experiments, comparison of elf propagation with full wave computations using IRI, comparison with ionospheric absorption measurements, extension toward greater heights, improved data base for ion composition, in particular at lower and at very great heights, and improved data base in the low latitude belt. Some of these problems were resolved; meanwhile, others are still pending.

2.2 Electron Content Measurements and IRI

Reinhart Leitinger
Institut für Meteorologie und Geophysik
University of Graz, 8010 Graz, Austria

Abstract—The use of ionospheric electron content data from Differential Doppler measurements for comparison with the International Reference Ionosphere (IRI) is demonstrated. A data base of European electron content data exists in Graz and was used for the comparison. The data were obtained at several receiving stations from the signals of the Navy Navigation Satellites (NNSS). Their nearly polar and nearly circular orbit is at a nominal height of 1000 km. The data gained at Lindau/Harz, Federal Republic of Germany, were used, with calibration by means of latitudinal profiles of electron content observed from Graz, Austria, if available. The comparison was based on monthly medians of electron content for latitudes 60°, 55°, 50°, and 45° north and local time intervals of two to three hours. Two levels of solar activity were considered: $0 \le R \le 40$ (low solar activity—LSA) and $130 \le R \le 170$ (high solar activity—HSA). Apart from electron content, two other integral parameters that can be derived from the IRI are discussed: (1) the equivalent slab thickness τ and (2) an ionospheric shape factor η. Both parameters are important for the assessment of transionospheric propagation errors.

2.2.1 Measurement Technique and Data

Electron content and other integral parameters for the ionosphere from the ground to ceiling heights around 1000 km are important both for geophysical and for engineering applications. Since actual measured values are not always available, one has to rely on models for many purposes. One of the areas of great practical importance is the prediction and the assessment of transionospheric propagation errors as needed, for example, space geodesy, radio astronomy, time dissemination via satellites, satellite and space probe navigation. Only a few papers have been published that deal with the comparison of measured electron content with the IRI (e.g., McNamara and Wilkinson, 1983; McNamara, 1985; Bilitza et al., 1988). Almost all published comparisons were based on electron content gained by means of the Faraday effect on the signals of geostationary satellites.

Modern measurement techniques for electron content are based on propagation effects observed on signals transmitted from satellites to ground stations. Several signal components are needed to separate plasma effects from geometric and neutral gas effects. The most important experimental methods are listed in Table 1 together with the signal components used.

Technique	Faraday Effect	Differential Doppler Effect	Group Delay
Alternate Name	-	Carrier Phase Difference	Modulation Phase Difference
Signal Components	Left- and right-hand circular components of one carrier	Two coherent carriers with large difference in frequencies	Identical and coherent modulations on two carriers
Frequency Bands	VHF	VHF/UHF, L-Band	c:[*] VHF/UHF, L-Band m:[†] 0.1 ... 10 MHz
Satellites	Beacon of geostationary communications satellites	Navy Navigation Satellite System (NNSS), Global Positioning System (GPS)	ATS 6 Radio Beacon GPS
Carrier Frequencies f_1, f_2/MHz	136	NNSS: 150, 400 GPS: 1227, 1575	ATS 6: 140, 360 GPS: 1227, 1575
Reference Frequency/MHz	-	NNSS: 50 GPS: 1227	-
Sensitivity $\Delta\phi/\Delta TEC$[††] $[^\circ/(10^{15}m^{-2})]$	9.12	NNSS: 9.24 GPS: 15.5	ATS 6: 2.11 GPS: 0.13

[*] c = carriers.

[†] m = modulation.

[††] $\Delta\phi$ = phase difference; ΔTEC = electron content difference.

Using geometric optics, the general expression for the received signal phase is

$$\phi = \frac{2\pi f}{c} \int_T^R n\, ds + 2\pi f t$$

where f is the transmitted frequency, c the free space velocity of light, n the refractive index, ds the ray path element, t the time, and the integral is taken from the phase center of the transmitting antenna at T to that of the receiving antenna at R.

All three techniques record propagation effects in the form of phase differences: (1) the Faraday effect as the phase difference between the two circularly polarized components of a suitable satellite signal, (2) the Differential Doppler effect as the phase difference between two coherently transmitted signal carriers transformed to a common reference frequency by phase division, and (3) the Group Delay effect as the difference of modulation phase on two carriers. In each case, the phase difference

contains plasma effects only. The Faraday effect is approximately proportional to the integral over $N B_L$ where N is the electron density and B_L the component of the geomagnetic field strength along the ray path TR; the other two effects are approximately proportional to the integral over N only. For signal frequencies greater than 100 MHz these approximations are very good and higher order effects can be neglected. In the case of the Faraday effect, the integral is evaluated assuming a constant B_L value for the whole ray path. One usually takes the B_L value from a fixed height. For geostationary satellites errors smaller than 5% are obtained with a fixed height of 420 km provided that the result is considered to be the electron content from the ground to a limiting height of 2000 km (Titheridge, 1972). The contribution of the electrons above this limiting height is negligible because of the decrease of B_L and of N with height.

Accordingly, propagation effects on signals transmitted from satellites are in a first order approximation proportional to the electron content between satellite and receiver. This slant electron content can be transformed (approximately) into the vertical electron content at a path height h_t, by multiplying it with the cosine of the angle between ray path and vertical direction (zenith) at h_t. It is common to take a h_t of 350 km or 400 km. Model calculations have shown that $h_t = hmF2 + 50$ km is a better choice with $hmF2$ being the height of the F-layer peak. Ionospheric electron content is often called total electron content (TEC) to distinguish it from sub-peak electron content or other partial contents.

If the propagation effect gives a phase difference greater than 2π, the data are ambiguous and one has to use additional information to resolve this $2n\pi$-ambiguity. In many cases, the transmitted phase and/or the phase shifts in the receiving equipment are not known, which means that one has to add a phase constant (an initial value) that can assume any value (not only multiples of 2π). Provided that transmitter and receiver are stable in respect to phase shifts, the initial value remains constant as long as there is temporal continuity in the received data. Therefore, the initial value problem is in general less severe for geostationary satellites than for orbiting satellites. In the latter case one has to find a new initial value for each pass of a satellite. For geostationary satellites the initial value acts as an additive constant because the projection from slant content to vertical content is done with a constant factor. During the pass of an orbiting satellite the projection factor changes and, therefore, the initial value has a changing influence on electron content. For orbiting satellites only those electron content differences gained for satellite locations with equal zenith angle are free from the initial value influence. For low and midlatitude stations and for satellites in nearly circular polar orbits, equal zenith angle is approximately equivalent to equal latitude differences to the latitude of the receiving station.

Ionospheric electron content depends on time and on location. It is not possible to gain both dependences with one receiving station and with one satellite: The beacons on board geostationary satellites make it possible to

derive the time dependence of electron content along a fixed ray path (or vertical content for a fixed location). Satellites in nearly circular and nearly polar orbits in heights around 1000 km (e.g., the Navy Navigation Satellites) give the latitude dependence of electron content for essentially constant time (the typical duration of a high elevation NNSS pass is 20 minutes). Satellites in high orbits (e.g., the satellites of the Global Positioning System – GPS – in 20,000 km height) mix temporal and spatial dependence of electron content.

The Differential Doppler data used in this study were gained by means of the signals of the NNSS. The receiving station was Lindau/Harz, Federal Republic of Germany (51.62° north, 10.09° east). For a part of the satellite passes, the initial phase value was determined by the two stations method (Leitinger et al., 1975) with data from the receiving station Graz, Austria (47.08° north, 15.45° east). For the remainder the initial phase value was determined using assumptions about the latitudinal structure of the ionosphere (single station method, see Leitinger and Putz, 1978). The latitude dependence of electron content was gained with a fixed mean ionospheric height of 400 km, using the geographic coordinates of the point in this height on the straight line from the receiver to the satellite.

Electron content was gained from the IRI by means of numerical integration from 60 km to 1000 km using a step-size of 10 km. The comparison is based on monthly medians of electron content for the latitudes 60° north, 55° north, 50° north, and 45° north. Because of the irregular distribution of NNSS passes, the day is divided into nine three-hour intervals starting at midnight. The monthly medians were calculated in each interval both for low solar activity (LSA) and for high solar activity (HSA). The criterion for low solar activity was a monthly mean solar sunspot number R not greater than 40 (nominal value $R = 20$), and for high solar activity an R between 130 and 170 (nominal value 150). For LSA all months from 1975 to 1976 were included; for HSA a selection of months was taken from the years 1978 through 1982 (Feichter et al., 1988, 1989).

2.2.2 Comparison of Monthly Medians

The comparison of electron content measurements with IRI data is demonstrated for a latitude of 50° north, 15° east, a typical midlatitude location both geographically and geomagnetically. The results of the direct comparison of monthly medians is shown in Figures 1 to 3. Examples for the seasonal variation are displayed in Figure 1 for the time intervals 06-09 LT and 11-13 LT, both for low and high solar activity. Because of the quick change of electron content in the morning time interval, the comparison for 06-09 LT is not too conclusive, but it can be clearly seen that the IRI gives an October maximum both for LSA and for HSA not present in the NNSS results for LSA. For noontime there are considerable differences in winter (Figure 1c): The IRI data are too high when compared with the NNSS data. During summer good agreement is found for HSA (Figure 1d).

14

Fig. 1. Comparison of the annual variation of electron content (TEC) from IRI with that from NNSS Differential Doppler measurements in units of $10^{15}m^{-2}$:

a) (top left) Low solar activity, morning
c) (bottom left) Low solar activity, noon

b) (top right) High solar activity, morning
d) (bottom right) High solar activity, noon

15

Fig. 2. Comparison of the diurnal variation of electron content (TEC) from IRI with that from NNSS Differential Doppler measurements in units of $10^{15}m^{-2}$:

a) (top left) Low solar activity, January
c) (bottom left) Low solar activity, March

b) (top right) High solar activity, January
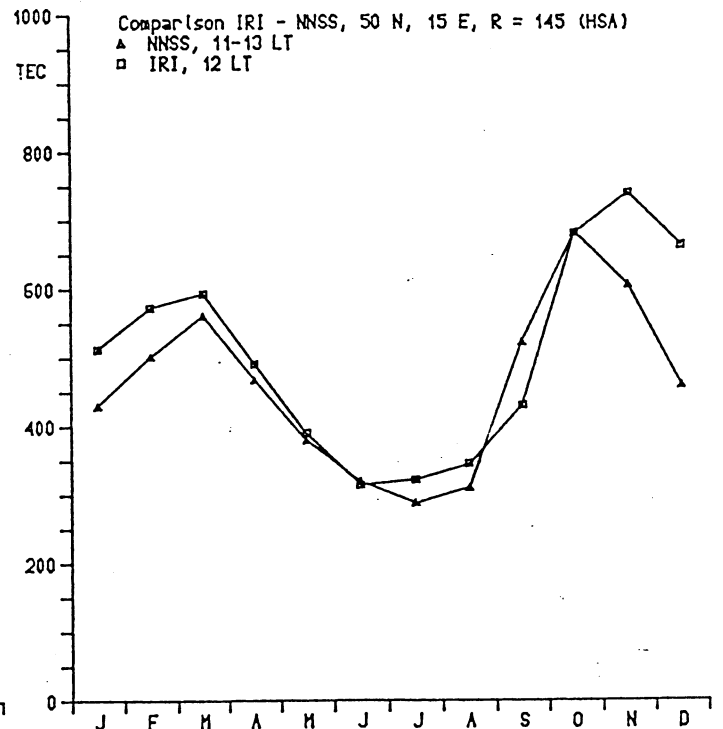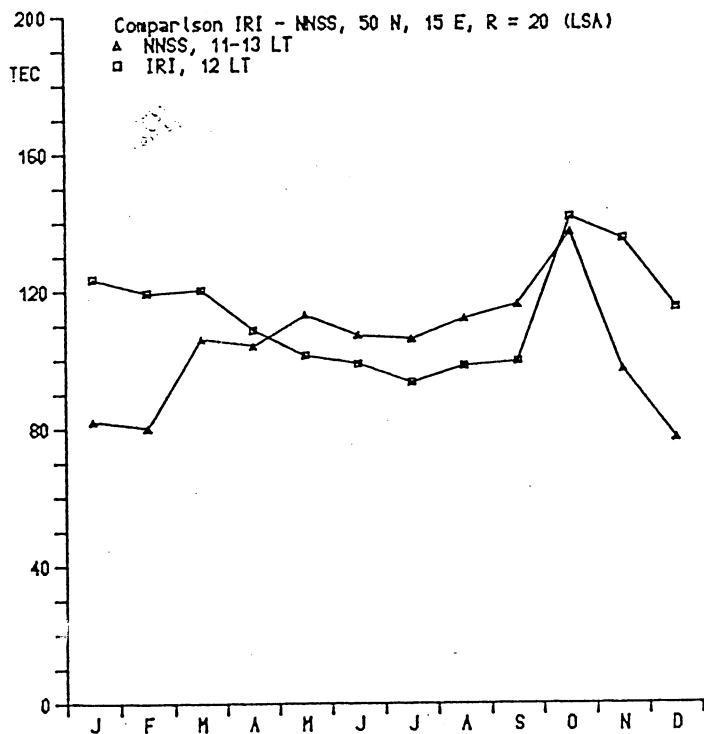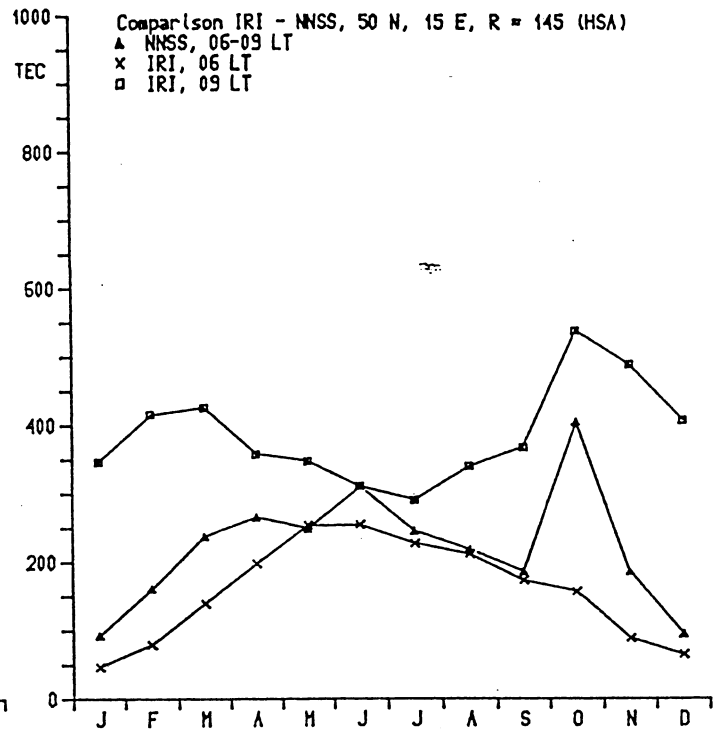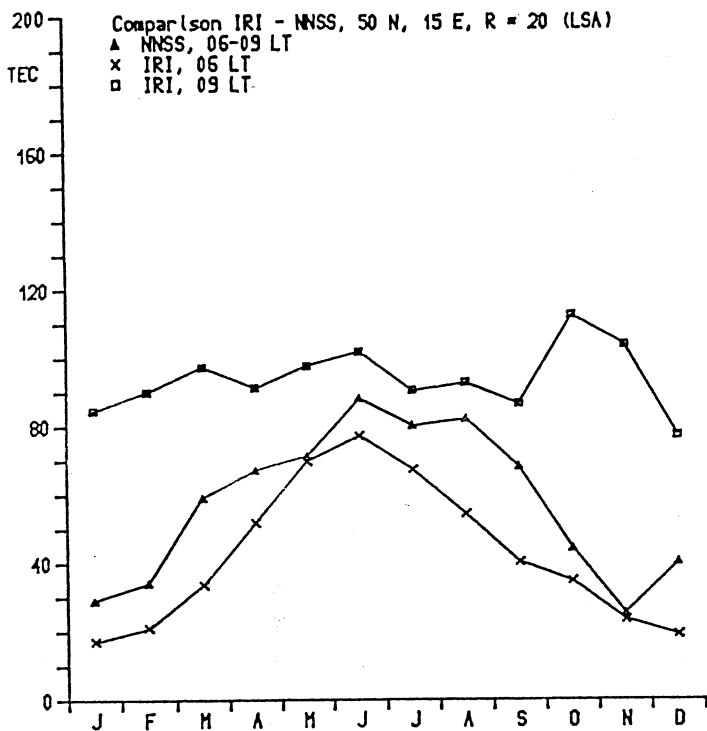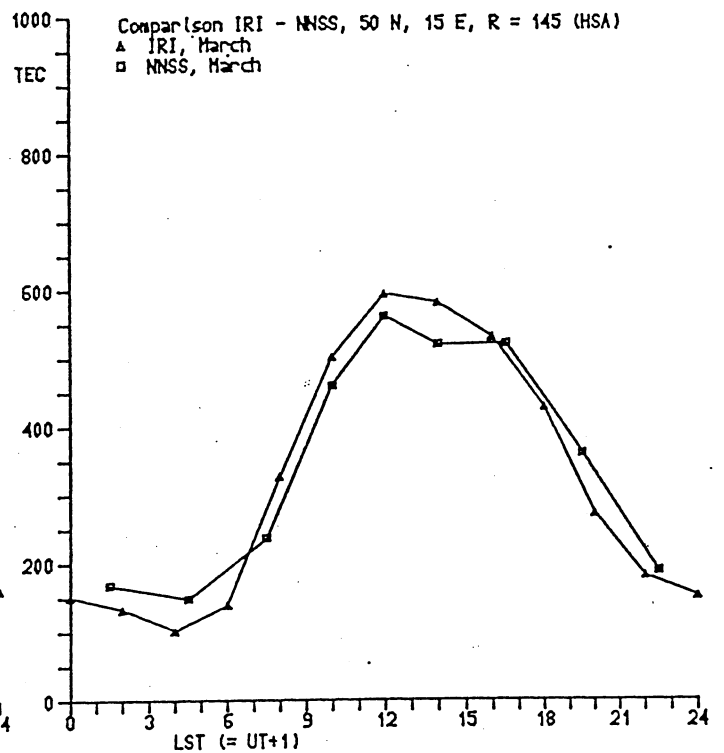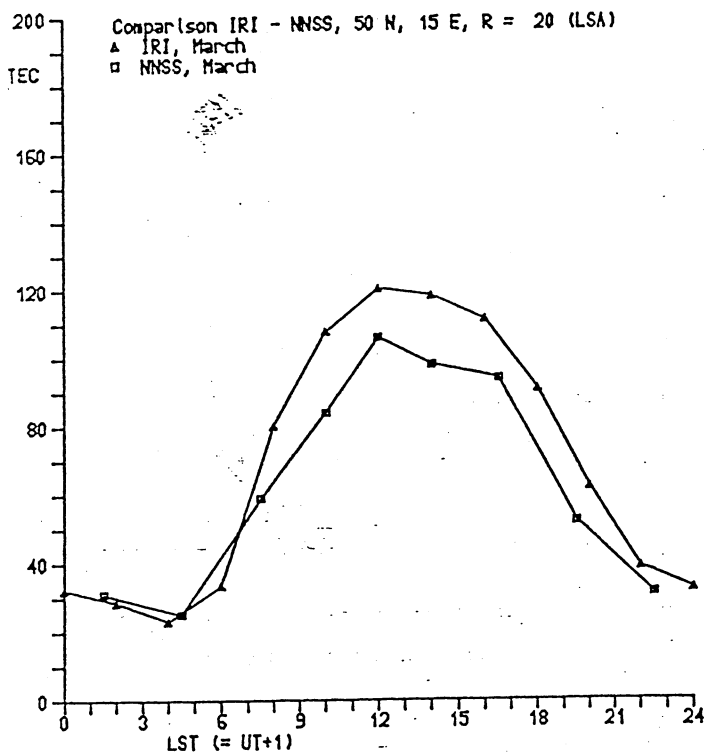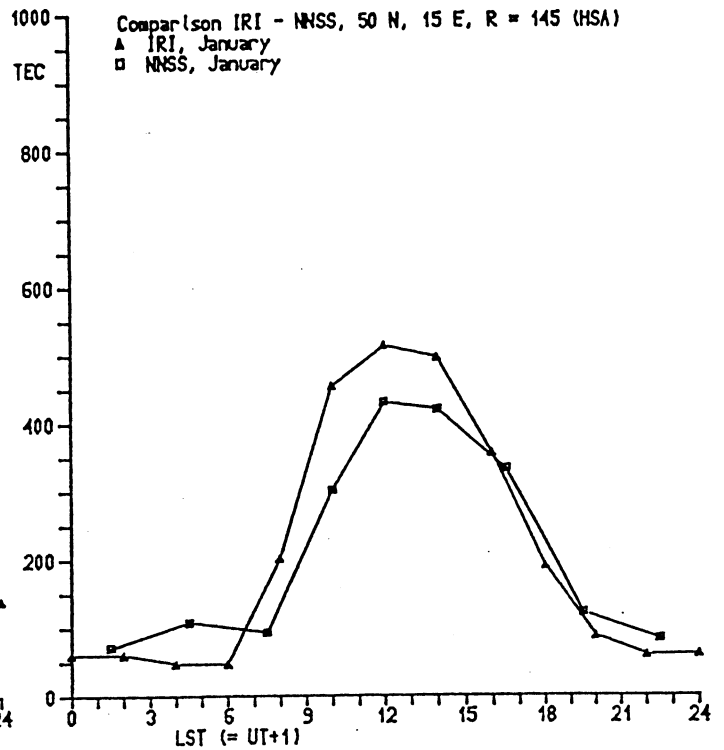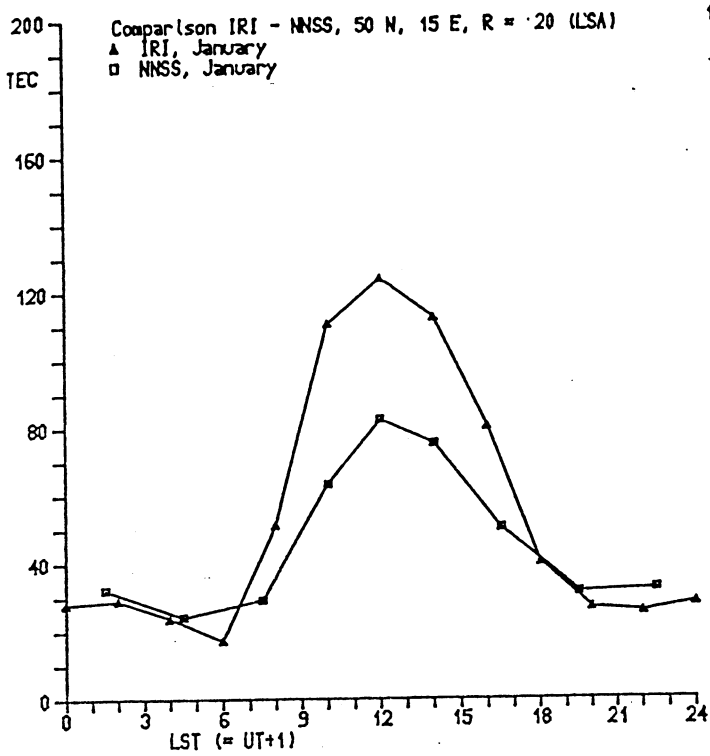d) (bottom right) High solar activity, March
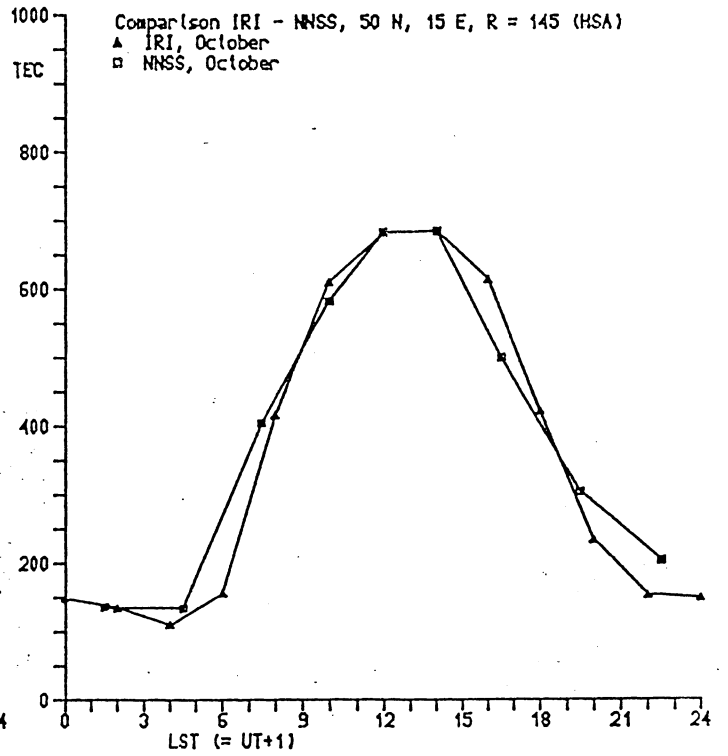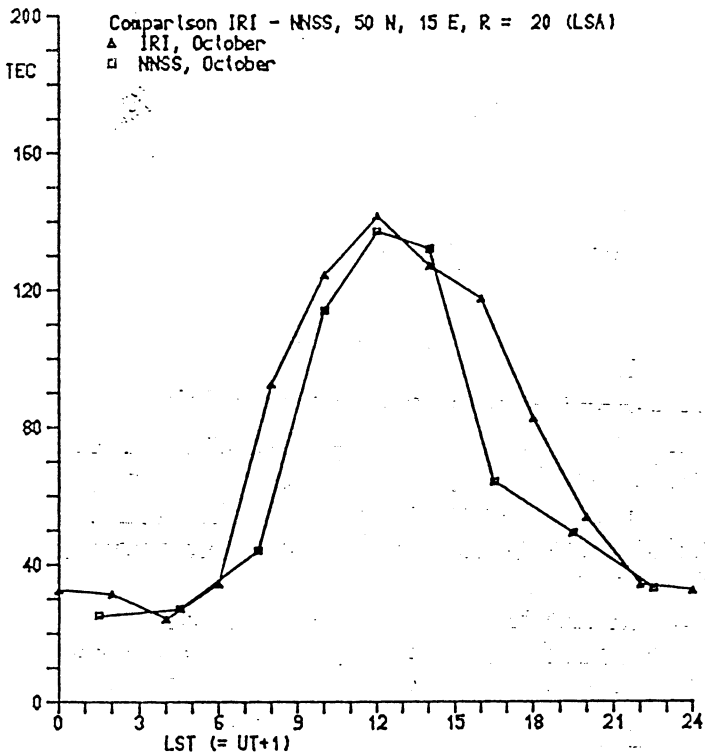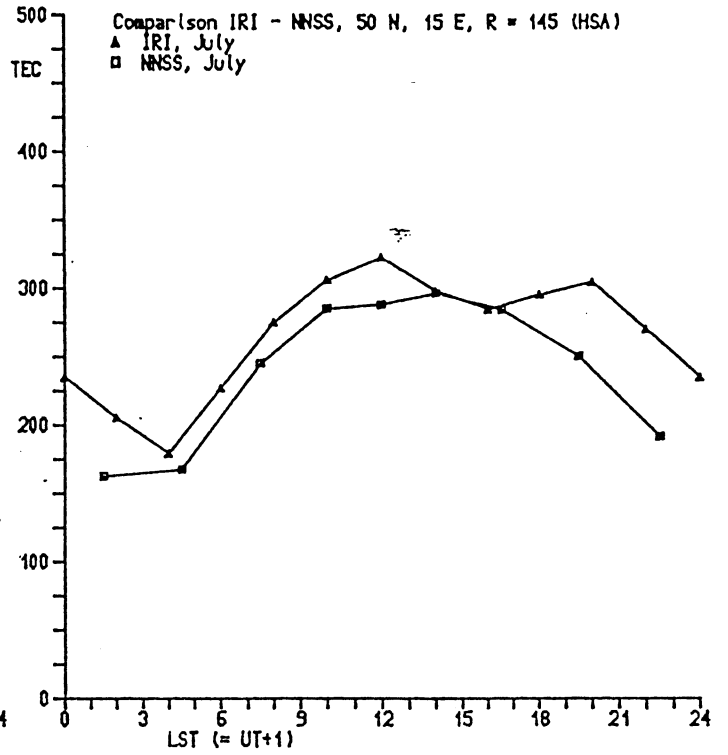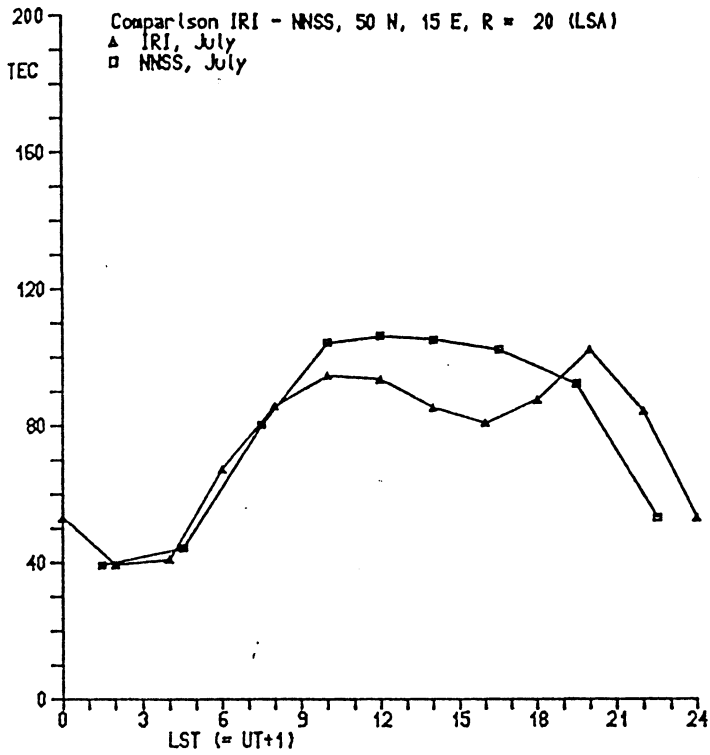
Fig. 3. Comparison of the diurnal variation of electron content (TEC) from IRI with that from NNSS Differential Doppler measurements in units of $10^{15}m^{-2}$:

a) (top left) Low solar activity, July
c) (bottom left) Low solar activity, October

b) (top right) High solar activity, July
d) (bottom right) High solar activity, October

17

Comparing the shape of the annual variations around noon reveals that for HSA the absolute IRI maximum occurs in November whereas the NNSS maximum is seen in October (Figure 1d). Since the IRI F2-peak exhibits the same November maximum, it is clear that this is a feature of the CCIR coefficients.

The diurnal curves exhibit the strongest differences in winter for LSA (Figure 2a). The shape of the winter curves is, however, similar. The diurnal curves for summer have different shapes (Figures 3a and b): IRI exhibits a double-peaked diurnal curve from May through August for LSA and from June through July for HSA. For low solar activity the evening maximum which occurs around 20 LT is even higher than the morning maximum occurring around 10 LT (Figure 3a).

2.2.3 Electron Content Differences

Since the initial value could add a bias to the NNSS data, it is advisable to compare electron content differences for suitably chosen latitudes. We have chosen the difference between the electron contents at 45° north and 60° north, which is comparatively free of latitudinal biases. The statistical properties of daytime (10-17 LT) electron content differences from NNSS observations are shown in Figure 4 in the form of "boxplots" (Kleiner and Graedel, 1980) with the range of IRI data added to the display. For LSA the IRI data are clearly too high, but for HSA they are too small. From October through February the TEC differences from IRI are even predominantly negative, a finding that contradicts the widespread experience that midlatitude TEC increases with decreasing latitude.

2.2.4 Equivalent Slab Thickness τ and Shape Factor η

Since electron content can be separated into peak electron density times equivalent slab thickness τ and since IRI takes peak electron densities from the CCIR (1967) model coefficients, it makes sense to investigate the equivalent slab thickness τ as predicted by IRI. Figure 5 shows the annual variation of the IRI equivalent slab thickness for different latitudes at noon and midnight and during low and high solar activity. For high solar activity a comparison was made with experimental data gained by the combination of electron content from the Faraday effect on the VHF signal of the geostationary satellite SIRIO (receiving station Graz, Austria, with the ionospheric point at 400 km having the coordinates 42.0° north, 10.2° east) with peak electron density from the ionograms of Rome, Italy (41.8° north, 12.5° east) (Skedel, 1989). The comparison was done with monthly medians for the years 1981 and 1982. The results can be summarized as follows:
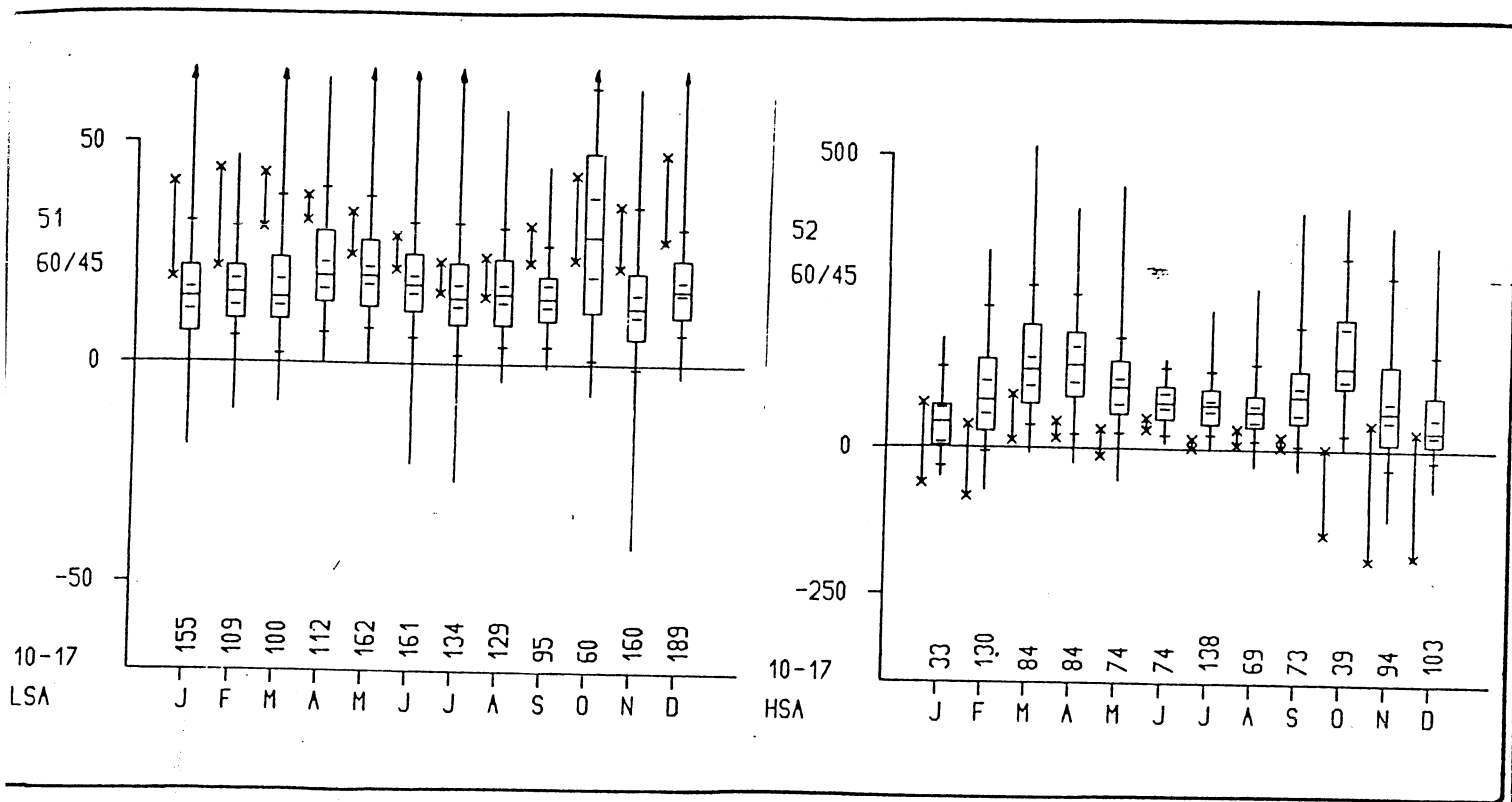
Fig. 4. Monthly boxplots for the difference of electron content at 45° north and 60° north from NNSS observations during daytime (10-17 LT) in units of $10^{15}m^{-2}$. Left hand panel: low solar activity (LSA, R = 20). Right hand panel: high solar activity (HSA, R = 150). Boxes: from quartile to quartile, divided by the median; vertical lines to the maximum and to the minimum, respectively. Short horizontal dashes: uppermost and lowest deciles and confidence limits (5% error probability) of the median. The number of data per month is displayed at the bottom. At the left of each box, one finds the range of IRI results for the local time interval 10-17 LT (x — x).

- 00 LT: The annual curve of IRI-τ is below the "observed" curve. For 1981 a decrease of IRI-τ by 50 km would improve the situation considerably.

- 06 LT: The IRI annual curve is still too high, but the experimental slab thickness is not very reliable in winter when sunrise is near 06 LT.

- 12 LT: In summer IRI-τ fits the observed τ comparatively well, but in winter the IRI values are too high by up to 70 km.

- 18 LT: The IRI data for 1982 were larger than the observed values throughout. For 1981 this is true for all months except April and June, which showed comparatively good agreement. The differences are highest in winter.

The IRI slab thickness shows a peculiar behavior near the geomagnetic equator (Figure 5a) and near the crest of the equatorial anomaly (Figure 5b).

IRI equiv. slab thickness, 11 N, 15 E

△ 00 LT (23 UT), R = 20 (LSA)
+ 12 LT (11 UT), R = 20 (LSA)
□ 00 LT (23 UT), R = 145 (HSA)
× 12 LT (11 UT), R = 145 (HSA)

IRI equiv. slab thickness, 20 N, 15 E

△ 00 LT (23 UT), R = 20 (LSA)
+ 12 LT (11 UT), R = 20 (LSA)
□ 00 LT (23 UT), R = 145 (HSA)
× 12 LT (11 UT), R = 145 (HAS)

IRI equiv. slab thickness, 42 N, 15 E

△ 00 LT (23 UT), R = 20 (LSA)
+ 12 LT (11 UT), R = 20 (LSA)
□ 00 LT (23 UT), R = 145 (HSA)
× 12 LT (11 UT), R = 145 (HSA)

IRI equiv. slab thickness, 50 N, 15 E

△ 00 LT (23 UT), R = 20 (LSA)
+ 12 LT (11 UT), R = 20 (LSA)
□ 00 LT (23 UT), R = 145 (HSA)
× 12 LT (11 UT), R = 145 (HSA)

Fig. 5. Annual variation of equivalent slab thickness from IRI in km for different geographic latitudes and geographic longitude 15° east:

a) (top left) Vicinity of the geomagnetic equator (11° north)
b) (top right) Vicinity of the crest of the equatorial anomaly (20° north)
c) (bottom left) Latitude 42° north (comparison with data Faraday Graz—ionosonde Rome)
d) (bottom right) Latitude 50° north

The equator τ is higher for LSA than for HSA and the equator slab thickness is higher than the crest slab thickness (Figures 5a and b). The crest τ and the equator τ for HSA exhibit almost no seasonal dependence. There is almost no solar activity dependence of slab thickness near the crest of the equatorial anomaly (Figure 5b). A decrease of solar activity dependence of IRI-τ with decreasing latitude is seen in midlatitudes, too (Figures 5c and d).

Since the contributions to slab thickness from the electrons above the F-layer peak are much higher than the contributions from the sub-peak electrons, it is clear that the IRI deficiencies in the slab thickness behavior stem from the Bent model (Llewellyn and Bent, 1973). This impression is enhanced when one studies the behavior of other parameters of the electron density profile. One such parameter is the so-called shape factor, a quantity needed for the assessment of higher order range errors, which play an important role in space geodesy and similar applications of the transionospheric propagation of radio waves (Leitinger and Putz, 1988). The shape factor η is defined by
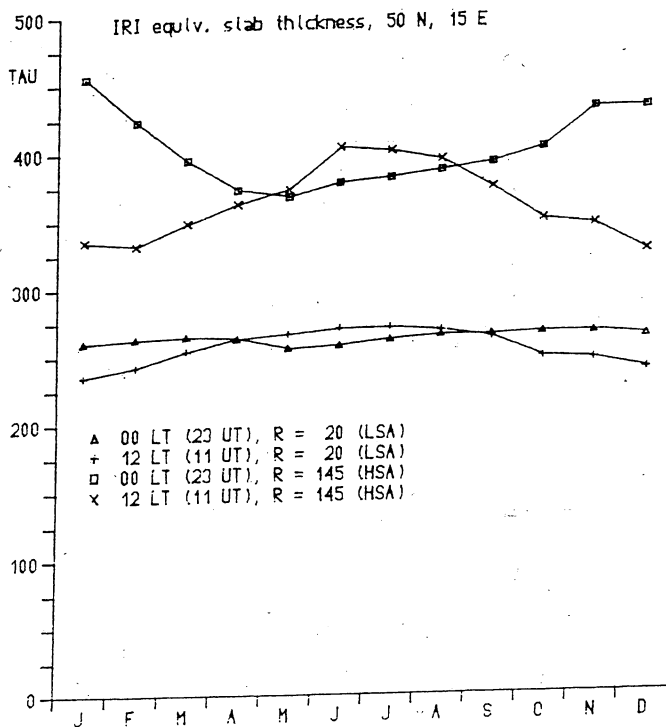
$$\eta = \frac{1}{\tau} \int_0^{h_s} \left(\frac{N}{N_m}\right)^2 dh$$

IRI gives a shape factor that is nearly independent of latitude and time and is about 0.616 for LSA (R = 20) and 0.638 for HSA (R = 145). Since η reflects strongly the electron density profile above the peak, this behavior means that the Bent model on which the IRI is based in this region has a shape that is practically independent of latitude and time and changes only slightly with solar activity. Recently, Buonsanto (1989) has compared electron density profiles measured by the incoherent scatter radar at Millstone Hill, Massachusetts, with IRI profiles. The comparison shows that even under geomagnetically quiet conditions the measured profiles can differ considerably from the IRI profiles, especially above the peak. Table 2 gives the electron content TEC, slab thickness τ, and shape factor η obtained by numerical integration of the values read from Buonsanto's figures.

Table 2: **Integral Parameters from Profiles Measured at Millstone Hill (46.2° N, 71.5° W)**

		Low Solar Activity				High Solar Activity			
Season	LT	Date	TEC	τ	η	Date	TEC	τ	η
	HH	YYMMDD	$10^{15}m^{-2}$	km		YYMMDD	$10^{15}m^{-2}$	km	
Summer	00	850813	16.8	172	0.576	800608	156.9	258	0.631
Summer	12	850813	72.8	269	0.637	800608	283.5	328	0.586
Winter	00	860209	13.6	225	0.630	801220	67.3	277	0.625
Winter	12	860209	99.9	192	0.561	801220	432.7	211	0.581

2.3 Morphology of Electron Temperature Anisotropy in the F-Region

Koh-ichiro Oyama
Institute of Space and Astronautical Science
3-1-1, Yoshinodai, Sagamihara, Kanagawa, 229, Japan

Abstract—Electron temperature was measured by means of planar probes that were installed on Japan's ninth polar-orbiting satellite OHZORA. The measurements were carried out at the same time both along ($T_{\parallel}$) and vertical ($T_{\perp}$) to the geomagnetic field and showed the difference between these two temperatures. $T_{\parallel}$ is more often higher than $T_{\perp}$ during nighttime. In the daytime $T_{\parallel}$ is sometimes lower than $T_{\perp}$ and sometimes higher. Dependence of the anisotropy upon geomagnetic latitude, local time, season, and height is investigated.

2.3.1 Instrument and Data

Japan's ninth scientific satellite OHZORA was launched on February 14, 1984, to study, besides other mission goals, plasma phenomena in polar and equatorial regions. The polar orbiting satellite measured in the altitude range from 350 km to 900 km. Electron temperature probes were installed together with other plasma instruments, such as particle analyzers, a wave receiver, an electron density probe, and a topside sounder. One of the objectives of the electron temperature measurements was the study of the anisotropy of the electron temperature. Results of this investigation are presented here.

Four planar probes (diameter: 120 mm) were put at the very end of the four solar cell paddles, as shown in Figure 1. Three probes were dedicated to electron temperature measurements, and one was used as a fixed bias Langmuir probe to measure the relative electron density. During most of the time, the satellite was non-spun, but occasionally it was spun very slowly. The maximum spin rate in the past has been 0.6 rpm. Usually, the spin rate was 0.2 rpm or less. The satellite spin axis was controlled to point towards the sun with an accuracy better than 1°.

The principle of the instrument and the data reduction method was described by Hirao and Oyama (1970) and Oyama et al. (1985). The probes whose sensor plates are vertical to the geomagnetic field lines (S3 and S7 in Figure 1) measure the parallel electron temperature $T_{\parallel}$, and the probes whose sensor plates are parallel to the geomagnetic field lines (S1 and S5 in Figure 1) measure the vertical electron temperature $T_{\perp}$. For this statistical study only those data points were used for which at least one of the sensors was aligned with the magnetic field to within ± 20°. The data were also carefully checked to remove measurements carried out in disturbed areas in the satellite wake or in the thick sheath which may be caused by the strong

23

REVO.8355 22:12 UT

B

X
S1

GAX GAS
S7
GAY GAZ

$T_\perp$ 1310K

Z

S3

S5

Y $T_{//}$ 2180K $T_\perp$ 1350K

V_S
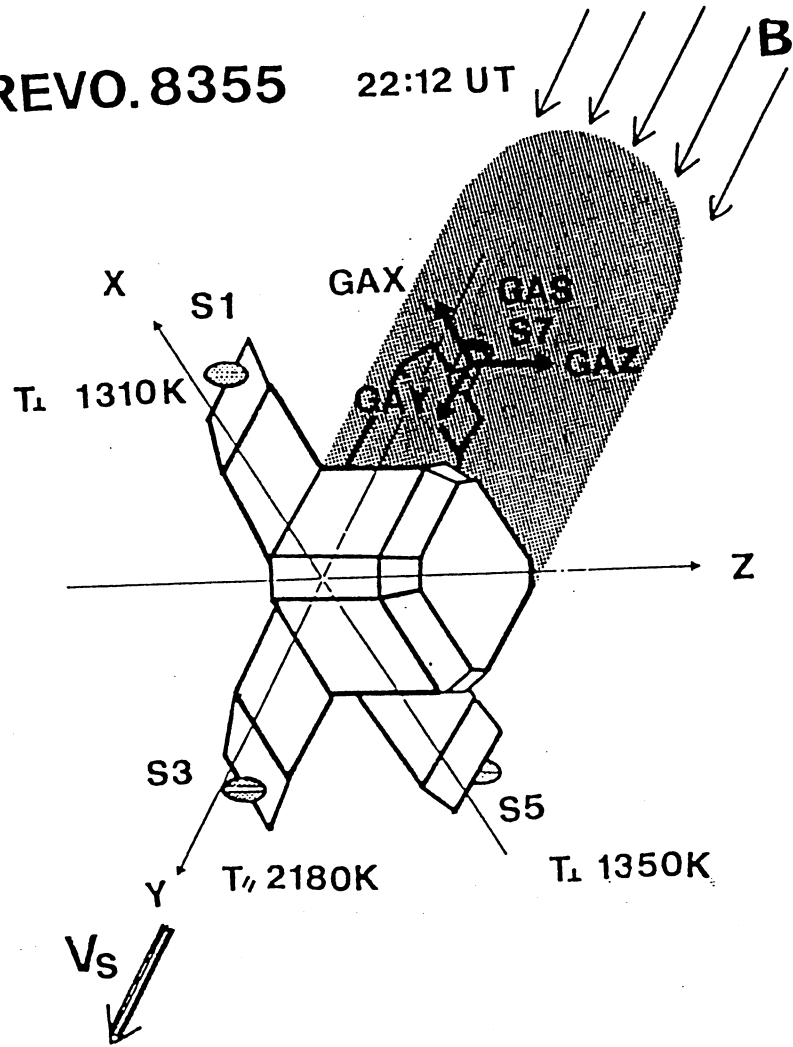
Fig. 1. Satellite OHZORA and location of the four temperature probes; sensors S1, S3, and S5 are used as the electron temperature probes while the sensor S7 measures ion and electron currents.

satellite charging. Altogether, 505 data points are used from observations carried out between February 1984 and December 1985.

2.3.2 Results for Individual Orbits

Figure 2 shows results which were obtained with sensors S1 and S3 during the satellite orbit 947; the two sensors are orthogonal to each other. The upper panel shows the angles between the geomagnetic field direction and the three satellite-centered axes X, Y, and Z (see Figure 1). To simplify matters, we will call these angles X, Y, and Z as indicated in Figure 2. Also shown (thin line) is the floating potential, which is measured by means of one of the sensor electrodes with respect to the satellite potential. The second panel from the top shows the ratio of electron temperatures obtained by the two sensors S1 and S3. The individual electron temperatures are plotted in the two lowest panels. Orbit attitude information is listed at the bottom of Figure 2, including the Universal Time (UT), the altitude (HHGT), L-value (FL), geomagnetic latitude (GLAT), geographic latitude (XXLAT), longitude (XXLON), and magnetic field strength (BB).

From 0051 UT to 0056 UT, the satellite traversed the polar cap, observing a large scatter of electron temperature values during that time. Oyama and Abe (1987) concluded that this scatter is real and reflects the geophysical conditions in the polar ionosphere. Between 0056 UT and 0057 UT, both temperatures exhibit a dip decreasing to a minimum value of 2000 K at 005640 UT and increasing again to 2600 K at 0057 UT. This region corresponds to the boundary where the flux of precipitating auroral electrons (0.2~16 keV) starts decreasing and the flux of trapped energetic particles of 0.1~140 MeV energy begins to increase. Simultaneous measurements show a maximum of the counting rate of energetic particles at 0058 UT.

At the beginning of the orbit the angle Y is about 170°. This means that sensor S3 is nearly vertical to the geomagnetic field, and, therefore, it is picking up most of the parallel component of electron temperature $T_{\parallel}$, while the sensor S1 is picking up the vertical component $T_{\perp}$. The panel second from the top shows that $T(S1)/T(S3)$ is 0.7 at this time; that is, $T_{\parallel}$ is 1.4 times higher than $T_{\perp}$. From 0051 UT to 0059 UT, the ratio increases toward one as the angle changes from 170° to smaller values. At 0059 UT the angle Y is nearly 135° and the angle Z is 108°. In this configuration S1 and S3 should pick up equal fractions of the electron temperatures $T_{\parallel}$ and $T_{\perp}$. In fact, the second panel shows that $T(S1)/T(S3)$ is nearly equal to one at this time. After 0059 UT the situation reverses, and the parallel temperature is more strongly observed by sensor S1. $T(S1)/T(S3)$ is 1.1 at 0102 UT indicating that the parallel component is still larger than the vertical component.
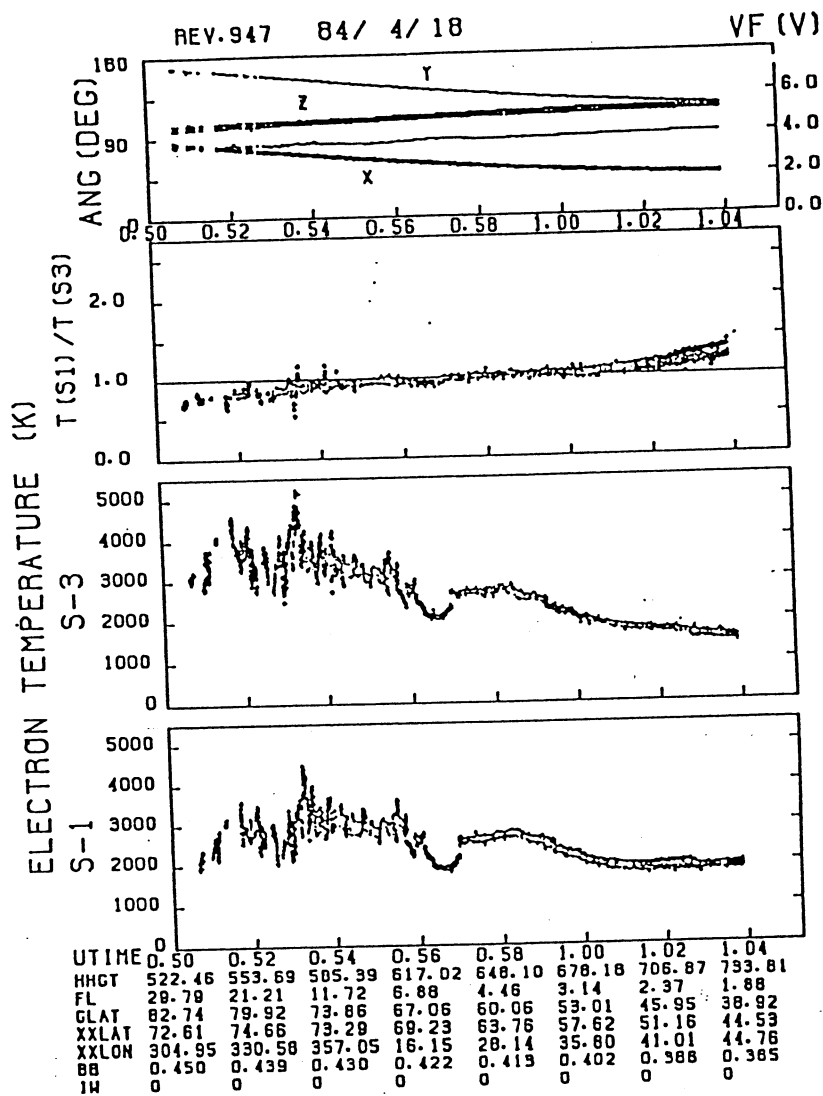
Fig. 2. Electron temperatures measured by the planar probes S1 and S3 during the pass 947 (lower two panels). Top panel shows the angles X, Y, and Z between the X, Y, and Z axes (see Figure 1, page 24) and the geomagnetic field direction. Also shown is the floating potential. The second panel shows the ratio between the two temperatures measured by sensors S1 and S3. Numbers at the bottom are Universal Time in hours and minutes (UTIME), height in km (HHGT), L-value (FL), geomagnetic latitude (GLAT), geographic latitude and longitude (XXLAT and XXLON), intensity of geomagnetic field in Gauss (BB), and IW (sunlight indicator: IW = 0 means satellite is sunlit).

Simultaneous measurements of electron flux in the energy range 0.2 to 16 keV show a strong precipitation pattern during the polar cap crossing from 0051 UT to 0057 UT. Large ion counting rates are seen from 0051 UT to 0056 UT. Thus, there is a time period and region in which electrons are detected, but no ions. This period from 0056 UT to 0057 UT corresponds to a dip in electron temperatures and a slightly enhanced electron temperature anisotropy.

Figure 3 shows the temperatures and the anisotropy observed during the satellite pass 2853. The angles Z and X are about 100° and 15°, respectively, at the beginning of the pass. In this configuration, sensor S1 detects most of the $T_{\parallel}$ component, while S3 detects most of the $T_{\perp}$ component. The ratio of these two temperatures is about 1.5; that is, $T_{\parallel}$ is about 1.5 times higher than $T_{\perp}$. Between 2336 UT and 2337 UT, the configuration is such that both sensors should see about equal fractions of the two temperature components. Figure 3 shows that, indeed, the ratio of the electron temperatures from the two sensors is nearly one during this time period.

For our statistical analysis of the electron temperature anisotropy, we use only electron temperatures obtained when the normal of one planar electrode deviates less than 20° from the magnetic field direction and when the vertical component can be simultaneously obtained from an orthogonally mounted sensor. Figure 4 shows $T_{\parallel}$ versus $T_{\perp}$ for the orbit period from 2331 UT to 2333 UT in Figure 3. During this time period, the angle between the normal of sensor S1 and the geomagnetic field changes from 18° to 24°, and, therefore, sensor S1 detects mostly $T_{\parallel}$ while sensor S3 detects mostly $T_{\perp}$. The data can be approximated by the relation $T_{\parallel} = 1.2 T_{\perp}$ as shown by the solid line in Figure 4. Figure 5 shows data taken between 0116 UT and 0118 UT during the satellite orbit 2721. The broken line shows the best fit curve, which is $T_{\parallel} = T_{\perp} + 250$. In this case, the average temperature ratio ($T_{\parallel} = 1.07 T_{\perp}$ solid line) is obtained by giving more weight to the data points for which the sensor S1 is aligned the closest to the geomagnetic field.

2.3.3 Statistical Results for the Occurrence of Anisotropy

From figures similar to Figures 5 and 6, we have calculated the temperature ratio R (= $T_{\parallel} / T_{\perp}$) for 505 satellite passes and investigated the dependence of R upon geomagnetic latitude, local time, season, and altitude. Figure 6 shows histograms of R for different geomagnetic latitude ranges. All data are sampled into six geomagnetic latitude zones without discriminating Southern and Northern Hemispheres. The average height for each data group varies from 555 km to 470 km. At latitudes less than 20°, the number of cases with R less than one is almost equal to the number of cases with R greater than one. The number of cases with R greater than one increases as we go to higher latitudes. We conclude that anisotropy is becoming more likely as we go to higher latitudes.

27

REV.2853   84/ 8/ 23   VF (V)

ANG (DEG)

180

90

0

6.0

4.0

2.0

0.0

Z

Y

X

T (S1)/T (S3)

2.0

1.0

0.0

ELECTRON TEMPERATURE · (K)

S-3

5000
4000
3000
2000
1000
0

S-1

5000
4000
3000
2000
1000
0

UTIME	23.29	23.31	23.33	23.35	23.37
HHGT	377.50	388.95	403.75	421.65	442.37
FL	18.79	11.85	7.11	4.55	3.14
GLAT	80.02	74.16	67.13	59.75	52.25
XXLAT	74.41	73.90	70.08	64.42	57.90
XXLON	329.19	357.92	19.99	33.69	42.19
BB	0.470	0.468	0.465	0.462	0.454
IW	0	0	0	0	0
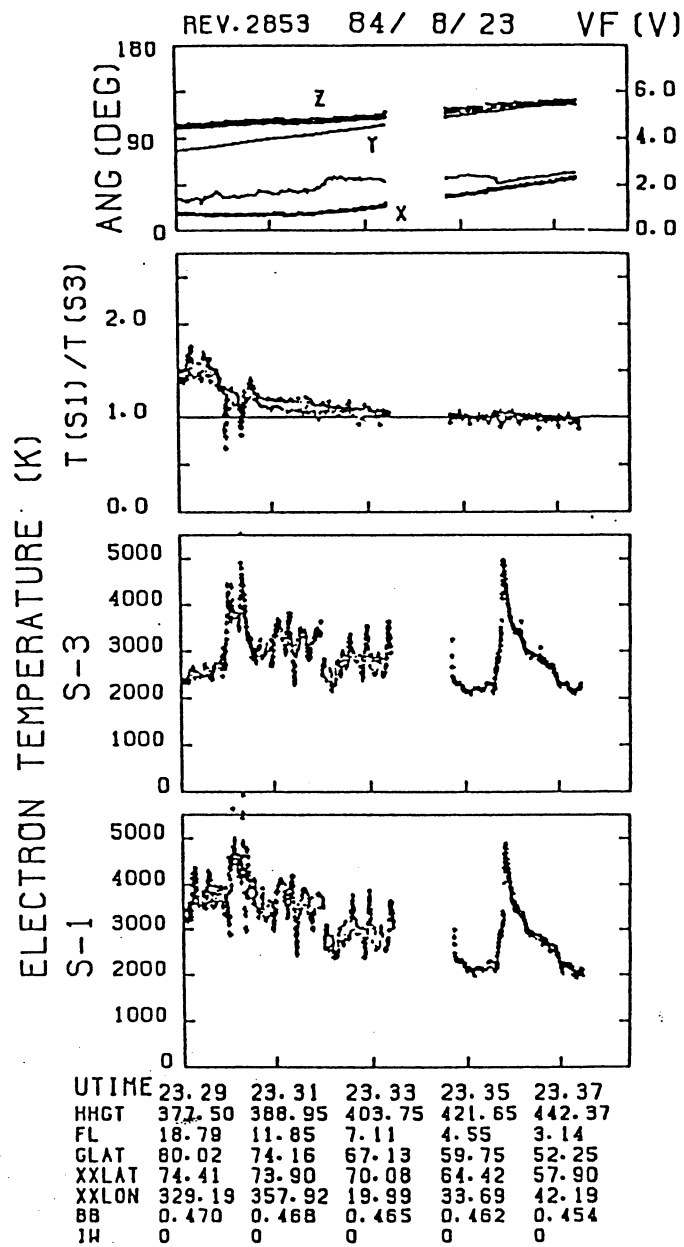
Fig. 3. Same as Figure 2 for orbit 2853.
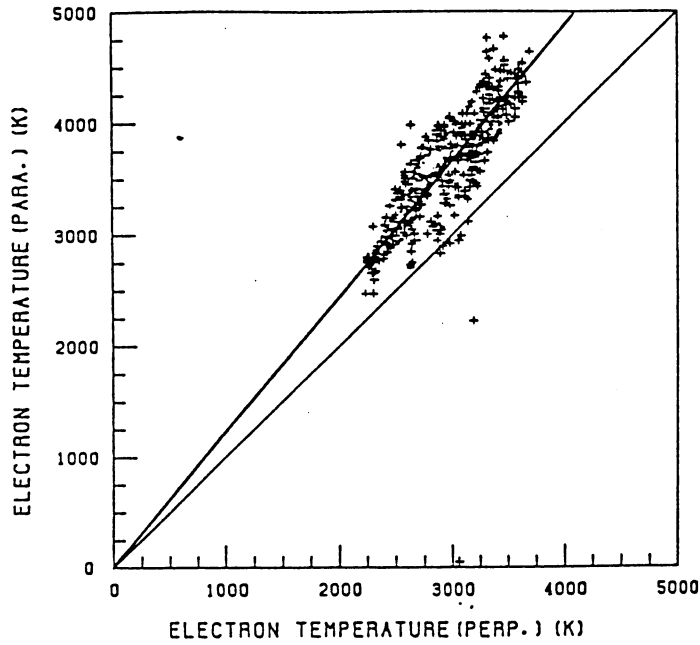
Fig. 4. Parallel electron temperature versus vertical electron temperature during orbit 2853 and best linear fit ($T_{\parallel} = 1.21\,T_{\perp}$).
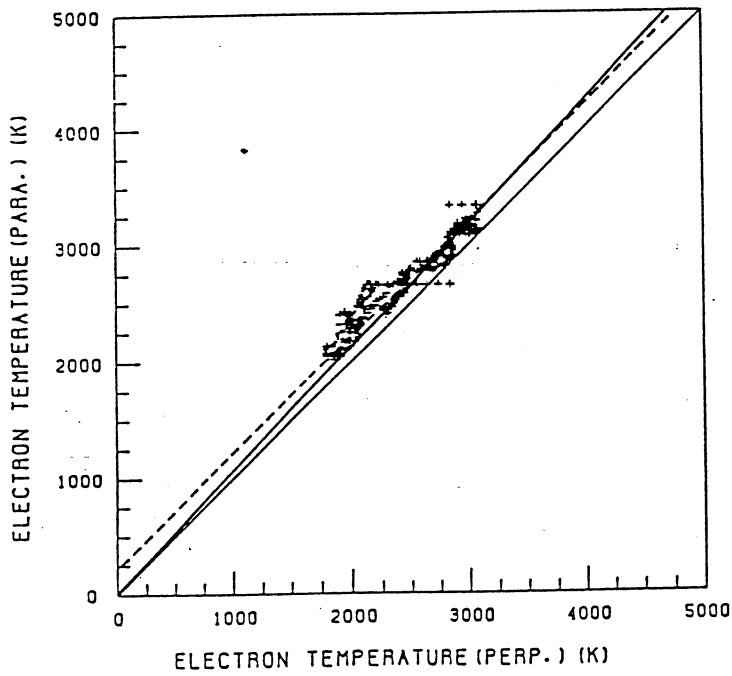
Fig. 5. Parallel electron temperature versus vertical electron temperature during orbit 2721 and best linear fit $T_{\parallel} = T_{\perp} + 250$ (dotted line); also shown is $T_{\parallel} = 1.07\,T_{\perp}$ (thick line).

Secondly, all data were distributed into six local time ranges. Each of the six data sets consists of measurements taken during a four-hour period as shown in Figure 7. The average height ranged from 515 km to 646 km. Each of the six cases indicates a temperature anisotropy with R greater than one, that is, $T_{\parallel}$ greater than $T_{\perp}$. The temperature ratio seems to increase towards midnight.

In order to study how the anisotropy varies with height, all data are grouped into six height zones starting from 300 km in steps of 100 km, as shown in Figure 8. Although we cannot see the influence of height upon the electron temperature anisotropy clearly, a weak tendency seems to exist that $T_{\parallel}$ approaches $T_{\perp}$ gradually as the height increases. It should, however, be noted that temperature measurements become more difficult with increasing height because of decreasing electron density.

Finally, Figure 9 shows the annual variation of R. All data are grouped into six bimonthly periods, starting January 1985. These histograms seem to show that the anisotropy $T_{\parallel} > T_{\perp}$ appears more often in summer (July and August) than in winter (January and February).

Similar statistical analysis is planned to examine the dependence of R on longitude and on solar and magnetic activity.

2.3.4 Conclusions

The investigation of electron temperature anisotropy observed by the OHZORA satellite can be summarized as follows.

- In the equatorial region, $T_{\parallel}$ is sometimes higher than $T_{\perp}$ and sometimes lower. With increasing latitude, the anisotropy $T_{\parallel} > T_{\perp}$ dominates.

- $T_{\parallel}$ is higher than $T_{\perp}$ for all local times. The difference increases and becomes clearer toward evening and during nighttime.

- Anisotropy ($T_{\parallel} / T_{\perp} > 1$) appears more often in summer than in winter.

These results clearly show that anisotropies have to be considered in describing the global and temporal variations of the ionospheric electron temperature. It is therefore recommended that future satellite instruments use temperature probes that can discriminate between the two temperature components.
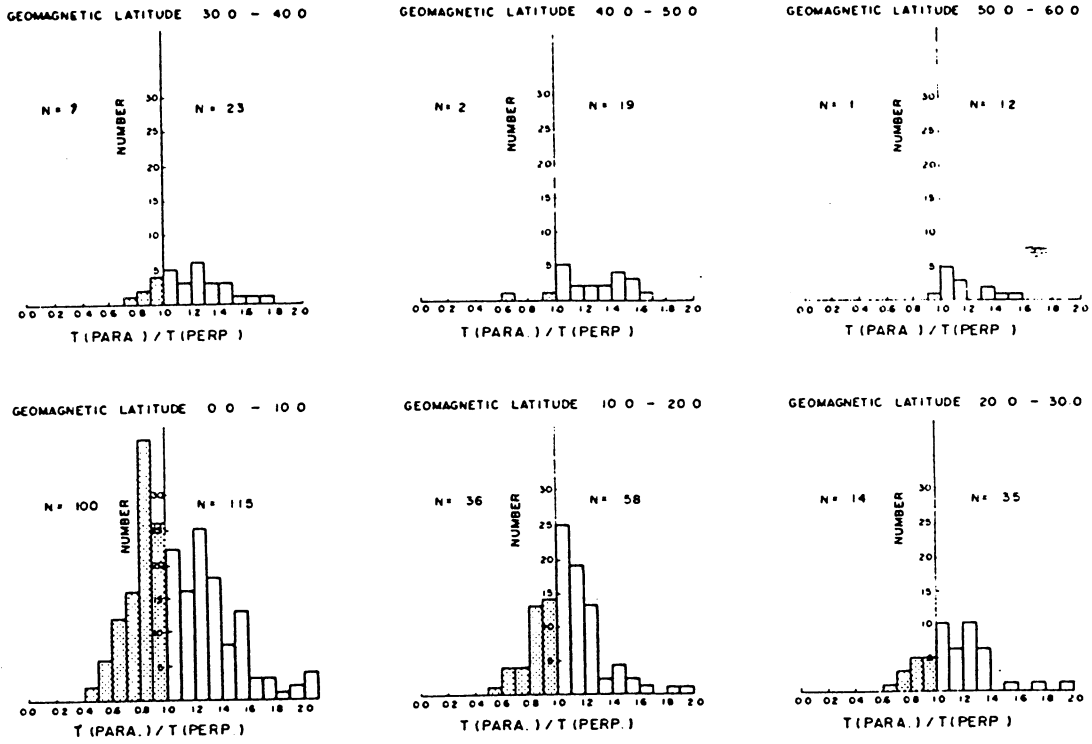
Fig. 6. Histograms of $R = T_{\parallel} / T_{\perp}$ for different latitude zones.
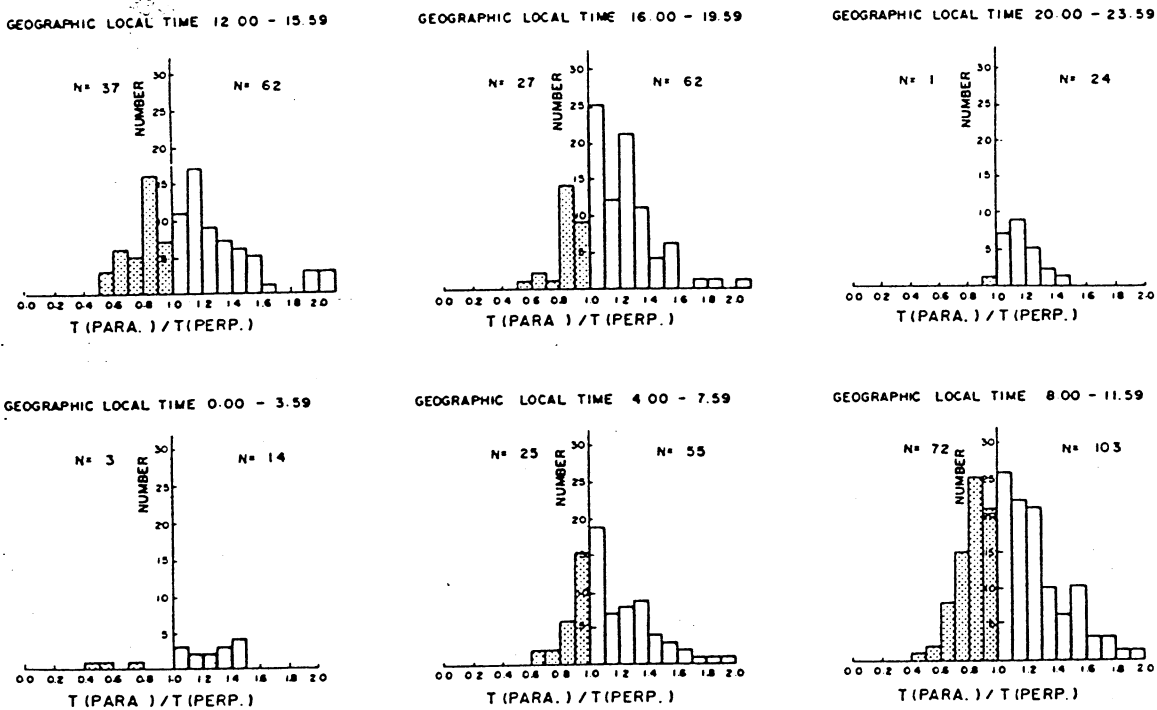
Fig. 7. Histograms of $R = T_{\parallel} / T_{\perp}$ for different local time periods.
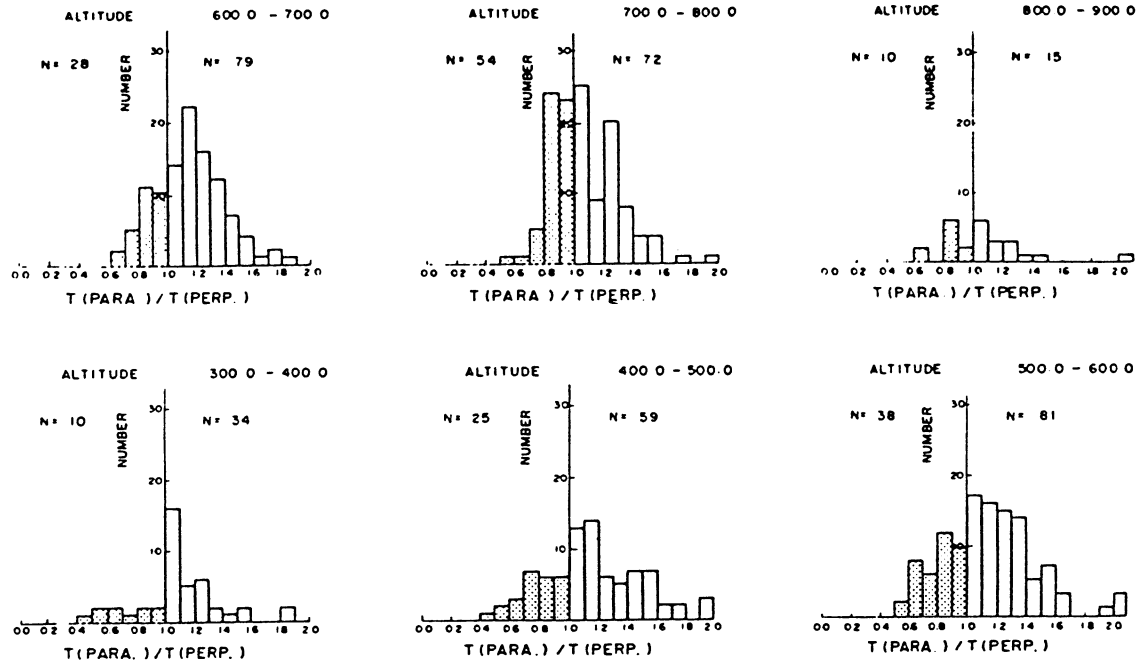
Fig. 8. Histograms of $R = T_\parallel / T_\perp$ for different height ranges.
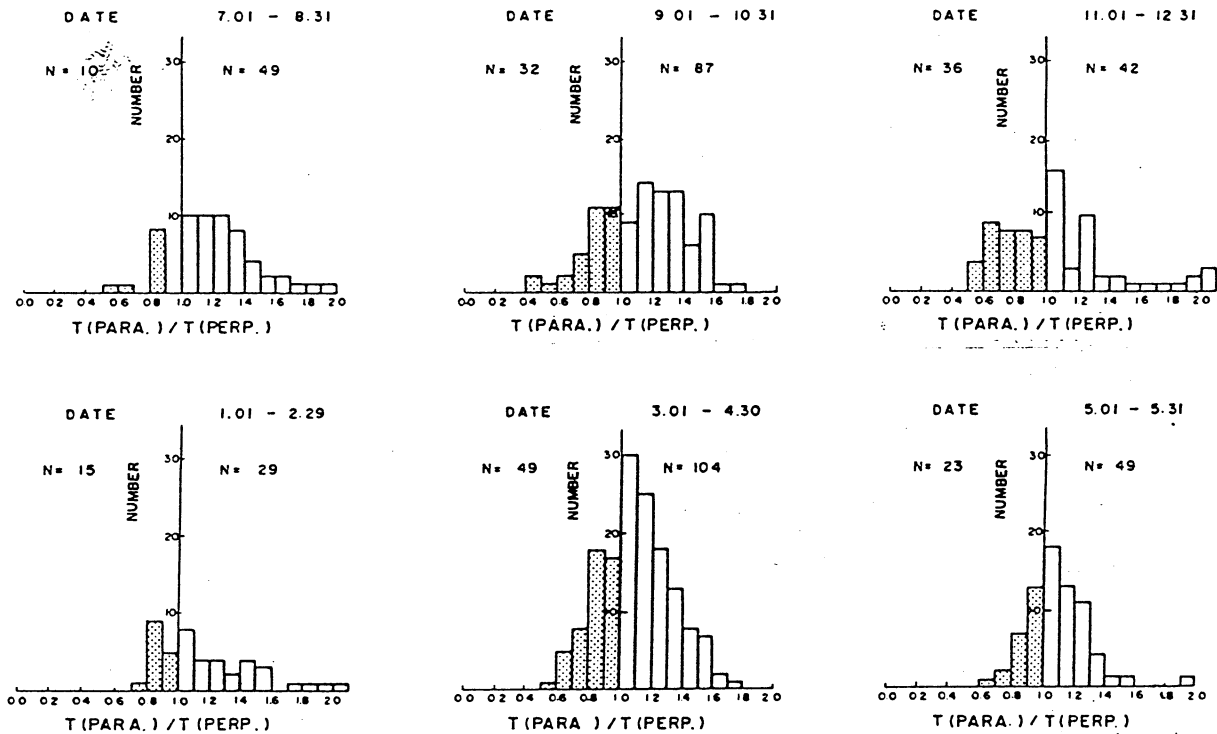
Fig. 9. Histograms of $R = T_\parallel / T_\perp$ or six bimonthly time periods starting January 1985.

32

2.4 Model Descriptions for the Ion Transition Heights

D. Bilitza
NASA/GSFC, NSSDC, Code 933
Greenbelt, Maryland 20771, U.S.A.

I. Kutiev
Bulgarian Academy of Sciences
Geophysical Institute
1113 Sofia, Bulgaria

Abstract—The ion composition in the upper and middle ionosphere exhibits two characteristic transition heights that mark the upper and lower boundaries of the region dominated by atomic oxygen ions. The upper transition height H_T is found at the point where the ion gas consists of equal parts of oxygen and light ions, and the lower transition height h_t where the oxygen density equals that of the molecular ions. We investigate the global and temporal morphology of these heights, summarizing the results of earlier studies. The use of these characteristic points for the IRI ion composition model is emphasized.

2.4.1 The Upper Transition Height

The ion gas of the topside ionosphere consists mainly of O^+, H^+, and He^+ ions. O^+ and He^+ ions are produced by photoionization, whereas the main source of H^+ ions is the charge exchange reaction between H and O^+. Production and loss together with redistribution by diffusion and ion drift are the major processes that shape the distribution of the different ion species. Figure 1, taken from the work by Raitt et al. (1975), shows O^+ and H^+ profiles for different upper boundary conditions. As a result of the difference in ion mass and because of the charge exchange reaction, the amount of O^+ ions decreases with altitude, whereas the percentage of light ions increases. The transition height H_T is defined as the height at which equal parts of O^+ and light ions are present. H_T depends strongly on the ion flow conditions at the plasmaspheric boundary, as is shown in Figure 1. Thus, H_T is a critical parameter in specifying and assessing the topside ion gas. Several studies (see Table 1) have examined the global and temporal variation of this characteristic height.

In summary, these investigations established the following characteristic variation patterns:

- The diurnal variation of H_T follows the change in O^+ density, being lowest at night and largest during daytime. H_T can drop down to as low as 500 km during nighttime and is rarely below 800 km during daytime.

- During daytime H_T is lowest at the magnetic equator and increases towards higher latitudes. This is caused by a similar change in plasma temperatures. Higher temperatures shift the ion density profiles upward.
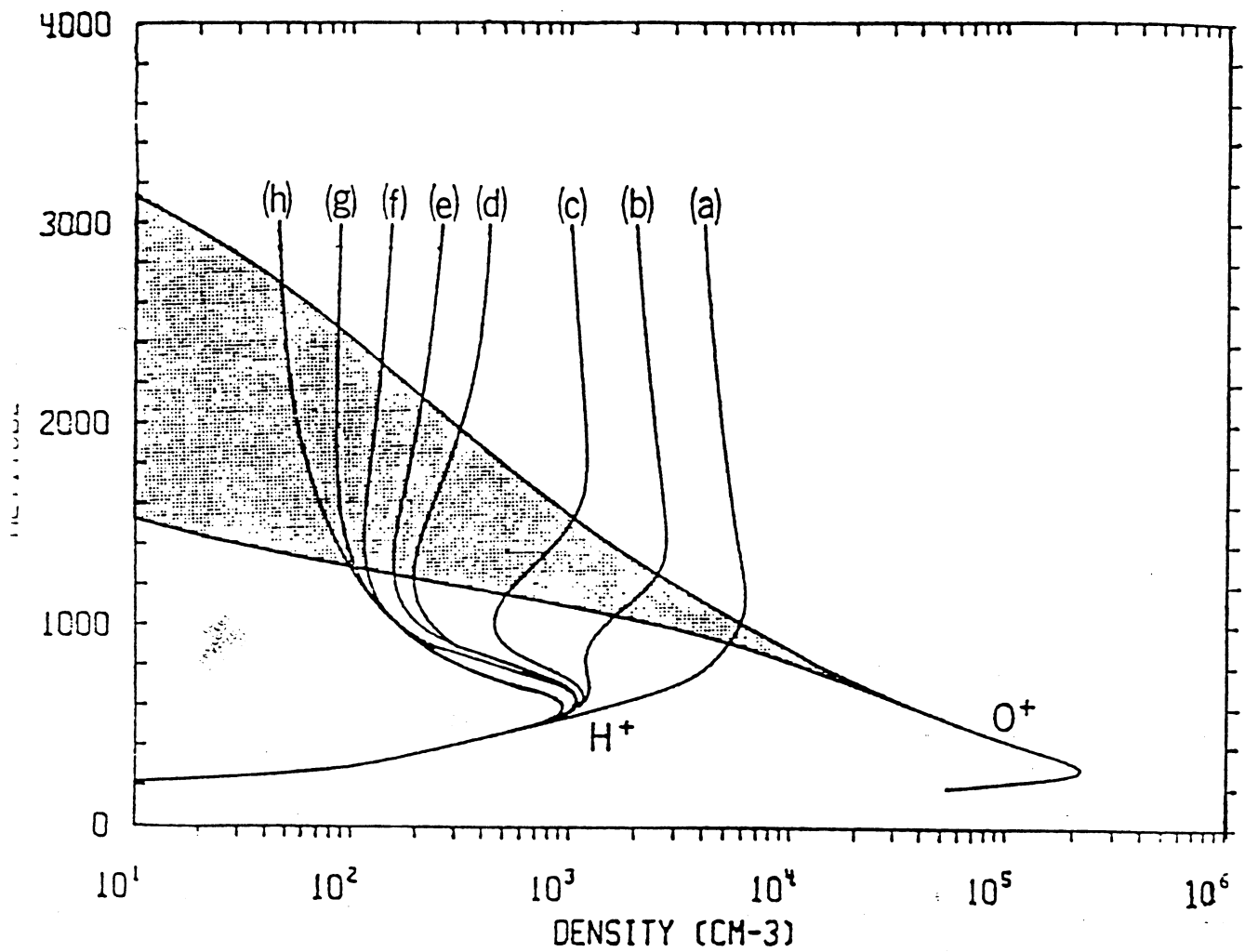
Fig. 1. Theoretical H+ and O+ density profiles as a function of altitude for different H+ velocities at 3000 km. The H+ velocities at the upper boundary in units of km/sec are (a) 0.06, (b) 0.34, (c) 0.75, (d) 2.0, (e) 3.0, (f) 5.0, (g) 10.0, and (h) 20.0. The shaded region shows the range of O+ densities; the lower boundary corresponding to H+ profile (a) and the upper boundary to (h) (Raitt et al., 1975).

Table 1: H_T Studies and Typical Values

Author	Data Used	Solar Activity	H_T/km Day Geomagnetic Latitude Low	H_T/km Day Geomagnetic Latitude Middle	H_T/km Night Geomagnetic Latitude Low	H_T/km Night Geomagnetic Latitude Middle
Brinton et al. (1970)	Explorer 32 IMS[†]	Low	1300	1900	–	–
Goel et al. (1970)	OGO 4 Explorer 31 RPA	Medium	1300	1600	700	700
Titheridge (1976)	Alouette 1 ISIS 1 Topside Sounder	Low	800 (800)	1200 (1200)	650	700 (550)
Miyazaki (1979)	Taiyo RPA[††]	Low	800 (800)	1100 (950)	600 (600)	550 (550)
Kutiev et al. (1984)	OGO 6 RPA	High	–	–	1100	800
Bilitza (1984)	Incoherent Scatter	Low	1400	>1500	700	1100

* Summer value; winter value in brackets.
† IMS = ion mass spectrometer.
†† RPA = retarding potential analyzer.

- H_T is higher in summer than in winter by 100 km to 200 km. An interhemispherical proton flux from the summer to the winter ionosphere is thought to be the reason for this difference (Brinton et al., 1970).

- H_T increases with solar activity. Titheridge (1976) finds nighttime transition heights about 500 km during solar minimum and about 1100 km at solar maximum.

There are, however, still quite a number of open questions and conflicting results that have to be resolved by future studies and measurements, for example:

- Table 1 shows that the earlier satellite measurements indicated generally higher transition heights than the more recent ones. There is also an obvious discrepancy between transition heights obtained by the incoherent scatter technique and those obtained by the in situ techniques.

- Kutiev et al. (1984) report considerable longitudinal changes in nighttime H_T obtained from OGO 6 RPA measurements, whereas the Taiyo RPA data (Miyazaki, 1979) exhibit a negligible longitudinal scatter.

Only a few investigators have attempted to represent their results by simple empirical relationships. Miyazaki (1979) used the following formulas to describe transition heights deduced from the Taiyo RPA measurements between March 1975 and October 1976.

$$H_T/\text{km} = \begin{cases} 591 - 87.1 \sin^2 \Psi & \chi > 90° \\ 591 - 87.1 \sin^2 \Psi + (217 + 473 \sin^2 \Psi)(\cos \chi)^{0.331} & \text{else} \end{cases}$$

Ψ is the magnetic dip latitude and χ the solar zenith angle. Kutiev et al. (1984b) used a power series in longitude and in magnetic dip latitude to represent the nighttime H_T deduced from OGO 6 RPA data.

In Figure 2 we compare the transition height predicted by these two H_T models with transition heights obtained from the IRI ion composition models and from the ion composition model by Danilov and Yaichnikov (1985). For more information about the latter two models, see section 3.4, page 71, of this document. The diurnal variation of H_T is shown at the magnetic equator (Lima) and at a magnetic midlatitude location (Arecibo). The IRI model predicts considerably lower transition heights than the other models. It also produces unreasonably abrupt changes of H_T at sunrise and sunset. The nighttime H_T from the model by Kutiev et al. (1984b) is much higher than all the other predictions. H_T deduced from the ion composition model by Danilov and Yaichnikov (1985) agrees fairly well with Miyazaki's (1979) H_T model at midlatitudes. At the magnetic equator the need for further data acquisition and modeling work is most obvious: None of the four models has much in common with the others.

2.4.2 The Lower Transition Height

In the altitude range 100 km to 300 km the ionospheric ion gas consists mainly of O^+, O_2^+, and NO^+ ions. In the absence of electric fields the distribution of ions can be explained straightforwardly by the chemical balance of photoionization and recombination. As a result of these processes, the concentration of O^+ ions increases with altitude whereas the percentage of molecular ions decreases. At the transition height h_t the percentage of molecular ions has dropped to 50%.

Oliver (1975) investigated the diurnal variation of this characteristic height by examining 40 rocket IMS measurements from 1956 to 1971. He found that the data could be well represented by

$$h_t/\text{km} = hs + 203.7 + 24.7 \tanh(-(88.4 - \chi)/19.7)$$

The remaining seasonal variation was approximated in terms of annual and semi-annual terms varying with the day number d.

$$hs/\text{km} = -16.8 \cos((d + 22)\, 2\pi/365) - 9.4 \sin((2d + 10.5)\, 2\pi/365)$$
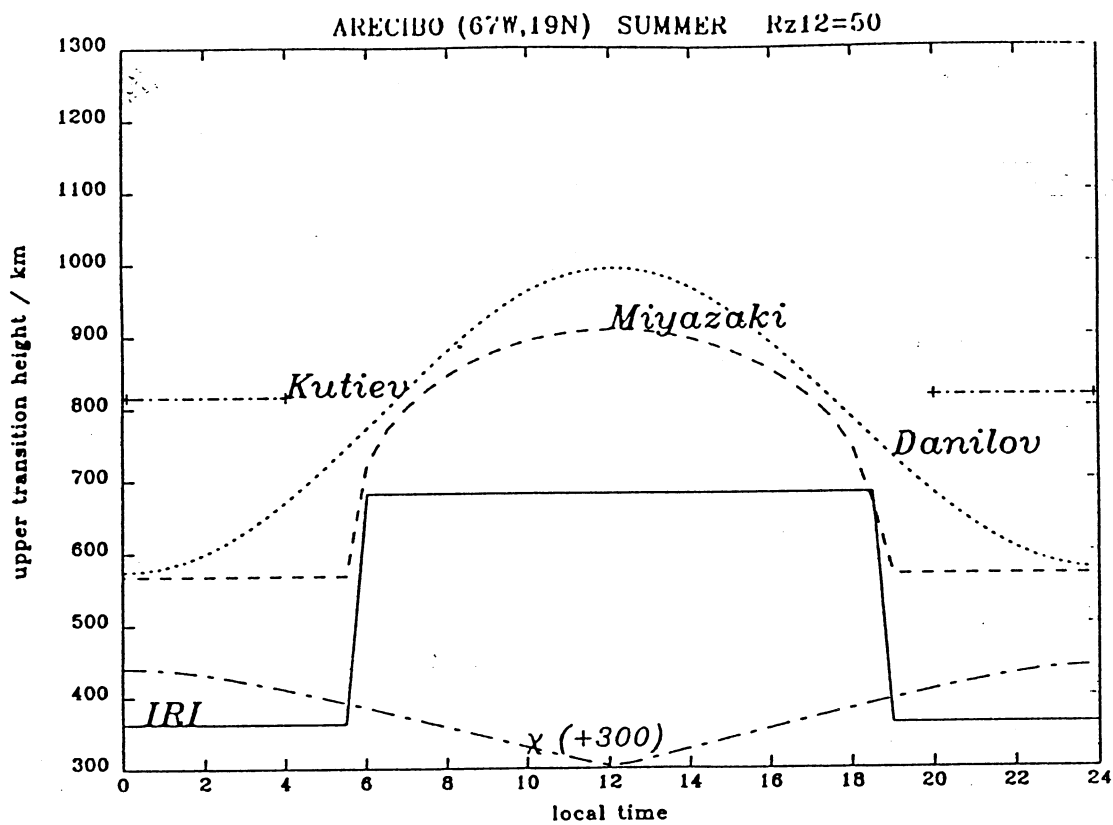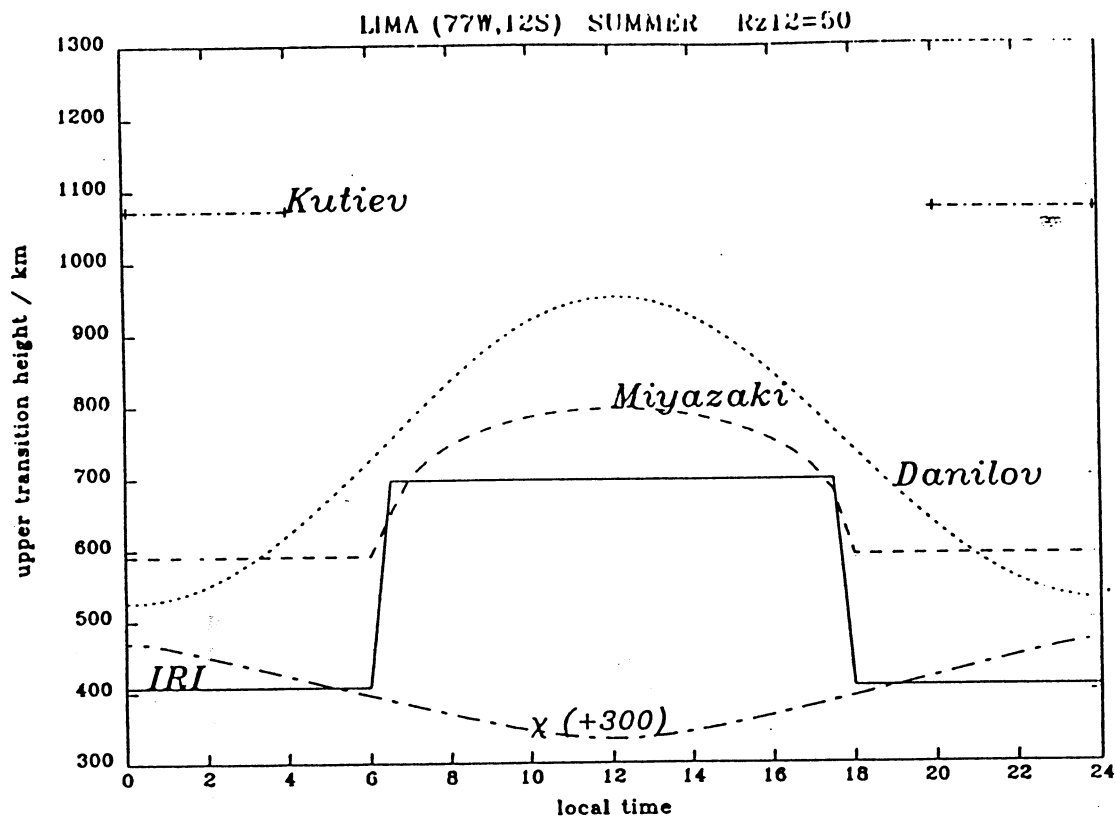
Fig. 2 a, b. Upper transition heights H_T obtained from the models by Miyazaki (1979), Danilov and Yaichnikov (1985), Kutiev et al. (1984), and from the IRI at the magnetic equator (top) and at a magnetic midlatitude location (bottom). Also shown is the solar zenith angle (plus 300).

Lathuillere and Brekke (1985) report good agreement between their EISCAT incoherent scatter results and Oliver's formula.

In Figure 3 the h_t values obtained with Oliver's (1975) model are compared with transition heights predicted by the IRI and by the ion composition model of Danilov and Yaichnikov (1985). At midlatitudes IRI agrees fairly well with Oliver's results, whereas the model by Danilov and Yaichnikov (1985) exhibits an unreasonably small change from day to night. At the equator IRI predicts the transition heights h_t much lower than the other two models.

2.4.3 Conclusion

The lower and upper ion transition heights are parameters which characterize and specify the ion composition profiles throughout most of the ionosphere. Our review has found only a few studies which examined the global morphology and the temporal change of these heights. Unfortunately, these studies have revealed somewhat conflicting results, in particular close to the magnetic equator. All three techniques used to evaluate transition heights have their specific accuracy problems. The ion mass spectrometers (IMS) and retarding potential analyzers (RPA) flown on long-lasting satellites missions have to deal with calibration problems and in-flight contamination effects. Ground-based incoherent scatter radars need long integration times or some assumptions about the plasma temperatures to deduce ion density ratios from the backscattered signal (Lathuillere et al., 1983).
Inconsistencies can only be resolved by comprehensive statistical studies of the data base accumulated so far and by a continued measurement program for these parameters from ground and space. It is clear that a better understanding of the variation patterns of the transition heights will significantly improve the modeling and prediction of ionospheric ion composition.
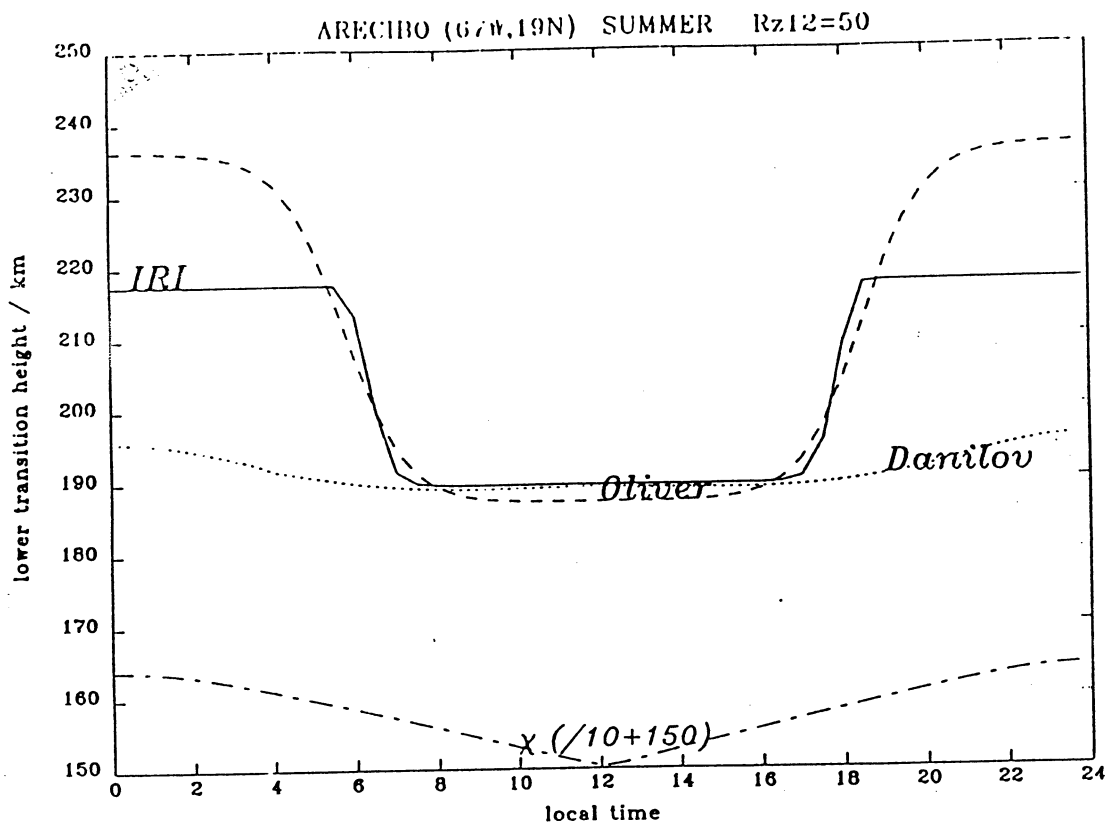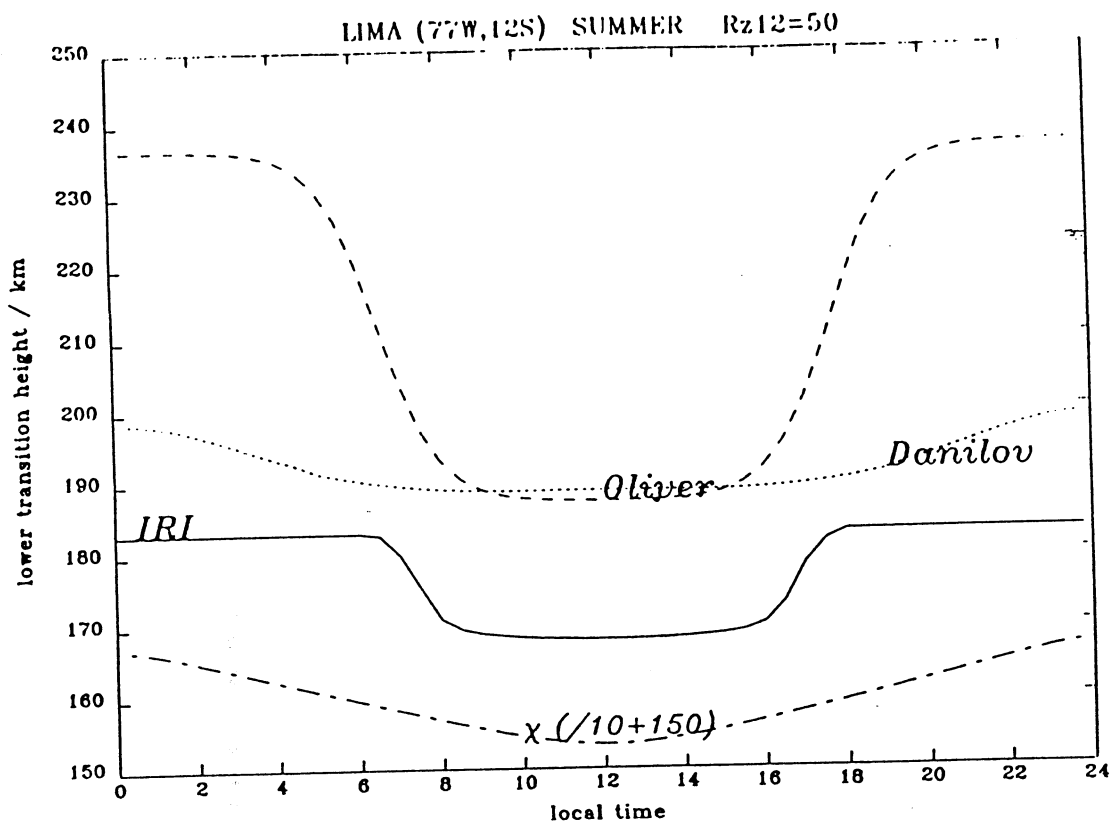
Fig. 3 a, b. Lower transition height h_t obtained from the models by Oliver (1975), Danilov and Yaichnikov (1985), and from the IRI at the magnetic equator (top) and at a midlatitude location (bottom). Also shown is the solar zenith angle (divided by 10; plus 150).

39

2.5 Models for Horizontal E- and F-Region Drifts

E. S. Kazimirovsky, E. I. Zhovty, and M. A. Chernigovskaya
Siberian Institute of Terrestrial Magnetism, Ionosphere,
and Radio Propagation (SibIZMIR)
664033, Post Box 4026
Irkutsk, U.S.S.R.

Abstract—E- and F-region horizontal ionospheric drift data, obtained worldwide from 1957 to 1970 by ground-based radio methods D1 and D3, are statistically analyzed and a computer code for the average variations in latitude and local time is constructed. This model has been adopted for the International Reference Ionosphere, IRI-90.

2.5.1 Data and Method

Plasma transport is very important for understanding the variations of the ionosphere in space and time. Therefore, the URSI/COSPAR Task Group on IRI has initiated an effort to construct a computer code that generates ion drifts for chosen location and local time.

A large quantity of experimental data obtained by measurement of horizontal ionospheric drifts is now available on a worldwide scale. The data we considered here were obtained by the spaced-receiver methods D1 and D3, as described by Briggs (1977). We have developed appropriate procedures that allow us to infer from these data the main parameters of the global ionospheric motion at E- and F-region levels (Vergasova et al., 1979).

Thus, following our earlier proposals (Kazimirovsky et al., 1984, 1985), we present here an analytical description of the dynamic behavior of the terrestrial ionosphere.

The experimental data are from 23 stations in the Northern Hemisphere and were obtained between 1957 and 1970. The worldwide coverage in geographic latitude is 7° to 71° north (7.5° to 64.1° north in geomagnetic latitude) and 0° to 131° east in geographic longitude.

2.5.2 The Drift Models

About 100000 individual drift velocity values in the E-region (90 km < h < 135 km) and F-region (h > 135 km) were statistically treated with sampling according to season and to solar activity as indicated in Table 1 and Table 2. Definition of seasons is as follows: December through February = winter, March through May = spring, June through August = summer, September through November = fall.

"SEASON = all" corresponds to the averaged velocities for the whole observed period. Three periods of solar activity are considered: (1) the whole solar activity range from minimum to maximum (all), (2) solar maximum (*F10.7* = 200), and (3) solar minimum (*F10.7* = 70). *F10.7* is the solar radio flux at 10.7 cm wavelength (Covington index).

Table 1: Analysis Periods for E-Region

PERIOD	1	2	3	4	5	6
SEASON	winter	spring	summer	fall	winter	spring
F10.7	all	all	all	all	200	200

PERIOD	7	8	9	10	11	12
SEASON	summer	fall	winter	spring	summer	fall
F10.7	200	200	70	70	70	70

Table 2: Analysis Periods for F-Region

PERIOD	1	2	3	4	5	6	7
SEASON	-	winter	spring	summer	fall	winter	spring
F10.7	all	all	all	all	all	200	200

PERIOD	8	9	10	11	12	13
SEASON	summer	fall	winter	spring	summer	fall
F10.7	200	200	70	70	70	70

An algorithm for computing the zonal and meridional drift components VX, VY can be found in section 3.5, page 75, of this document. It is written in PASCAL 8000 for IBM 360/370 compatible computers. The main block of the program is the procedure DRIRR for calculating VX and VY for a certain period (P), geomagnetic latitude (FI), and local time (LTT). VX and VY are first computed by Fourier development:

$$VX \ (LTT, \ FI) = X_0(FI) + \sum_{n=1}^{3} X_n \ (FI) \ \sin(n \ LTT + CX_n \ (FI))$$

$$VY \ (LTT, \ FI) = Y_0(FI) + \sum_{n=1}^{3} Y_n \ (FI) \ \sin(n \ LTT + CY_n \ (FI))$$

for six main latitudes FI = 10°, 20°, ... , 60°. Spline interpolation between these allows determination for any specified value of FI. The coefficients $X_n(FI)$, $Y_n(FI)$, $CX_n(FI)$, and $CY_n(FI)$ are contained in the files FAR1 and FAR2 listed in section 3.5, page 75, of this document.

Chapter 3

IRI-90: Formulas and Explanations

Contents

3.1 Introduction

IRI-90 describes monthly averages of electron density, electron temperature, ion temperature, and ion composition in the non-auroral, quiet ionosphere from 100 km to 1000 km.

3.1.1 Data Sources

The following data sources were used to establish IRI-90.

- Worldwide ionosonde measurements (peak plasma frequencies => peak densities)

- Incoherent scatter measurements from Jicamarca, Arecibo, St. Santin, Millstone Hill, and Malvern (E-valley, F2-peak height, F2-bottomside, topside, electron and ion temperature)

- Alouette 1, 2 topside sounder measurements (topside)

- AE-C, ISIS 1 and 2 in situ measurements (electron temperature)

- AEROS in situ measurements (electron and ion temperature, ion composition)

- Rocket measurements (D- and E-region electron density and ion composition)

- Beacon satellite data (ionospheric electron content for test purposes)

- Ground-based absorption measurements (D- and E-region variability)

3.1.2 Functions

A variety of analytical expressions and functions is used in IRI-90 to represent the temporal and spatial variations of the ionospheric densities and temperatures. Global variations (with latitude and longitude/local time) are in most cases described by a form of a spherical harmonics series (Legendre polynomials).

A group of functions introduced by S. Epstein has been used to represent altitudinal variations as well as special latitudinal and diurnal features. The first three members of the Epstein family of functions are shown in Figure 1 and defined as

$$EPS_{-1}(h; HX, SC) = \ln(1 + e^x) \qquad (3.1a)$$
$$EPS_0(h; HX, SC) = 1/(1 + e^{-x}) \qquad (3.1b)$$
$$EPS_1(h; HX, SC) = e^x/(1 + e^x)^2 \qquad (3.1c)$$

45
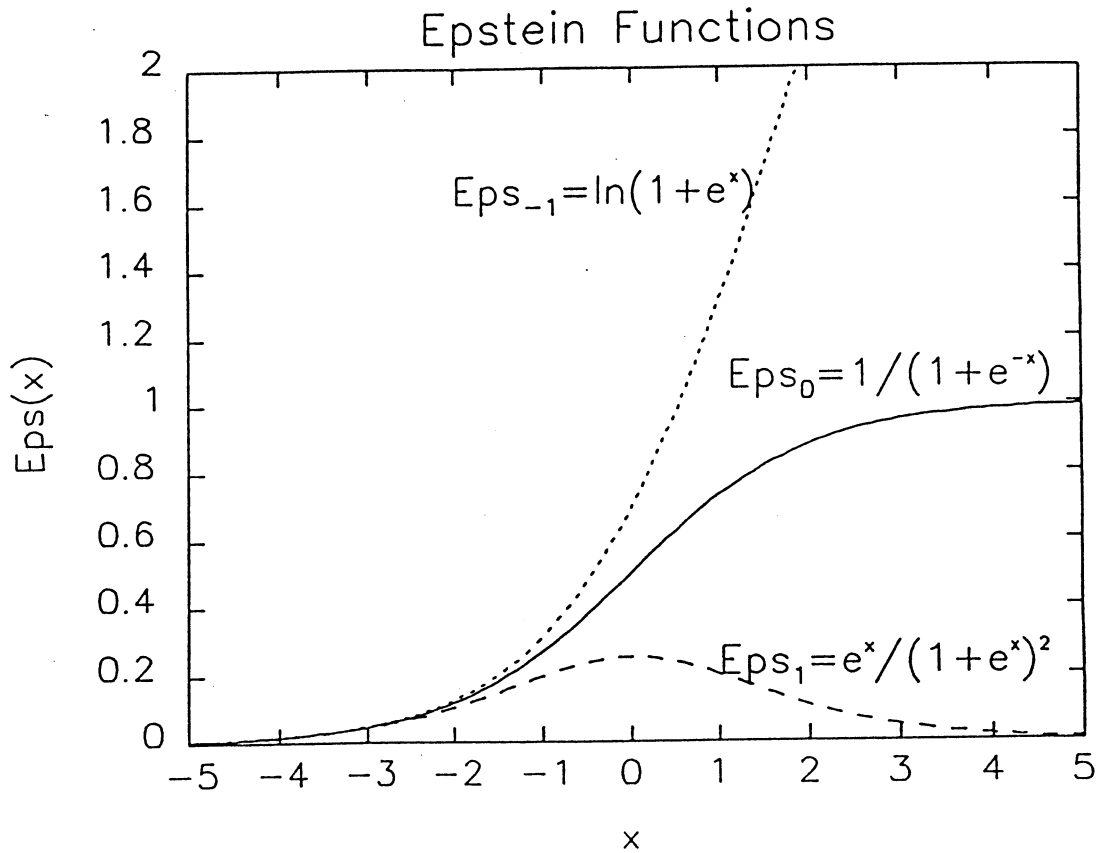
Fig. 1. Epstein functions.

with

$$x = (h - HX)/SC \tag{3.1d}$$

and

$$EPS_{i+1} = d\ EPS_i/dx \tag{3.1e}$$

EPS_{-1} describes a transition, EPS_0 a step, and EPS_1 a peak at $h = HX$ with the width SC. Three combinations of Epstein functions are explained in the following sections. All three have been used repeatedly in constructing the IRI profiles.

The Epstein step function can also provide a type of filter function taking the value 0 below a certain altitude and the value 1 above. Rawer (1987) explained how three such filter functions can be used for a joint analytical representation of the whole electron density profile.

3.1.2.1 <u>Booker Profile Function</u>

A parameter Y, which steps from a value Y_1 to a value Y_2 at $h = h_s$, can be described by the function

46

$$\text{EPSTEP}(h; Y_1, Y_2, h_s, d_s) = Y_1 + (Y_2 - Y_1)\ \text{EPS}_0(h; h_s, d_s) \tag{3.2}$$

d_s determines the width of the transition region. Booker's (1977) approach uses several such steps. He assumes that the altitudinal profile of a parameter y can be divided into several subsections such that in each subsection y can be fairly well approximated by a straight line or, in other words, that the gradient dy/dh is nearly constant in every subsection (e.g., Figure 5). Booker calls this the skeleton profile. The derivative of the skeleton function can then be represented by a sum of EPSTEP functions, stepping from subsection to subsection. Integrating from h_0 to h, we obtain y in terms of the "Booker function" B.

$$y(h) - y_0 = B(h; h_0, M, DY, HX, SC)$$

$$= (h - h_0)\ DY_1 + \sum_{j=1}^{M} (DY_{j+1} - DY_j)\ SC_j\ (\ \text{EPS}_{-1}(h;\ HX_j,\ SC_j)$$

$$- \text{EPS}_{-1}(h_0;\ HX_j,\ SC_j)\ ) \tag{3.3}$$

M is the number of subsections, DY_j ($j = 1$ to $M + 1$) are the constant gradients in these subsections, HX_j ($j = 1$ to M) are the subsection boundaries, and SC_j ($j = 1$ to M) are the thicknesses of the transition zones between subsections. y_0 is the integration constant, with $y(h_0) = y_0$. Suitable transition thicknesses SC_j have to be found by trial and error. Small SC_j values produce a profile closer to the skeleton than to the real profile; large SC_j values provide greater smoothness but could cause interference between adjacent step functions. Best results are obtained with

$$D/20 \le SC_j \le D/10 \tag{3.4a}$$

where D is the height range of the smaller of the two adjacent subsections

$$D = \min\ (h_j - h_{j-1},\ h_{j+1} - h_j) \tag{3.4b}$$

Care has also to be taken in choosing the anchor point (integration boundary) h_0. It should not be located in one of the highly variable transition regions. The best choice is a h_0 from a region where the skeleton and the original profile are close together. These constraints make it difficult to represent layer profiles with Booker's method. A profile peak can be approximate by either two skeleton lines whose gradients have opposite sign or by three skeleton lines, where the gradient of the middle one is zero. In the first case, the tip of the layer is in the middle of the transition zone and the peak height cannot be used as anchor point h_0. In the second case, condition (3.4) will almost always be violated.

3.1.2.2 Rawer Lay(er) Function

A better way of representing layer shape was introduced by Rawer (1984). His LAY function combines the Epstein transition function with a linear term.

$$LAY\ (h;\ hm,\ HX,\ SC) = \ EPS_{-1}(h;\ HX,\ SC) - EPS_{-1}(hm;\ HX,\ SC)$$

$$- (h - hm)\ EPS_0(hm;\ HX,\ SC)/SC \qquad (3.5)$$

It peaks at $h = hm$, where it takes zero value. A wide variety of layer shapes can be represented by the LAY function as shown in Figure 2. The appropriate HX and SC values can be found by a non-linear least-square-fit procedure.

3.1.2.3 Day-Night Transition Function

Epstein step functions are also used to describe simple day-night variations of ionospheric parameters. The combination of two step functions

$$HPOL(t;\ Y_D,\ Y_N,\ SR,\ SS) = \ Y_N + (Y_D - Y_N)\ EPS_0(t;\ SR,\ TD)$$

$$+ (Y_N - Y_D)\ EPS_0(t;\ SS,\ TD) \qquad (3.6)$$

varies with local time t continuously from a constant nighttime value Y_N to a constant daytime value Y_D. The steps occur at the local times of sunrise SR and sunset SS and the step width is determined by TD (usually one hour). This local time variation is used for all parameters for which only day and night values are listed.
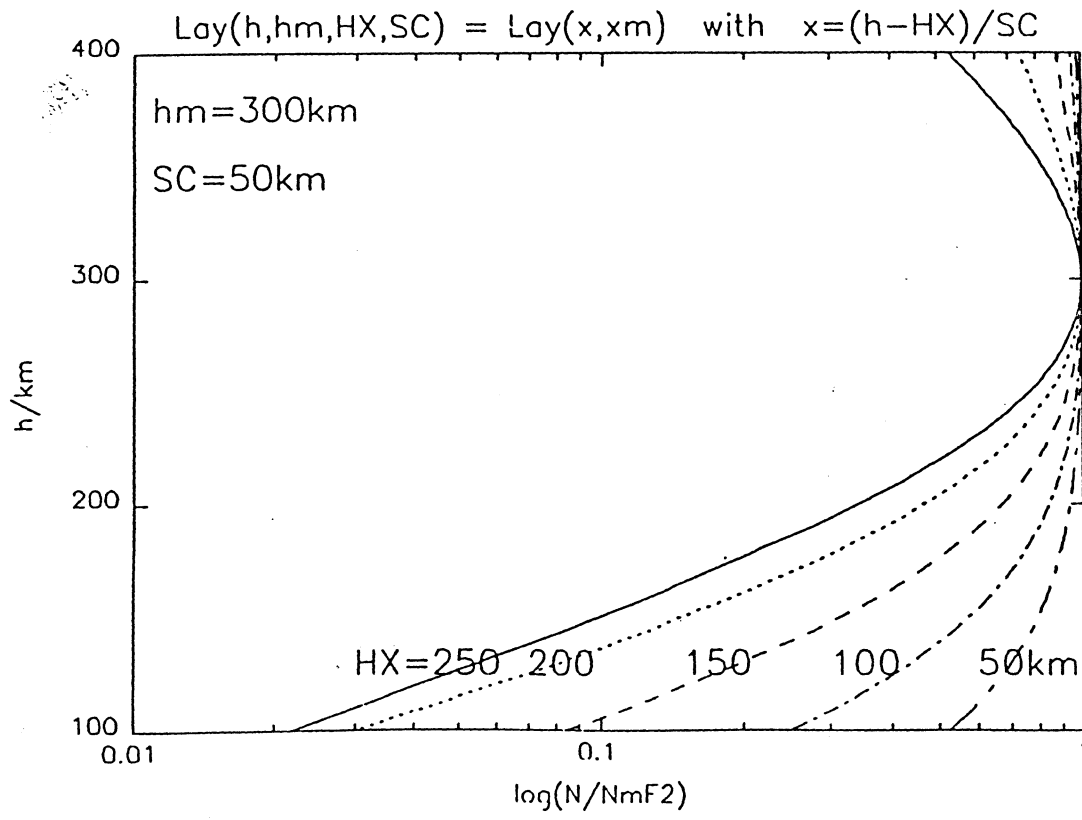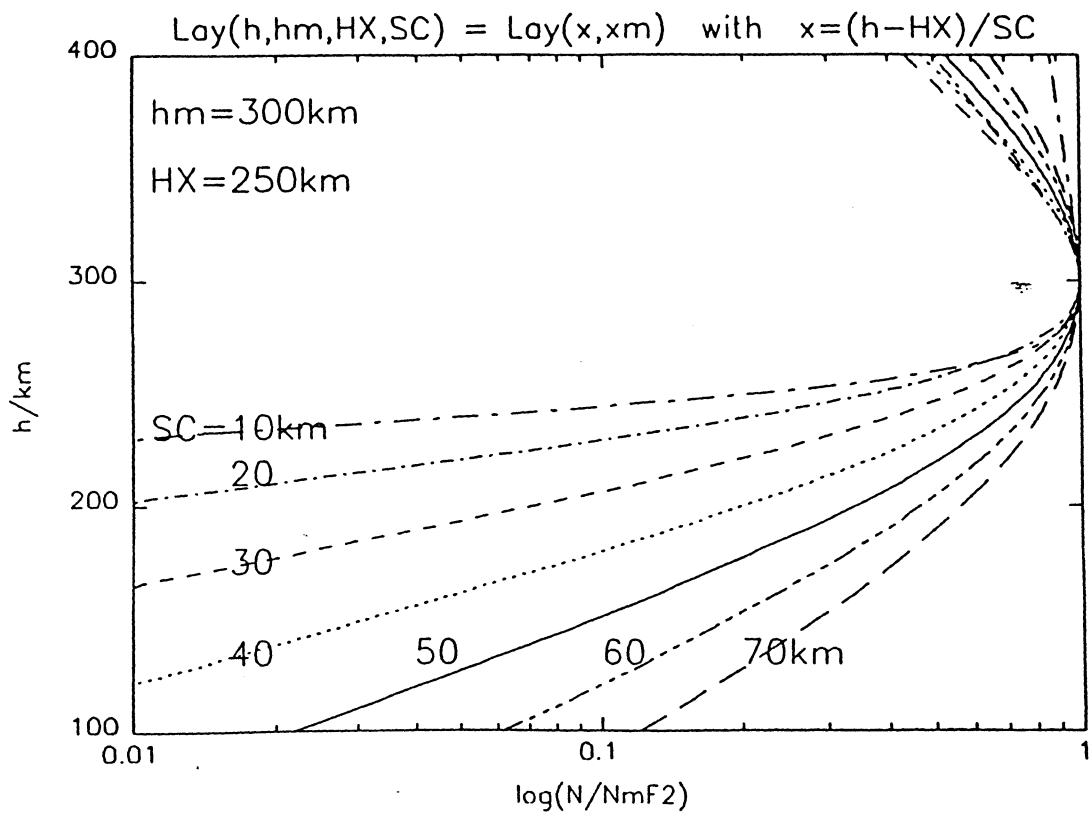
Fig. 2. Rawer's LAY function for a variety of *HX* and *SC* values.

1.2 Electron Density

The IRI electron density profile is divided into six subregions as shown in Figure 3, including the topside, the F2-bottomside, the F1-layer, the intermediate region, the E-valley, and the E-bottomside and D-region. The boundaries of these subsections are marked by several characteristic profile points including the F2-, F1-, and E-layer peaks. The critical frequencies foF2, foF1, and foE of these peaks have been monitored by the worldwide network of ionosondes since the forties. A radio wave with the critical frequency foF2 transmitted vertically from the ground will be reflected at the F2-peak. The squares of the critical frequencies are proportional to the electron density at the height where reflection occurs,

$$NmF2/\text{m}^{-3} = 1.24 \ 10^{10} \ (foF2/\text{MHz})^2 \qquad (3.7)$$
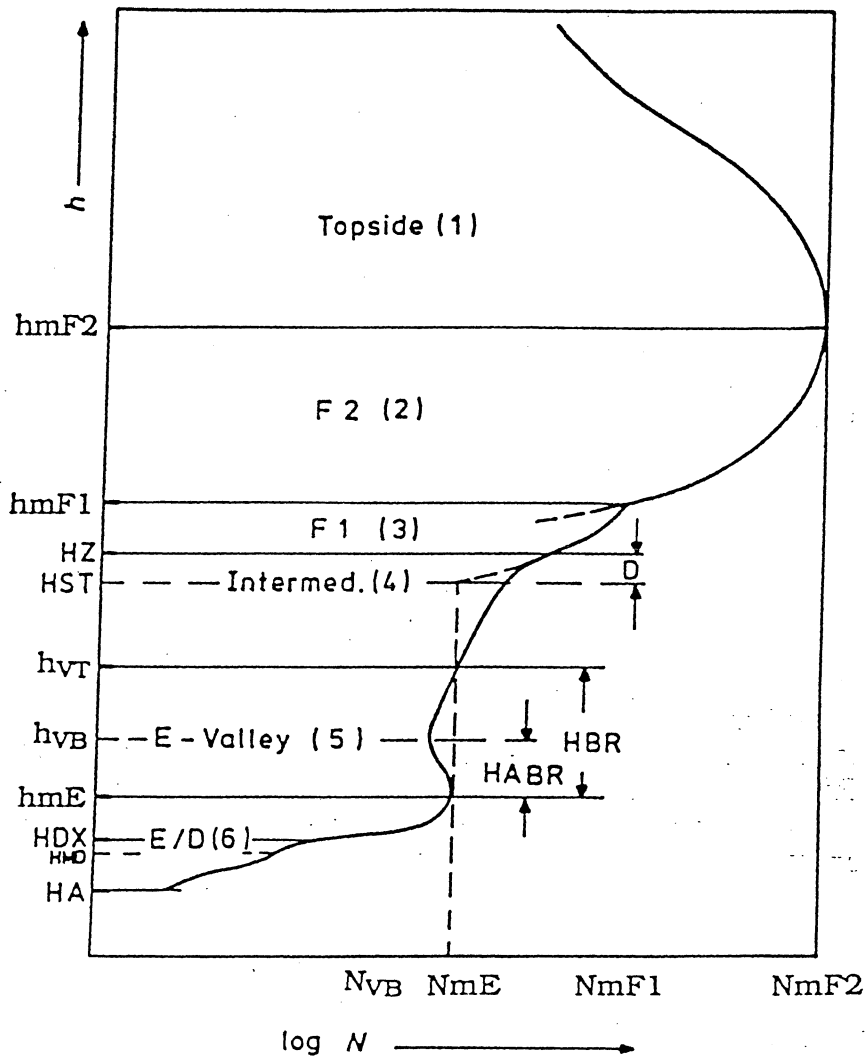
Fig. 3. Buildup of IRI electron density profile.

3.2.1 Topside (*hmF2* to 1000 km)

The topside profile is normalized to the F2-peak density *NmF2* and altitude *hmF2*.

3.2.1.1 F2-Peak Density (*NmF2, foF2*)

IRI-90 offers two choices for the description of the F2 critical frequency *foF2* (and therefore *NmF2*): (1) the model recommended by the International Radio Consultative Committee (CCIR, 1967) and (2) the one recently proposed by the International Union of Radio Science (URSI, Rush et al., 1989). The mathematical description is the same in both cases. It is based on first Fourier analysis (seventh order, 15 coefficients) of the monthly median diurnal variation as observed by the worldwide network of ionosondes, and secondly, a worldwide description in terms of spherical (Legendre) functions, separately found for each of the 15 coefficients (Jones and Gallet, 1965). Two sets of 988 coefficients each are given for each month, one for low and one for high solar activity (R_{12} = 0, 100); *foF2* for intermediate activities is found by linear interpolation.

For very high solar activities *foF2* observations indicate a saturation effect. In IRI this effect is enforced by keeping *foF2* constant above R_{12} = 150. (See Equation [3.13d]).

Because of the strong magnetic control of F-region processes, it is advantageous to use a magnetic field coordinate in the global analysis. The best results were obtained with the modified dip latitude (short: Modip), μ, introduced by Rawer (1963)

$$\tan \mu = \psi / \cos^{1/2}\varphi \qquad (3.8)$$

which at low latitudes is near the magnetic inclination (short: dip), ψ, and gets closer to the geodetic latitude φ as latitude increases.

For the newer URSI model, the data sparse regions (oceans, Southern Hemisphere) were first populated with *foF2* values obtained by aeronomic theory and then the analysis procedure was applied (Rush et al., 1984, 1985). The URSI coefficient set provides a somewhat better representation of ocean *foF2* values than the CCIR model, when compared with ISS-b topside sounder measurements (Rush et al., 1989). Recent reviews of *foF2* modeling were given by Bilitza et al. (1987) and Bradley (1990).

3.2.1.2 F2-Peak Height (*hmF2, M(3000)F2*)

The F2-peak height *hmF2* is obtained by its close correlation with the propagation parameter *M(3000)F2* (Shimazaki, 1955; for review, see Bradley and Dudeney, 1973, and Bilitza et al., 1979). *M(3000)F2* is defined as

$$M(3000)F2 = MUF/foF2 \qquad (3.9)$$

where *MUF* is the maximum usable frequency that, refracted in the ionosphere, can be received at a distance of 3000 km. This factor has been routinely scaled from ionograms, and numerical maps (CCIR, 1967) have been established in the same way as described above for *foF2*. *hmF2* is calculated from *M(3000)F2* with the empirical formula (Bilitza et al., 1979)

$$hmF2/km = 1490/(M(3000)F2 + DM) - 176 \qquad (3.10a)$$

with the correction factor

$$DM = f_1 f_2/(foF2/foE - f_3) + f_4 \qquad (3.10b)$$

and the solar activity functions

$$f_1 = 0.00232\, R_{12} + 0.222 \qquad (3.10c)$$

$$f_2 = 1 - R_{12}/150 \exp(-(\Psi/40)^2) \qquad (3.10d)$$

$$f_3 = 1.2 - 0.0116 \exp(R_{12}/41.84) \qquad (3.10e)$$

$$f_4 = 0.096\,(R_{12} - 25)/150 \qquad (3.10f)$$

R_{12} is the 12-months-running mean of solar sunspot number and Ψ is the magnetic dip latitude

$$\tan\Psi = \frac{1}{2}\tan\psi \qquad (3.11)$$

which is related to the magnetic inclination (short: dip) ψ of the Earth's magnetic field at 300 km altitude.

Formula (3.10) is based on the work by Shimazaki (1955), who was the first to describe the strong anti-correlation between *hmF2* and *M(3000)F2*, and the work by Bradley and Dudeney (1973), who were the first to take account of the effect of the E-layer ionization on the correlation. Bilitza et al. (1979) used incoherent scatter data to improve the earlier relationships, which were based on the, generally, less reliable *hmF2* values deduced from ionosonde recordings.

3.2.1.3 Topside Profile Shape

The topside model is based on the descriptive compilation of Alouette topside sounder data by Bent and his colleagues (Llewellyn and Bent, 1973). Epstein functions are used to obtain an analytical representation of the values given by Bent in tabular form.

$$N(h)/NmF2 = \exp(-1/\alpha \cdot B(x; x_0, 2, TG, TX, TC)) \qquad (3.12a)$$

B is the Booker function explained in section 3.1.2.1 (Equation [3.3]) and x is a modified altitude variable transforming the F2-peak to near 300 km

$$x - x_0 = \alpha \ (h - hmF2) \tag{3.12b}$$

with the transformation factor

$$\alpha = 700/(1000 - hmF2) \tag{3.12c}$$

and the new peak height

$$x_0 = 300 - \delta \tag{3.12d}$$

The Epstein parameters for the topside profile are given in Table 1.

Table 1: Epstein Parameter for Topside Formula

j	TG	TX	TC
1	$-\xi$	300	100
2	0	394.5	β
3	η	—	—

The parameters ξ, η, β are functions of the geomagnetic latitude ϕ, the monthly solar radio flux $F10.7$, and the F2 critical frequency $foF2$

$$\xi, \eta, \beta = t_0 + t_1 \ T_m(\phi) + t_2 \ R(F10.7) + t_3 \ T(\phi) \ R(F10.7) +$$

$$t_4 \ foF2 + t_5 \ foF2 \ T(\phi) + t_6 \ foF2^2 \tag{3.13a}$$

where

$$T(\phi) = \cos^2\phi \tag{3.13b}$$

$$T_m(\phi) = \begin{cases} EPS_1(\phi, \ 0, \ 15) & \text{for } \eta \\ \cos^2\phi & \text{for } \xi \ \beta \end{cases} \tag{3.13c}$$

$$R(F10.7) = \begin{cases} (F10.7 - 40)/30 & \text{for } F10.7 < 193 \\ 5.1 & \text{else} \end{cases} \tag{3.13d}$$

The coefficients t_i were determined by fitting these functions to the corresponding values obtained from Bent's tabulation and are listed in Table 2.

Table 2: Topside Profile Parameters

	η	ξ	β
t_0	0.058798	0.078922	−128.03
t_1	−0.08	−0.0046702	20.253
t_2	−0.014065	−0.019132	−8.0755
t_3	0.0069724	0.0076545	−0.65896
t_4	0.0024287	0.0032513	0.44041
t_5	0.004281	0.006029	0.71458
t_6	−0.0001528	−0.00020872	−0.042966

The corrective term δ is related to η, ξ, and β by

$$\delta = \left(\frac{\eta}{1+Z} - \frac{\xi}{2} \right) / \left(\frac{\eta}{\beta} \frac{Z}{(1+Z)^2} + \frac{\xi}{400} \right) \qquad (3.14a)$$

with

$$Z = \exp(94.45/\beta) \qquad (3.14b)$$

It should be noted that the parameters TG, TX, and TC for the Booker function were obtained by a least-square-fit procedure, rather than from a skeleton profile as originally intended by Booker (1977) (see section 3.1.2.1, page 46). Thus, the topside representation is closer to the LAY formalism (see section 3.1.2.2, page 48) as pointed out by Rawer (1987). Rearranging formula (3.12a) in terms of LAY functions (Equation [3.5]), one obtains

$$N(h)/NmF2 = \exp(-\beta\eta/\alpha \; LAY\; (x; x_0, 394.5, \beta) -$$

$$100 \frac{\xi}{\alpha} LAY\; (x; x_0, 300, 100) - (h - hmF2) \; \gamma) \qquad (3.15a)$$

where

$$\gamma = \eta/(1 + \exp((\delta + 94.5)/\beta)) + \xi/(1 + \exp(\delta/100)) - \xi \qquad (3.15b)$$

In general, γ is so small that the linear term can be neglected in computing the argument of the exponential function, at least in the lower topside.

Good agreement was found in comparisons of IRI with AEROS and AE-C satellite data and with Jicamarca incoherent scatter measurements (Bilitza, 1985a). Buonsanto (1989) reported that IRI overestimates the electron densities observed by the Millstone Hill incoherent scatter radar. A comparison with DE 2 satellite data indicated that IRI topside density may be too low for very high solar activities (Bilitza et al., 1987).

3.2.2 Bottomside ($hmF1$ to $hmF2$)

The bottomside profile description was established by Ramakrishnan and Rawer (1972). It is defined as (see also Figure 4)

$$N(h)/NmF2 = \exp(-x^{B_1})/\cosh(x) \qquad (3.16a)$$

with

$$x = (hmF2 - h)/B_0 \qquad (3.16b)$$

$NmF2$ and $hmF2$ are the electron density and height of the F2-peak, and B_1 is equal to 3 in most cases (see section 3.2.4, page 59, for exceptions). IRI-90 offers two choices for the bottomside thickness parameter B_0: (1) a table of values (Table 3) based on reduced ionosonde profiles as in previous editions of IRI, and (2) Gulyaeva's (1987) model for the half-density height $h_{0.5}$. In most cases, the newer model (option [2]) is the better choice, especially at low latitudes.

Table 3: Bottomside Thickness Parameters B_0 Deduced from Ionograms Recorded at Mexico City, Huancayo (Peru), and Lindau (F.R.G.)

B_0/km		Spring		Summer		Fall		Winter	
		LT=12	LT=0	LT=12	LT=0	LT=12	LT=0	LT=12	LT=0
Modip =18	R=10	114	64	134	77	128	66	75	73
	R=100	113	115	150	116	138	123	94	132
Modip =45	R=10	72	84	83	89	75	85	57	76
	R=100	102	100	120	110	107	103	76	86

Interpolation Rules: R (12-months-running mean value): Linear interpolation.
LT (local time): Day-night transitions; see section 3.1.2.3, page 48.
Modip (modified dip, μ, Equation [3.8]): EPSTEP (μ; B_0 (18), B_0 (45), 30, 10); see section 3.1.2.1, page 46. B_0 is kept constant for $|\mu| < 18$.

Gulyaeva (1987) has established, based on ionosonde data, the following relationship between the F2-peak height, $hmF2$, and the height, $h_{0.5}$, where the density profile has decreased to half the F2-peak density

$$\rho = h_{0.5}/hmF2 = \text{EPSTEP } (x; 0.6, 0.8, 20s, 15) \qquad (3.17)$$

with the seasonal parameter s taking the values 1, 2, 3 for winter, equinox, and summer, respectively, or using the day number d approximately

$$s(d) = 2 - \cos(2\pi/365 \cdot d) \qquad (3.18)$$
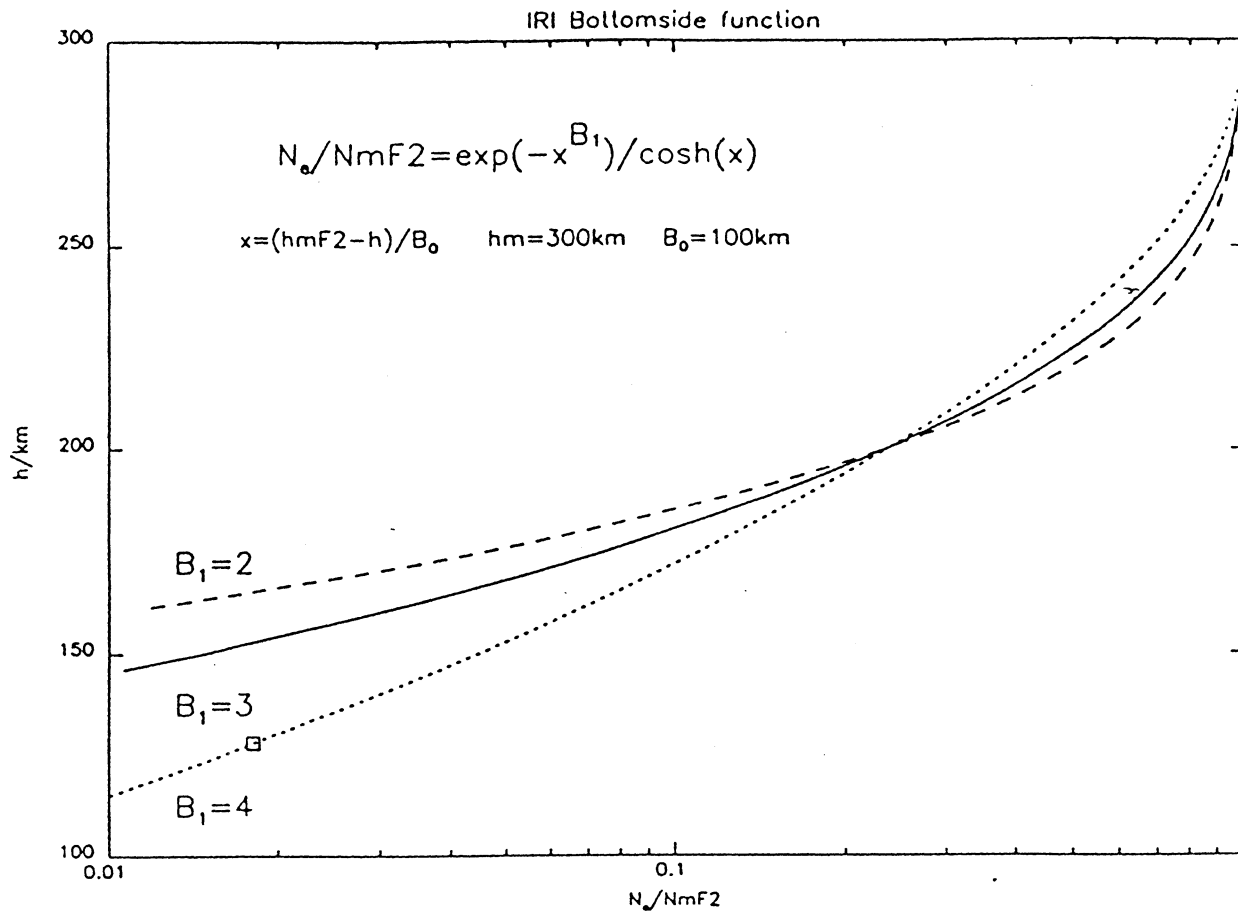
Fig. 4. Bottomside function for various B_1 values.

Assuming a bottomside profile as given by Function (3.16), one can use Gulyaeva's model to determine the thickness parameter B_0 (Bilitza and Rawer, 1990).

$$B_0 = hmF2 \, (1 - \rho)/C \qquad (3.19)$$

where C is a function of B_1 and takes the values

B_1	3	3.5	4	4.5	5
C	0.755566	0.778596	0.797332	0.812928	0.82614

Gulyaeva's (1987) model has also shown good agreement with incoherent scatter measurements at Arecibo (Mahajan and Kohli, 1987).

3.2.3 F1-Layer ($hmF1$ to HZ)

Ducharme et al. (1971, 1973) established, based on a large amount of ionosonde data, the following relationship for the variation of the F1 plasma

frequency $foF1$ with solar zenith angle χ, solar activity (R_{12}), and magnetic dip latitude (Ψ).

$$foF1 = fs \cos^n \chi \qquad (3.20a)$$

$$f_s = f_0 (f_{100} - f_0) R_{12}/100 \qquad (3.20b)$$

$$f_0 = 4.35 + 0.058 |\Psi| - 0.00012 \Psi^2 \qquad (3.20c)$$

$$f_{100} = 5.348 + 0.011 |\Psi| - 0.00023 \Psi^2 \qquad (3.20d)$$

$$n = 0.093 + 0.0046 |\Psi| - 0.000054 \Psi^2 + 0.0003 R_{12} \qquad (3.20e)$$

Their model provides also a critical solar zenith angle χ_s for the occurrence probability of the F1-feature. An F1-layer is only assumed to exist when the solar zenith angle is smaller than χ_s.

$$\chi_s = \chi_0 (\chi_{100} - \chi_0) R_{12}/100 \qquad (3.21a)$$

$$\chi_0 = 49.85 + 0.35 |\Psi| \qquad (3.21b)$$

$$\chi_{100} = 38.96 + 0.51 |\Psi| \qquad (3.21c)$$

IRI omits the F1-feature at night and in winter in accordance with the experimental evidence.

The F1-peak height, $hmF1$, is found as the height at which the bottomside IRI profile reaches the F1-peak density. It is important to notice that $hmF1$ will be affected by the choice of the bottomside thickness parameter B_0, for which in IRI-90 two options are given, as described in the previous section. Bilitza and Rawer (1990) indicated that option (2), Gulyaeva's (1987) model, produces $hmF1$ values closer to other estimates for this parameter (e.g., Formula [3.33]).

If the F1 feature exists, a parabolic F1-layer is added to the bottomside profile

$$N(h)/NmF2 = \exp(-x^{B_1})/\cosh(x) + C_1 ((hmF1 - h)/B_0)^{1/2} \qquad (3.22a)$$

with

$$C_1 = \begin{cases} \text{EPSTEP } (18; 0.09, 0.2, 30, 10) & \text{for } |\mu| < 18 \\ \text{EPSTEP } (\mu; 0.09, 0.2, 30, 10) & \text{else} \end{cases} \qquad (3.22b)$$

where μ is the modified dip latitude (Equation [3.8]) and the EPSTEP function is given in Equation (3.2).

3.2.4 Intermediate Region (HZ to h_{VT})

This is the region where the upper profile (normalized to $NmF2$) is merged with the lower profile (normalized to NmE). First, the height HST is found where the F1 profile function reaches the density value of the E-peak, NmE (see Figure 3). It may occur that the profile function does not reach down to a very low NmE value or that the height HST is found below the top of the E-valley. In such cases the parameter B_1, in the bottomside profile function (3.16a) is changed from 3 to 3.5 to 4 and finally 4.5 (see Figure 4). If HST cannot be found with these B_1 values, the gap between HZ and the E-valley top is closed by linear interpolation. The upper boundary of the intermediate region is defined by

$$HZ = (h_x + HST)/2 \qquad\qquad (3.23a)$$

with

$$h_x = \begin{cases} hmF1 & \text{if F1-layer is present} \\ hmF2 & \text{else} \end{cases} \qquad (3.23b)$$

Starting from HZ the profile is bent downward parabolically such that it meets the E-valley top h_{VT}. This is accomplished with the altitude transformation

$$h' - HZ = T/2 \pm (T^2/4 - T(h - HZ))^{1/2} \qquad (3.24a)$$

where

$$T = (HZ - HST)^2/(HST - h_\ell) \qquad\qquad (3.24b)$$

and

$$h_\ell = \begin{cases} h_{VT} & \text{if valley exists} \\ hmE & \text{else} \end{cases} \qquad (3.24c)$$

h_{VT} is the height at the top of the valley and hmE is the height of the E-peak.

3.2.5 E-Peak and Valley (h_{VT} to hmE)

The E-peak critical frequency is described by the model developed by Kouris and Muggleton (1973a, b) for CCIR (1973). It consists of four factors

$$foE^4 = A \cdot B \cdot C \cdot D \qquad\qquad (3.25a)$$

depending on the 12-months-running mean of the solar 10.7 cm radio flux (COV_{12}), on season (χ_{noon} is the solar zenith angle at noon), on geodetic latitude (φ), and on the solar zenith angle (χ).

$$A = 1 + 0.0094 \, (COV_{12} - 66) \qquad (3.25b)$$

$$B = \cos^m \chi_{noon} \qquad (3.25c)$$

$$m = \begin{cases} -1.93 + 1.92 \cos\varphi & \text{for } |\varphi| < 32° \\ 0.11 - 0.49 \cos\varphi & \text{for } |\varphi| \geq 32° \end{cases} \qquad (3.25d)$$

$$C = \begin{cases} 23 + 116 \cos\varphi & \text{for } |\varphi| < 32° \\ 92 + 35 \cos\varphi & \text{for } |\varphi| \geq 32° \end{cases} \qquad (3.25e)$$

$$D = \cos^n \chi_a \qquad (3.25f)$$

$$n = \begin{cases} 1.2 & \text{for } |\varphi| > 12° \\ 1.31 & \text{for } |\varphi| \leq 12° \end{cases} \qquad (3.25g)$$

Different from CCIR (1973), a modified zenith angle χ_a was introduced to improve the nighttime variation (Rawer and Bilitza, 1990).

$$\chi_a = \chi - 3 \; EPS_{-1} \, (\chi; \, 89.98, \, 3) \qquad (3.25h)$$

During all times foE is kept above or equal to the observed minimum value

$$foE_{min} = 0.121 + 0.0015 \, (COV_{12} - 66) \qquad (3.26)$$

A constant peak height $hmE = 105$ km is assumed for all conditions.

The F-region peak and valley profile is described by a fifth order power series

$$N(h)/NmE = 1 + E_1 \, x^2 + E_2 \, x^3 + E_3 \, x^4 + E_4 \, x^5 \qquad (3.27a)$$

with

$$x = h - hmE \qquad (3.27b)$$

Parameters E_1, E_2, E_3, and E_4 are determined from the valley width, HBR, the valley depth, DP, the distance between valley base and hmE, $HABR$, and the logarithmic derivative at the valley top, DLN. The parameter values listed in Table 4 were obtained from incoherent scatter measurements.

Table 4: Valley Parameters

		HABR/km	HBR/km	DP/%	DLN/km⁻¹	hmE/km
Mid-night	Modip = 18	28	45	81	0.06	105
	Modip = 45	28	67	81	0.06	105
Noon	Modip = 18	0	0	0	0	105
	Modip = 45	10.5	17.8	winter: 10 else: 5	summer: 0.01 else: 0.016	105

Notes: $DP = 100 (NmE - N_{VB})/NmE$; N_{VB} is the density at the valley base.

$DLN = \dfrac{d \ln N}{d h}\big|_{h = h_{VT}}$

Interpolation procedure is the same as indicated in Table 3 for B_0.

For the deep nighttime valley the power series is fitted to the logarithm of the electron density rather than to the density itself. At low and equatorial latitudes the valley feature has been observed irregularly during daytime, but not frequently enough to be included in a monthly average profile (e.g., Mahajan et al., 1990). In the case of zero valley depth (no valley), the F1-layer function is merged all the way down to hmE.

Since it appears quite irregularly, the sporadic E phenomenon is not incorporated in the IRI profile description.

3.2.6 D-Region and E-Bottomside (hmE to HA)

Most D-region profiles exhibit a characteristic inflection point with the height hmD and the density NmD. Mechtley and Bilitza (1974) found the following empirical relationship from rocket measurements (see also Bilitza, 1981a).

$$NmD/(10^8 m^{-3}) = (6.05 + 0.088 R_{12}) \exp(- 0.1/\cos^{2.7}\chi) \tag{3.28}$$

where R_{12} is the 12-months-running mean of the solar sunspot number and χ is the solar zenith angle. NmD is kept greater or equal to a minimum (nighttime) value of $4 \cdot 10^8 m^{-3}$.

The density profile starts at height HA and is represented by a third order polynomial (Mechtley and Bilitza, 1974; Bilitza, 1981a).

$$N(h)/NmD = \exp (F_1 x + F_2 x^2 + F_3 x^3) \tag{3.29a}$$

with

$$x = h - hmD \tag{3.29b}$$

Different F_3 parameters are used above (F_3^a) and below (F_3^b) the inflection point to account for the drastic change in scale height. The parameters

61

Table 5: D-Region Parameters

Time	Geographic Latitude	hmD/km	HA/km	F_1/km	F_2/km^2	$F_3{}^a$/km^3	$F_3{}^b$/km^3	hDX/km
Day	Low	80	65	0.02	$-2 \cdot 10^{-4}$	$9.37 \cdot 10^{-3}$	$4.89 \cdot 10^{-4}$	85.6
	Middle	80	65	0.05	$-1.25 \cdot 10^{-3}$	$8.18 \cdot 10^{-3}$	$1.707 \cdot 10^{-4}$	85.6
Night	All	88	80	0.05	$-1.25 \cdot 10^{-3}$	$8.79 \cdot 10^{-3}$	$1.22 \cdot 10^{-2}$	92.5

listed in Table 5 were obtained from the rocket measurements compiled by Mechtley and Bilitza (1974).

Somewhat arbitrarily an exponential function is used to connect the D-region profile with the E-layer peak density NmE and height hmE.

$$N(h)/NmE = \exp(-D_1 (hmE - h)^K) \qquad (3.30)$$

The parameters D_1 and K are determined such that the function agrees with the D-region profile function and its first derivative at the height hDX (see Table 5):

$$K = -DN (hmE - hDX)/(NDX \ln(NDX/NmE)) \qquad (3.31a)$$

$$D_1 = DN/(NDX \cdot K (hmE - hDX)^{K-1}) \qquad (3.31b)$$

NDX is the electron density at hDX and DN the derivative dN/dh at that height.

Comparisons with radio wave propagation data have resulted in several, sometimes conflicting, proposals for changes of the IRI D-region profile (Singer et al., 1984; Ferguson and McNamara, 1986; Pintado et al., 1987; Oyinloye, 1988). Since, however, these are all indirectly deduced profiles based on certain assumptions about the collision frequencies, additional experimental evidence is needed before IRI can be changed with confidence (Serafimov et al., 1985).

3.2.7 LAY Functions for Middle Ionosphere (hmE to $hmF2$)

A combination of four LAY functions (see section 3.1.2.2, page 48, Equation [3.5]) can be used to represent the electron density profile from the E- to the F2-peak in analytical form (Rawer, 1984, 1986, 1988; Suchy and Rawer, 1988).

$$\log(N(h)/NmF2) = \sum_{j=1}^{4} A_j \, LAY(h; hmF2, HX_j, SC_j) \qquad (3.32)$$

A preliminary set of parameters HX_j, SC_j is listed in Table 6 (Bilitza and Rawer, 1990). The amplitudes A_j are obtained automatically by least-square-fitting to the constraints listed in Table 7. All peak and valley parameters

Table 6: Parameters for the Four LAY Functions

	HX		SC
j	Day	Night	-
1	0.9 hmF2	$h_{0.5}$†	0.1204 $(hmF2-h_{0.5})$ + 56.8
2	hmF1*	$(hmF2+h_{VT})/2$	10
3	h_{VB}	h_{VB}	9
4	hmE-6	hmE	6

* $(hmF2 + h_{0.5})/2$, if F1-layer is not present.
† $h_{0.5}$ is the height, where $N(h) = 0.5\ NmF2$ (see Equation [3.17]).

Table 7: Constraints for LAY-Formalism

k					Weight	
Day	Night	*h*	*N*	d*N*/d*h*	Day	Night
1	1	$h_{0.5}$	0.5 NmF2	-	f††	1
2	2	h_{VT}	NmE	-	1	1
3	3	h_{VB}	N_{VB}	-	2	3
4	4	hmE	NmE	-	5	5
5	5	h_{BE}*	N_{VB}	-	1	0.5
6	-	hmF1	NmF1	-	3†	-
7	6	h_{VB}	-	0	50	50
8	7	hmE	-	0	500	500

* $h_{BE} = hmE - (h_{VB} - hmE)$.
† Zero, if F1-layer is not present.
†† f = EPS$_0$ (z; 0.15, 0.1)   with z = log $(N_{0.5}/NmF1)$ and $N_{0.5}$ = 0.5 NmF2.
   = 1   if F1-layer is not present.
   = 0.5   if $(NmF1 - N_{0.5})(hmF1 - h_{0.5}) < 0$.

are the same as those described for the standard IRI-90 profile, except for *hmF1* which is calculated with the widely used formula

$$hmF1/km = 165 + 0.6428\ x \qquad (3.33)$$

x is the solar zenith angle in degrees. Because there are more constraints (seven or eight) than free parameters (four), the degree to which the individual constraint is enforced will depend on the weight that is assigned to it during the fitting procedure. For more information and application to other parts of the density profile, see Rawer and Bilitza (1990).

3.2.8 Plasmaspheric Extension

Rycroft and Jones (1985, 1987) have developed a plasmaspheric extension for the IRI electron density model. Their diffusive equilibrium model describes the field-aligned distribution of plasma out to *L*-values of 6. A merging procedure with the IRI topside profile is suggested at a reference level near 650 km. This plasmaspheric extension is not yet included in IRI-90 but may be available from the authors.

3.2.9 Ionospheric Electron Content

McNamara (1983, 1984, 1985) has compared a large data base of total electron content (TEC) observations with the TEC values computed with IRI-79. He finds generally good agreement at midlatitudes; however, IRI-79 underestimated the TEC observed close to the magnetic equator by up to a factor of 2. The improved topside profile in IRI-86 helped to reduce this discrepancy to about 10% to 20%. Using the new option for the bottomside thickness parameter B_0 will further improve the agreement.

Application of IRI for satellite orbit determination was discussed by Bilitza et al. (1988) and by Coster et al. (1990). A recent comparison of IRI and TEC measurements is given in section 2.4, page 33, of this report.

3.3 Plasma Temperatures

The IRI-90 profiles for the electron and ion temperatures extend from 120 km to 1000 km. First order estimates can be obtained up to 3000 km; above 1000 km the two temperatures are assumed to coincide.

At the lower boundary, $HTA = 120$ km, thermal equilibrium is assumed between neutrals, ions, and electrons

$$T_e(HTA) = T_i(HTA) = T_n(HTA) \tag{3.34}$$

in accordance with most of the observations. Differences between electron and neutral temperatures at these low altitudes have been reported by Oyama et al. (1980).

With increasing altitude the electron temperature is always kept above (or equal to) the ion temperature, which in turn is kept above the neutral temperature

$$T_e(h) \geq T_i(h) \geq T_n(h) \tag{3.35}$$

Variations with solar activity are not explicitly included in the IRI-90 plasma temperature models. The above stated constraints (coupling to neutral temperature) can, however, cause solar activity variations when all temperatures are close together. In such cases, for example, at nighttime, the plasma temperatures vary with solar activity in the same way as the neutral temperature does. A review of observed and modeled solar activity variations of plasma temperatures was given by Bilitza and Hoegy (1990).

IRI uses the COSPAR International Reference Atmosphere (CIRA) as its neutral temperature model. The IRI computer code contains subroutines to calculate the CIRA (1972) temperatures. It is planned to incorporate the newly released CIRA (1986) model into IRI, as soon as an appropriately simplified version is available.

3.3.1 Electron Temperature

The development and improvement of the IRI electron temperature model was described by Bilitza (1981b, 1985b) and Bilitza et al. (1985). The electron temperature profile is subdivided into six regions defined by the region boundaries AHH_j ($j = 0$ to 6) as shown in Figure 5. Using Booker's (1977) approach, the temperature profile is approximated by a straight line in each region. Thus, the temperature can be described as (see section 3.1.2.1, page 46, Equation [3.3])

$$T_e(h) = ATE_0 + B(h; AHH_0, 5, ST, AHH, DTE) \tag{3.36a}$$

with the region gradients

$$ST_j = (dT_e/dh)_{j-1, j} = (ATE_j - ATE_{j-1})/(AHH_j - AHH_{j-1}) \tag{3.36b}$$

h / km

3000

BRACE,THEIS
(1981)

1400

BRACE,THEIS
(1981)

SPENNER,
PLUGGE
(1979)

600

400

300

200-270
120

T_e

CIRA   IRI-79

h / km

dT_e / dh
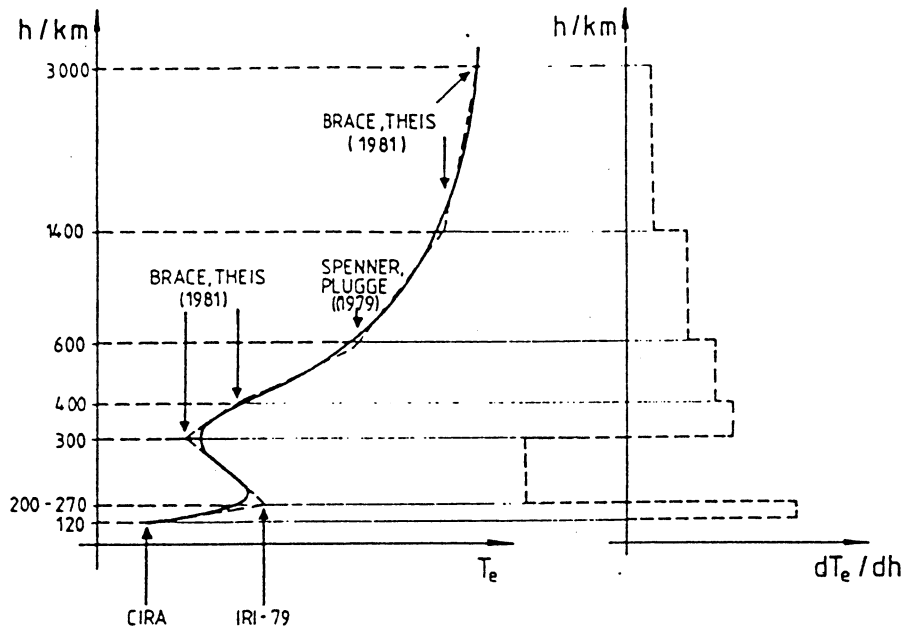
Fig. 5. Buildup of the IRI electron temperature model.

The region boundaries AHH_j, the electron temperatures ATE_j at these boundaries, and the transition thicknesses DTE_j are given in Table 8. If we

Table 8:   Electron Temperature Parameters

j	AHH_j/km	DTE/km	ATE_j	Source Model	Data Base	R_{12}*
0	120	-	T_n(120km)	CIRA (1986)	Incoherent scatter, satellites	T_n varies with R_{12}
1	h_m	5	TE_m	-	Incoherent scatter	60 - 120
2	300	5	TE_{BT}(300km)	Brace and Theis (1981)	AE-C	10 - 20
3	400	10	TE_{BT}(400km)		AE-C	20 - 50
4	600	20	TE_{SP}(600km)	Spenner and Plugge (1979)	AEROS	20 - 40
5	1400	20	TE_{BT}(1400km)	Brace and Theis (1981)	ISIS 2	40 - 70
6	3000		TE_{BT}(3000km)		ISIS 1	70 - 110

* R_{12} is 12-months-running mean solar sunspot number.

evaluate function (3.36) at the altitudes AHH_j, we find

$$T_e(AHH_j) - ATE_j = DSS_j \approx (ST_{j+1} - ST_j)\, DTE_j\, \ln(2) \qquad (3.37)$$

DSS_j describes the difference between the skeleton profile and the smoothed function at AHH_j. The ATE_j values are, however, well defined temperatures, which should be on the final profile. This can be accomplished to a good degree by introducing new temperatures

$$ATE_j^{(1)} = ATE_j - DSS_j \qquad (3.38)$$

and using these as the anchor points for the skeleton profile.

Table 8 lists also the source models used to obtain the temperature values ATE_j and the data base behind these models. Brace and Theis (1981) apply spherical harmonics analysis to describe their AE-C and ISIS satellite data in terms of magnetic dip latitude (Equation [3.11]) and local time. Sets of 81 coefficients are provided for equinox and solstice at 300 km, 400 km, 1400 km, and 3000 km. The model by Spenner and Plugge (1979) is based on AEROS satellite data and describes variations with geomagnetic latitude, longitude, and altitude. Two sets of coefficients are given, one for 3 a.m. local time and one for 3 p.m. (both for winter). Omitting the small longitudinal variation, Bilitza (1981b) obtained the following approximate expressions.

$$TE_{SP}\,(600\ \text{km},\ \phi)/K = \begin{cases} 2900{-}5600\ \text{EPS}_1\,(\phi;\ 0,\ 11.35) & \text{at 3 p.m.} \\ \text{EPSTEP}\,(\lvert\phi\rvert;\ 839,\ 2000,\ 45,\ 5) & \text{at 3 a.m.} \end{cases}$$
$$(3.39)$$

ϕ is the geomagnetic latitude in degrees. Local time variations are described with the day-night transition function explained in section 3.1.2.3, page 48 (Equation [3.6]).

During daytime at low latitudes, the temperature profile frequently exhibits a local maximum at about 270 km. The height h_m and temperature TE_m of this feature were obtained from incoherent scatter measurements.

$$h_m/\text{km} = 210 + 60\,\exp\left(-\,(\phi/22.4)^2\right) \qquad (3.40a)$$
$$TE_m/K = 1500 + 800\,\exp\left(-\,(\phi/33)^2\right) \qquad (3.40b)$$

During nighttime TE_m is set equal to the neutral temperature at $h_m = 150$ km.

The IRI model has been compared with a large number of rocket, satellite, and incoherent scatter radar measurements. In general good agreement was found; discrepancies are mostly due to the insufficient description of changes with season and solar activity (Bilitza and Hoegy, 1990; Buonsanto, 1989).

IRI offers a second option for the determination of the temperatures ATE_2, ATE_3, and ATE_4. They can be calculated with a model that makes use of the strong anti-correlation between electron temperature and density in the daytime ionosphere (Brace and Theis, 1978; Bilitza et al., 1985). In this case, users have to provide the electron density at the heights at which they choose to use this option (AHH_1, AHH_2, and/or AHH_3). The model by Brace and Theis (1978) describes the electron temperature in terms of electron density and altitude. It was extended by Bilitza et al. (1985) to include solar activity variations.

3.3.2 Ion Temperature

Similar to the electron temperature, the ion temperature profile is represented by a Booker-function

$$T_i(h) = ATI_0 + B(h; XSM_0, 3, STI, XSM, DTI) \qquad (3.41a)$$

with the gradients

$$STI_j = (ATI_j - ATI_{j-1})/(XSM_j - XSM_{j-1}) \qquad (3.41b)$$

the section boundaries XSM_j, the ion temperatures at these boundaries ATI_j, and the transition thicknesses DTI_j (see Table 9).

Table 9: Ion Temperature Parameters

j	XSM_j/km	ATI_j	DTI_j
0	HS	$T_n(HS)$	
1	430	TIM	10
2	HTT	$T_e(HTT)$	10
3	AHH_5*	ATE_5*	20
4	AHH_6*	ATE_6*	-

* If $HTT > AHH_5$, then $XSM_3 = AHH_6$ and $ATI_3 = ATE_6$. (AHH_j and ATE_j are electron temperature parameters defined in section 3.3.1, page 65, and Table 8.)

Incoherent scatter observations of ion temperature show a distinct change in gradient at about 430 km. Using AEROS satellite measurements the latitudinal variation of ion temperature at this point has been described as (Bilitza, 1981b)

$$TIM = \begin{cases} 1240 - 1400 \, EPS_1 \, (\phi; 0, 11.11) & \text{day} \\ 1200 - 300 \, \cos^{1/2} Z & \text{night} \end{cases} \qquad (3.42a)$$

with the geomagnetic latitude ϕ (in degrees) and

$$Z = 0.47 \, |\phi| + 0.024 \, \phi^2 \qquad (3.42b)$$

The height HS is found as the point on the neutral temperature profile, whose tangent meets the point (XSM_1/TIM). Below HS, $T_i = T_n$ is assumed.

HTT is the height at which the ion temperature profile meets the electron temperature profile, assuming a constant ion temperature gradient STI_2 above XSM_1. STI_2 is chosen as

$$STI_2 = \begin{cases} 3 & \text{day} \\ 0 & \text{night} \end{cases} \qquad (3.43)$$

based on incoherent scatter data. Above HTT, $T_i = T_e$ is assumed.

Comparisons with incoherent scatter data and with satellite measurements have indicated the need for a closer coupling between ion and neutral temperature at intermediate altitudes (Bilitza and Hoegy, 1990). See also Buonsanto (1989).

3.4 Ion Composition

IRI describes the relative percentage ion densities (ion composition) $R_{ion}(h)$; thus, the absolute ion densities are given by

$$N_{ion}(h) = N_e(h) \, R_{ion}(h) \qquad (3.44)$$

The model describes the percentage of O^+ and O_2^+ ions and fills up to 100% with light ions in the topside and with NO^+ ions at lower altitudes. A tenth of the light ions is assumed to be He^+, the rest H^+.

Booker's (1977) approach is used to represent the O^+ and O_2^+ profiles (see section 3.1.2.1, page 46). For O^+ ions the profile function reads (see Equation [3.3])

$$RO(h) = RO_0 \cdot \exp(\, B(h;\ HO_0,\ 4,\ MO,\ HO,\ DO)\,) \qquad (3.45)$$

with the thicknesses $DO_j = 9,\ 5,\ 5,\ 50$ km for $j = 1,\ 2,\ 3,\ 4$. At low altitudes the gradients MO_1, MO_2 and the transition heights HO_1, HO_2 were obtained from the compilation of rocket data (ion mass spectrometer) by Danilov and Semenov (1978). The variation of these parameters with solar zenith angle χ was approximated by the step function (3.2)

$$MO_1,\ MO_2,\ HO_1 = EPSTEP\ (z;\ A,\ B,\ z_s,\ d_z) \qquad (3.46)$$

where $z = \cos \chi$. Because of the limitations of the data base the model is restricted to sunlit hours. In IRI, z is set equal to 0 for χ greater than 90°. Parameters A, B, z_s, and d_z vary with season and solar activity as shown in Table 10. The topside part of the O^+ profile is yet relying on a very small data base of satellite data (AEROS, OGO 6; retarding potential analyzer). It distinguishes only day and night conditions and two latitude classes as listed in Table 11.

Only two Epstein functions are needed to represent the O_2^+ profile.

$$RO2(h) = RO2_0 \cdot \exp(\, B(h;\ HO2_0,\ 2,\ MO2,\ HO2,\ DO2)) \qquad (3.47)$$

with the transition thicknesses $DO2_1 = 5$ km and $DO2_2 = 5$ km and the gradients and transition heights as listed in Table 12.

The following adjustments are made automatically during the program execution:

(1) The height HO_3 is found where the upper O^+ skeleton profile (defined by the point $(HO_5/1\%)$, the transition height HO_4, and the gradients MO_4, MO_5) reaches 100%.

$$HO_3 = HO_4 + (\, \ln(100) - MO_5\ (HO_4 - HO_5))/MO_4 \qquad (3.48)$$

71

Table 10: Parameters for the Lower Part of the IRI O⁺ Model

		Winter	Summer COV < 100	Summer COV > 100	Equinox COV < 100	Equinox COV > 100
MO_1 %/km	A	0.13027	0.161	0.092	0.088	0.102
	B	0.08018	0.069	0.072	0.091	0.083
	z_s	0.25	0.18	0.21	0.34	0.03
	d_z	0.04216	0.254	0.014	0.008	0.045
MO_2 %/km	A	0.00999	0.0216	0.03863	0.0195	0.01
	B	-0.00686	0.0161	0.01389	0.0067	0.00127
	z_s	0.1	0.1	0.12	0.1	0.09
	d_z	5.113	0.03014	0.05762	0.04	0.05
HO_1 km	A	180	167	168	172	185
	B	170	152	165	158	167
	z_s	0.15	0.17	0.258	0.24	0.18
	d_z	0.1175	0.04916	0.008	0.01	0.015
HO_2/km		290	290	237	290	
HO_0/km		$(HO_2 + HO_3)/2$				
RO_0/%		100				

Table 11: Parameters for the Topside Part of the IRI O⁺ Model

	|Latitude| < 30 Day	|Latitude| < 30 Night	|Latitude| ≥ 30 Day	|Latitude| ≥ 30 Night
HO_4/km	695	570	695	575
HO_5*/km	2177	1040	3367	1380
MO_3/% km⁻¹	0			
MO_4/%km⁻¹	-0.000781	-0.002	-0.000786	-0.00126
MO_5/%km⁻¹	0.00264	-0.0052	-0.00165	-0.00524

* HO_5 is the height at which the percentage of O⁺ ions has decreased to 1%.

HO_3 has to be above HO_2 (see Table 10), which is the height at which the lower O⁺ skeleton profile reaches 100%. If HO_3 is below HO_2, then the gradient MO_4 is successively decreased by 0.001 km⁻¹ until HO_3 is above HO_2.

(2) Using the reference point $HO2_0//RO2_0$ and the gradients $MO2$ from Table 12, a new reference point is determined at the height $(HO2_2 + HO2_3)/2$ and used in Formula (3.47), thus making sure that the reference (anchor) point for the O_2^+ profile is not located in one of the transition regions (see section 3.1.2.1, page 46).

		Winter	Summer		Equinox	
			COV < 100	COV > 100	COV < 100	COV > 100
$\frac{HO2_1}{km}$	a	136	130	130	125	125
	b	-9	-10	-10	0	0
$\frac{HO2_2}{km}$	a	181	198	190	182	170
	b	-26	0	0	0	0
$\frac{MO2_1}{\%/km}$	a	0.02994	0.05922	0.05107	0.0307	0.02806
	b	-0.04879	-0.07983	-0.07964	-0.04968	-0.04716
$\frac{MO2_2}{\%/km}$	a	-0.01396	-0.00397	0.00097	-0.00248	-0.00066
	b	0.00089	0.00085	-0.01118	-0.02451	-0.02763
$\frac{MO2_3}{\%/km}$	a	-0.09929	-0.00313	-0.02614	-0.00313	-0.02247
	b	0.05589	0	-0.09537	0	-0.01919
$HO2_0$/km		140	160	140	140	140
$RO2_0$/%		45	31	30	37	37

Note: $\left.\begin{array}{c} HO2 \\ MO2 \end{array}\right\} = a + bz$ $z = \begin{cases} \cos x \\ 0 \text{ for } x > 90 \end{cases}$ x is solar zenith angle.

3) The height HO_{max} is determined where the O^+ profile function (3.45) reaches its maximum RO_{max}. If RO_{max} is greater than 100%, then RO_0 is reduced successively by 0.01%, until RO_{max} is less or equal to 100%. If at this altitude the percentage of O_2^+ ions (Function [3.47]) is larger than $100 - RO_{max}$, then the gradient $MO2_3$ is decreased successively by 0.02 km^{-1}, until the sum of O^+ and O_2^+ percentages is less than 100%.

(4) At the height HO_{max} the ratio

$$r = (100 - RO_{max} - RO2(HO_{max}))/RO2(HO_{max}) \qquad (3.49)$$

is determined and is used to calculate the percentage of NO^+ above HO_{max}. Herewith, interference between the molecular ion profiles and the light ion profiles is avoided.

Finally, the percentages of NO^+, H^+, and He^+ ions are determined:

$$RNO(h) = \begin{cases} 100 - RO(h) - RO2(h) & h \le HO_{max} \\ r\,RO2(h) & h > HO_{max} \end{cases} \qquad (3.50)$$

$$RH(h) = \begin{cases} (100 - RO(h) - RO2(h) - RNO(h))/(1-P) & h \ge HO_{max} \\ 0 & h < HO_{max} \end{cases} \qquad (3.51)$$

$$RHE(h) = RH(h)\,P/(1-P) \qquad (3.52)$$

$P = 0.1$ is the ratio of He^+ ions to the sum of all light ions (H^+ and He^+).

Comparisons with incoherent scatter data (Bilitza, 1984) with OGO 6 data (Kutiev et al., 1984a, b) and with ISS-b data (Goel and Rao, 1984) showed that IRI overestimates the percentage of light ions in the topside ionosphere. Discrepancies were also found at low altitudes in comparison with S3-1 satellite data (Philbrick and Bhavnani, 1983; Philbrick et al., 1984) and in comparisons with equatorial rocket data (Sridharan et al., 1985). A review of empirical ion composition modeling and of possible improvements of IRI was given by Bilitza (1990).

An alternative model was proposed by Danilov and Yaichnikov (1985). It describes the relative densities of O^+, H^+, He^+, NO^+, O_2^+, N^+, and Cluster ions in the altitude range from 75 km to 1000 km, taking into account variation with solar zenith angle, latitude, season, and solar activity. It is based on a compilation of satellite (Electron 2, 4, S3-1) and (high apogee) rocket data. IRI-90 offers this model as a second choice for the computation of the ionospheric ion composition. A listing of the computer code follows below.

```fortran
        subroutine ioncom(h,z,f,fs,t,cn)
c------------------------------------------------------------------
c ion composition model
c A.D. Danilov and A.P. Yaichnikov, A New Model of the Ion
c   Composition at 75 to 1000 km for IRI, Adv. Space Res. 5, #7,
c   75-79, 107-108, 1985
c
c       h          altitude in km
c       z          solar zenith angle in radians
c       f          latitude in radians
c       fs         10.7cm solar radio flux
c       t          season (month)
c       cn(1)      O+  relative density in percent
c       cn(2)      H+  relative density in percent
c       cn(3)      N+  relative density in percent
c       cn(4)      He+ relative density in percent
c       cn(5)      NO+ relative density in percent
c       cn(6)      O2+ relative density in percent
c       cn(7)      cluster ions  relative density in percent
c------------------------------------------------------------------
c
        dimension      cn(7),cm(7),hm(7),alh(7),all(7),beth(7),
     &                 betl(7),p(5,6,7),var(6),po(5,6),ph(5,6),
     &                 pn(5,6),phe(5,6),pno(5,6),po2(5,6),pcl(5,6)

        data po/4*0.,98.5,4*0.,320.,4*0.,-2.59E-4,2.79E-4,-3.33E-3,
     &          -3.52E-3,-5.16E-3,-2.47E-2,4*0.,-2.5E-6,1.04E-3,
     &          -1.79E-4,-4.29E-5,1.01E-5,-1.27E-3/
        data ph/-4.97E-7,-1.21E-1,-1.31E-1,0.,98.1,355.,-191.,
     &          -127.,0.,2040.,4*0.,-4.79E-6,-2.E-4,5.67E-4,
     &          2.6E-4,0.,-5.08E-3,10*0./
        data pn/7.6E-1,-5.62,-4.99,0.,5.79,83.,-369.,-324.,0.,593.,
     &          4*0.,-6.3E-5,-6.74E-3,-7.93E-3,-4.65E-3,0.,-3.26E-3,
     &          4*0.,-1.17E-5,4.88E-3,-1.31E-3,-7.03E-4,0.,-2.38E-3/
        data phe/-8.95E-1,6.1,5.39,0.,8.01,4*0.,1200.,4*0.,-1.04E-5,
     &          1.9E-3,9.53E-4,1.06E-3,0.,-3.44E-3,10*0./
        data pno/-22.4,17.7,-13.4,-4.88,62.3,32.7,0.,19.8,2.07,115.,
     &          5*0.,3.94E-3,0.,2.48E-3,2.15E-4,6.67E-3,5*0.,
     &          -8.4E-3,0.,-3.64E-3,2.E-3,-2.59E-2/
        data po2/8.,-12.2,9.9,5.8,53.4,-25.2,0.,-28.5,-6.72,120.,
     &          5*0.,-1.4E-2,0.,-9.3E-3,3.3E-3,2.8E-2,5*0.,4.25E-3,
     &          0.,-6.04E-3,3.85E-3,-3.64E-2/
        data pcl/4*0.,100.,4*0.,75.,10*0.,4*0.,-9.04E-3,-7.28E-3,
     &          2*0.,3.46E-3,-2.11E-2/

        DO 8 I=1,5
        DO 8 J=1,6
                p(i,j,1)=po(i,j)
                p(i,j,2)=ph(i,j)
                p(i,j,3)=pn(i,j)
                p(i,j,4)=phe(i,j)
                p(i,j,5)=pno(i,j)
                p(i,j,6)=po2(i,j)
                p(i,j,7)=pcl(i,j)
8       continue

        s=0.
```

```fortran
      do 5 i=1,7
          do 7 j=1,6
              var(j) = p(1,j,i)*cos(z) + p(2,j,i)*cos(f) +
     &                 p(3,j,i)*cos(0.013*(300.-fs)) +
     &                 p(4,j,i)*cos(0.52*(t-6.)) + p(5,j,i)
7         continue
          cm(i)  = var(1)
          hm(i)  = var(2)
          all(i) = var(3)
          betl(i)= var(4)
          alh(i) = var(5)
          beth(i)= var(6)
          hx=h-hm(i)
          if(hx) 1,2,3
1             cn(i) = cm(i) * exp( hx * (hx * all(i) + betl(i)) )
              goto 4
2             cn(i) = cm(i)
              goto 4
3             cn(i) = cm(i) * exp( hx * (hx * alh(i) - beth(i)) )
4         continue
          if(cn(i).LT.0.005*cm(i)) cn(i)=0.
          if(cn(i).GT.cm(i)) cn(i)=cm(i)
          s=s+cn(i)
5     continue
      do 6 i=1,7
6             cn(i)=cn(i)/s*100.
      return
      end
c
c
```

3.5 Ion Drift

A model of the ionospheric ion drift was developed for IRI-90 by Kazimirovsky and his colleagues based on ground-based drift measurements. It provides the horizontal E- and F-region drifts (zonal and meridional) for different geomagnetic latitudes, local times, seasons, and solar activities. The model is described in section 2.5, page 41, of this report. A listing of the computer code and coefficient files follows below. The program and coefficients may be available in computer-accessible form from the model authors.

A Computer Code for Determination VX, VY

```pascal
PROGRAM GLOB(INPUT,OUTPUT,FAR1,FAR2);
(*****************************************************************)
(*        TEST CALCULATION OF IONOSPHERIC DRIFTS GLOBAL MODEL    *)
(*****************************************************************)


  TYPE T1= ARRAY (.1..15.) OF REAL;
       T2= ARRAY (.0..10,0..23.) OF REAL;
  VAR  FAR1,FAR2: TEXT;
       BFAR : T1;
       DX,DY: T2;
       I,J,PMAX,REG,P : INTEGER;
       FI,LT,VX,VY : REAL;
       AR : ARRAY (.1..78,1..15.) OF REAL;



PROCEDURE DRIRR( REG,P : INTEGER; FI,LTT: REAL; VAR VX,VY : REAL );
  (*****************************************************************)
  (*        E.S.KAZIMIROVSKY,E.I.ZHOVTY AND M.A.CHERNIGOVSKAYA    *)
  (*    SIBERIAN INSTITUTE OF TERRESTRIAL MAGNETISM, IONOSPHERE AND  *)
  (*    RADIO WAVE PROPAGATION, SIBERIAN DERAPTMENT OF THE U.S.S.R,  *)
  (*    ACADEMY OF SCIENCES, 664033 IRKUTSK 33, P.O.BOX 4026,U.S,S,R,*)
  (*****************************************************************)
  (*        PROCEDURE CALCULATES ZONAL VX  AND MERIDIONAL VY      *)
  (*    COMPONENTS OF HORIZONTAL VELOCITY OF THE IONOSPHERIC      *)
  (*    IRREGULARITIES AT THE HEIGHTS OF E- AND F-REGION FOR PERIOD  *)
  (*    NUMBER P, GEOMAGNETIC LATITUDE FI(DEGR) AND LOCAL MEAN    *)
  (*    TIME LTT(HOUR), IN M/SEC.                                 *)
  (*                                                             *)
  (*    TO CALCULATE VX AND VY                                    *)
  (*      FOR E-REGION IT IS NECESSARY TO TAKE      REG=1         *)
  (*      FOR F-REGION                              REG=2         *)
  (*      FOR THE WHOLE PERIOD OF OBSERVATIONS                    *)
  (*                             (ONLY FOR F-REGION)       P=1    *)
  (*      FOR WINTER(FOR THE WHOLE PERIOD OF OBSERVATIONS) P=2    *)
  (*      FOR SPRING(FOR THE WHOLE PERIOD OF OBSERVATIONS) P=3    *)
  (*      FOR SUMMER(FOR THE WHOLE PERIOD OF OBSERVATIONS) P=4    *)
  (*      FOR AUTUMN(FOR THE WHOLE PERIOD OF OBSERVATIONS) P=5    *)
  (*      FOR WINTER( F 10.7 = 200 )                       P=6    *)
  (*      FOR SPRING( F 10.7 = 200 )                       P=7    *)
  (*      FOR SUMMER( F 10.7 = 200 )                       P=8    *)
  (*      FOR AUTUMN( F 10.7 = 200 )                       P=9    *)
  (*      FOR WINTER( F 10.7 =  70 )                       P=10   *)
  (*      FOR SPRING( F 10.7 =  70 )                       P=11   *)
  (*      FOR SUMMER( F 10.7 =  70 )                       P=12   *)
  (*      FOR AUTUMN( F 10.7 =  70 )                       P=13   *)
  (*                                                             *)
  (*    IF THERE IS NO DATA THEN    VX=VY=9999.9                  *)
  (*                                                             *)
  (*    VX > 0 TO EAST, VY > 0 TO NORTH                          *)
  (*****************************************************************)
  (* SEE "ADV.SPACE RES," VOL.5,#7,95,109(1985), VOL.8,#4,239(1988)*)
  (*        FOR A DESCRIPTION OF THE ORIGINAL WORK.              *)
  (*****************************************************************)
  (*        THIS VERSION OF MODEL IS WRITTEN IN  PASCAL 8000     *)
  (* SEE "PASCAL 8000. REFERENCE MANUAL (VERSION 2.0)",          *)
  (*****************************************************************)
```

```
BEGIN (* DRIRR *)
  RA:=PI/12;   RAD:=PI/180;
   (* CHECKING THE CONDITIONS OF INFORMATION AVAILABILITY *)
  LT:=LTT;
 :IF LT>24 THEN  BEGIN    LT:=LT-24; GOTO 13   END;
  IF (FI>60) OR (FI<10) THEN GOTO 11;
  K:=(P-1)*6+TRUNC(FI/10);
  P1:=TRUNC(AR(.K,15.));
  CASE REG OF
  1: IF (P1=0) OR ((P1=1) AND ((LT<6) OR (LT>18))) THEN GOTO 11;
  2: IF (P1=0) OR ((P1=1) AND ((LT>6) AND (LT<18))) THEN GOTO 11
  END; (* CASE REG *)
  IF TRUNC(FI/10)=TRUNC((FI-1)/10+1) THEN
    BEGIN (* 1 *)
      FOR I1:=1 TO 2 DO
        BEGIN
          I2:=(I1-1)*7;
          V0:=AR(.K,I2+1,); V1:=AR(.K,I2+2.); V2:=AR(.K,I2+3,);
          V3:=AR(.K,I2+4.); F1:=AR(.K,I2+5.); F2:=AR(.K,I2+6.);
          F3:=AR(.K,I2+7,);
          CASE I1 OF
          1: VX:=C(LT,V0,V1,V2,V3,F1,F2,F3);
          2: VY:=C(LT,V0,V1,V2,V3,F1,F2,F3)
          END  (* CASE I1 *)
        END  (* I1 *)
    END  (* 1 *)
  ELSE
    BEGIN (* 2 *)
      P11:=TRUNC(AR(.K+1,15.));
      CASE REG OF
      1: IF (P11=0) OR ((P11=1) AND ((LT<6) OR (LT>18)))
         THEN GOTO 11;
      2: IF (P11=0) OR ((P11=1) AND ((LT>6) AND (LT<18)))
         THEN GOTO 11
      END; (* CASE REG *)
         (* FILLING OF THE ARRAY F *)
      FOR I1:=1 TO 2 DO
        BEGIN
          I2:=(I1-1)*7;
          FOR I3:=1 TO 6 DO
            BEGIN
              J:=(P-1)*6+I3;
              V0:=AR(.J,I2+1,); V1:=AR(.J,I2+2.); V2:=AR(.J,I2+3.);
              V3:=AR(.J,I2+4.); F1:=AR(.J,I2+5.); F2:=AR(.J,I2+6.);
              F3:=AR(.J,I2+7.); F(.I3-1.):=C(LT,V0,V1,V2,V3,F1,F2,F3)
            END; (* I3 *)
          (* THE LATITUDINAL INTERPOLATION OF VELOCITY *)
          CASE I1 OF
          1: VX:=SPF(PI/18,FI*RAD);
          2: VY:=SPF(PI/18,FI*RAD)
          END  (* CASE I1 *)
        END
    END; (* 2 *)
  GOTO 12;
11:VX:=9999.9;  VY:=9999.9;
12:.
 END;  (* DRIRR *)
```

```pascal
LABEL 11,12,13;
CONST PI=3.1415926;
VAR K,P1,I1,I2,I3,I,J,P11: INTEGER;
    LT,RA,RAD,V0,V1,V2,V3,F1,F2,F3: REAL;
    F: ARRAY (.0..5.) OF REAL;


FUNCTION SPF( HX,X: REAL ): REAL;
   (*  FUNCTION CALCULATES SPLINE INTERPOLATION OF      *)
   (*  LATITUDINAL VARIATION                            *)
   LABEL 14;
   VAR  G,Q,R,Z : ARRAY (.0..5.) OF REAL;
        M,KSI,NJ : ARRAY (.0..6.) OF REAL;
        A,B : ARRAY (.0..4.) OF REAL;
        I,IO : INTEGER;
        X0,X1 : REAL;
   BEGIN (* SPF *)
      G(.0.):=0;  R(.5.):=0; G(.5.):=1;  R(.0.):=1;
      Z(.0.):=3*(F(.1.)-F(.0.))/HX;
      Z(.5.):=3*(F(.5.)-F(.4.))/HX;
      FOR I:=1 TO 4 DO
        BEGIN
          G(.I.):=0.5;  R(.I.):=0.5;
          Z(.I.):=3*(R(.I.)*(F(.I+1.)-F(.I.))/HX+
                  G(.I.)*(F(.I.)-F(.I-1.))/HX)
        END;
      FOR I:=0 TO 5 DO  Q(.I.):=-2;
      KSI(.0.):=0; NJ(.0.):=0;
      FOR I:=0 TO 5 DO
        BEGIN
          KSI(.I+1.):=R(.I.)/(Q(.I.)-KSI(.I.)*G(.I.));
          NJ(.I+1.):=(NU(.I.)*G(.I.)-Z(.I.))/(Q(.I.)-KSI(.I.)*G(.I.))
        END;
      M(.6.):=0;
      FOR I:=5 DOWNTO 0 DO  M(.I.):=KSI(.I+1.)*M(.I+1.)+NU(.I+1.);
      FOR I:=0 TO 4 DO
        BEGIN
          A(.I.):=-2*(F(.I+1.)-F(.I.))/HX+(M(.I.)+M(.I+1.));
          B(.I.):=-A(.I.)+(F(.I+1.)-F(.I.))/HX-M(.I.)
        END;
      FOR I:=0 TO 5 DO
        BEGIN
          IF (X>=(10*RAD+HX*I)) AND (X<(10*RAD+HX*(I+1))) THEN
             BEGIN   X1:=X; IO:=I; GOTO 14 END;
        END;
   14:X0:=X1-HX*IO-10*RAD;
      SPF:=F(.IO.)+M(.IO.)*X0+B(.IO.)/HX*X0**2+A(.IO.)/(HX*HX)*X0**3
   END; (* SPF *)


FUNCTION C(JJ,C0,C1,C2,C3,FI1,FI2,FI3 : REAL) : REAL;
   (*   FUNCTION CALCULATES THE VALUE OF VELOCITY FOR  *)
   (*   THE LATITUDINAL NET POINTS                     *)
   BEGIN
      C:=C0+C1*SIN(RA*JJ+FI1*RAD)+C2*SIN(2*RA*JJ+FI2*RAD)+
         C3*SIN(3*RA*JJ+FI3*RAD)
   END; (* C *)
```

```pascal
PROCEDURE NAME(REG,P: INTEGER);
    (*   PROCEDURE PRINTS THE NAME OF THE PERIOD FOR      *)
    (*   DIFFERENT REG AND P                              *)
    VAR II: INTEGER;
    BEGIN
      CASE REG OF
        1: WRITE('       E REGION      ');
        2: WRITE('       F REGION      ')
      END; (* CASE REG *)
      IF                           (REG=2) AND (P=1 ) THEN II:=0;
      IF (REG=1) AND (P=1 ) OR (REG=2) AND (P=2 ) THEN II:=1;
      IF (REG=1) AND (P=2 ) OR (REG=2) AND (P=3 ) THEN II:=2;
      IF (REG=1) AND (P=3 ) OR (REG=2) AND (P=4 ) THEN II:=3;
      IF (REG=1) AND (P=4 ) OR (REG=2) AND (P=5 ) THEN II:=4;
      IF (REG=1) AND (P=5 ) OR (REG=2) AND (P=6 ) THEN II:=5;
      IF (REG=1) AND (P=6 ) OR (REG=2) AND (P=7 ) THEN II:=6;
      IF (REG=1) AND (P=7 ) OR (REG=2) AND (P=8 ) THEN II:=7;
      IF (REG=1) AND (P=8 ) OR (REG=2) AND (P=9 ) THEN II:=8;
      IF (REG=1) AND (P=9 ) OR (REG=2) AND (P=10) THEN II:=9;
      IF (REG=1) AND (P=10) OR (REG=2) AND (P=11) THEN II:=10;
      IF (REG=1) AND (P=11) OR (REG=2) AND (P=12) THEN II:=11;
      IF (REG=1) AND (P=12) OR (REG=2) AND (P=13) THEN II:=12;
      CASE II OF
        0:WRITELN('   THE WHOLE PERIOD OF OBSERVATIONS');
        1:WRITELN('   WINTER(FOR THE WHOLE PERIOD OF OBSERVATIONS)');
        2:WRITELN('   SPRING(FOR THE WHOLE PERIOD OF OBSERVATIONS)');
        3:WRITELN('   SUMMER(FOR THE WHOLE PERIOD OF OBSERVATIONS)');
        4:WRITELN('   AUTUMN(FOR THE WHOLE PERIOD OF OBSERVATIONS)');
        5:WRITELN('   WINTER( F 10.7 =  200 )');
        6:WRITELN('   SPRING( F 10.7 =  200 )');
        7:WRITELN('   SUMMER( F 10.7 =  200 )');
        8:WRITELN('   AUTUMN( F 10.7 =  200 )');
        9:WRITELN('   WINTER( F 10.7 =   70 )');
        10:WRITELN('   SPRING( F 10.7 =   70 )');
        11:WRITELN('   SUMMER( F 10.7 =   70 )');
        12:WRITELN('   AUTUMN( F 10.7 =   70 )');
      END (* CASE II *)
    END; (* NAME *)


  PROCEDURE TABLE;
    (*   PROCEDURE PRINTS THE TABLE OF CALCULATED VALUES *)
    (*   OF DRIFT VELOCITYES VX AND VY  FOR EVERY        *)
    (*   HOUR FROM 00LT TILL 23LT FOR LATITUDES 5,10,15, *)
    (*   ...,60 DEG.                                     *)
    VAR I,J: INTEGER;
    BEGIN (* TABLE *)
      WRITELN('      ZONAL VELOCITY  VX (M/S)');
      WRITELN;WRITE(' ');FOR J:=1 TO 91 DO WRITE('*');WRITELN;
      WRITE(' FI  LT');FOR J:=1 TO 12 DO WRITE((J-1):7);WRITELN;
      WRITE(' ');FOR J:=1 TO 91 DO WRITE('*');WRITELN;
      FOR J:=0 TO 10 DO
        BEGIN
          WRITE(' ',(60-J*5):2,'        ');
          FOR I:=0 TO 11 DO WRITE(VX(.10-J,I.):7:1);WRITELN
        END;
      WRITE(' ');FOR J:=1 TO 91 DO WRITE('*');WRITELN;
      WRITE(' FI  LT');FOR J:=1 TO 12 DO WRITE((J+11):7);WRITELN;
      WRITE(' ');FOR J:=1 TO 91 DO WRITE('*');WRITELN;
```

```pascal
      FOR J:=0 TO 10 DO
      BEGIN
         WRITE(' ',(50-J*5):2,'        ');
         FOR I:=12 TO 23 DO WRITE(DX(.10-J,I.):7:1);WRITELN
      END;
      WRITE(' ');FOR J:=1 TO 91 DO WRITE('*');WRITELN;WRITELN;
      WRITELN('        MERIDIONAL VELOCITY  VY (M/S)');
      WRITELN;WRITE(' ');FOR J:=1 TO 91 DO WRITE('*');WRITELN;
      WRITE(' FI   LT');FOR J:=1 TO 12 DO WRITE((J-1):7);WRITELN;
      WRITE(' ');FOR J:=1 TO 91 DO WRITE('*');WRITELN;
      FOR J:=0 TO 10 DO
         BEGIN
            WRITE(' ',(50-J*5):2,'        ');
            FOR I:=0 TO 11 DO WRITE(DY(.10-J,I.):7:1);WRITELN
         END;
      WRITE(' ');FOR J:=1 TO 91 DO WRITE('*');WRITELN;
      WRITE(' FI   LT');FOR J:=1 TO 12 DO WRITE((J+11):7);WRITELN;
      WRITE(' ');FOR J:=1 TO 91 DO WRITE('*');WRITELN;
      FOR J:=0 TO 10 DO
         BEGIN
            WRITE(' ',(50-J*5):2,'        ');
            FOR I:=12 TO 23 DO WRITE(DY(.10-J,I.):7:1);WRITELN
         END;
      WRITE(' ');FOR J:=1 TO 91 DO WRITE('*');WRITELN;WRITELN
   END; (* TABLE *)

BEGIN    (* GLOBMOD *)
  VX:=0;VY:=0;
  FOR REG:=1 TO 2 DO
     BEGIN
        FOR I:=1 TO 15 DO  FOR J:=1 TO 78 DO  AR(.J,I.):=0;
        CASE REG OF
          1: BEGIN
               (* INPUT THE INITIAL DATA FOR E-REGION *)
               RESET (FAR1);
               FOR J:=1 TO 72 DO
                  BEGIN
                     FOR I:=1 TO 15 DO READ (FAR1,BFAR(.I.));
                     FOR I:=1 TO 15 DO  AR(.J,I.):=BFAR(.I.)
                  END
             END; (* REG1 *)
          2: BEGIN
               (* INPUT THE INITIAL DATA FOR F-REGION *)
               RESET (FAR2);
               FOR J:=1 TO 78 DO
                  BEGIN
                     FOR I:=1 TO 15 DO READ (FAR2,BFAR(.I.));
                     FOR I:=1 TO 15 DO  AR(.J,I.):=BFAR(.I.)
                  END
             END (* REG2 *)
        END; (* CASE *)

        CASE REG OF
          1: PMAX:= 12;
          2: PMAX:= 13;
        END;
```

```
FOR P:=1 TO PMAX DO
    BEGIN
        PAGE;
        NAME(REG,P);
        FI:=5;
        FOR J:=0 TO 10 DO
            BEGIN
                FI:=FI+5;
                FOR I:=0 TO 23 DO
                    BEGIN
                        LT:=I;
                        ORIRR(REG,P,FI,LT,VX,VY);
                        DX(.J,I.):=VX; DY(.J,I.):=VY
                    END (* I *)
            END; (* J *)
        TABLE
    END (* P *)
END (* REG *)
END. (* GLOBMOD *)
```

83

```
7.8  36.7  21.0  15.7  324.9  297.9  21.0  -6.2  34.0  15.3  14.9  282.9  267.0  228.0  2
-15.5   5.8  36.2  13.2  241.0  255.0  75.0  -38.0   5.3  12.3   5.7  226.0  221.0  153.0  2
-18.3  23.6   0   45.7   0   -3.0  30.4   0  343.6   0  1
-42.6  13.5   2.8   8.9  242.0  152.5  307.9  -57.9  15.0  47.6  11.7  197.0  36.3  251.0  2
-9.0  12.0   8.0   4.4  284.9  259.8  56.5  -15.5   4.5   7.2   1.5  254.0  48.4  32.7  2
-38.0  56.0  28.8  20.0  76.0   5.4  244.0  -24.8  17.9  30.1   1.8  179.0  352.0  44.0  2
35.3   6.9   0   0  269.0  -19.0  39.9   0  173.0   0  1
29.7  15.6  12.2  10.9  106.0  213.0  93.0  -28.2  14.8  13.4   9.2  174.0  94.0  342.9  2
12.5  10.3  16.2  12.2  80.9  213.3  37.1  -9.2   6.5  16.7  11.6  263.7  92.4   1.4  2
18.8  32.1  13.2   2.3  163.8  213.8  62.1  -5.7  21.5  32.4  13.4  253.8  170.1  356.9  2
8.5   4.9  14.2   7.8  174.0  210.7  44.1  -2.4  12.2  17.5   6.8  185.9  154.2  19.5  2
-16.8  59.5  28.7  32.5  73.0  38.0  214.0  -52.9  87.6  17.2  230.0  200.0  274.9  266.0  2
20.6  17.6   1.9   8.5  353.0   3.2  321.9  -25.7  12.8   2.6   7.1  72.4   4.6  31.8  2
17.2  33.0  15.7   6.6  180.0  214.0  352.9  -25.9  16.6   9.6  18.8  169.0  51.0   1.0  2
10.3  13.0  12.2   9.0  160.1  189.7  35.5  -5.1   4.8   8.7   1.8  155.3  94.4  328.9  2
20.6  27.2  23.4   9.5  181.7  155.3  168.0  14.1  28.8  44.3   7.0  165.3  156.0  64.6  2
19.5  14.9   8.0   3.7  172.3  190.8  21.1   4.7   9.3   1.3  181.6  132.1  24.5  2
11.2   8.1   1.9  11.0  177.2  180.8  197.2  168.3   6.5   4.3   3.8  167.4  108.3  31.9  2
-3.2  24.3  19.5  17.3  332.9  282.9  123.3  -35.3  18.0   7.9  110.0  183.0   6.0  2
-13.0  13.1  28.7   6.1  142.0  182.9  134.8  -34.8  19.9  27.2   8.8  218.0  95.0  356.9  2
3.7   8.0   9.2   3.7  245.8  193.9  43.6  -18.7   6.4  19.8   8.0  334.1  58.9  348.7  2
-35.5  28.1   0   0  161.1  119.6  10.3  -7.5   0  8.4   0  2
-11.2  35.4  22.1  21.1  335.9  320.9  21.1  -2.9  12.2  27.0  196.1  91.7  336.4  2
-9.2   0   0  65.0  8.2  15.0  286.6   0  1
-1.2  12.0  35.0   0  344.1  0  -4.3  0  -9.2  35.0  21.8   7.0  287.9  270.9  239.0  2
-28.3  36.8  14.8  15.8  53.0  -24.1  72.6  0  171.0   0  1
-9.3  27.2  29.6   7.2  250.0  210.7  68.0  -28.4  11.8  20.6   8.6  216.6  89.7  326.5  2
-43.1  37.7   0   6.4  306.9  6.4  55.4  -12.0   0  173.0  11.9  187.0  12.5  215.0  2
35.3   6.9   0   0  269.0  -19.0  39.0   0  173.0   0  1
31.4  22.5  24.1  17.0  45.0  239.0  115.0  -34.2   8.8  13.4  174.0  149.0  62.0  2
-9.8  11.4  27.1  12.2  349.9  306.9  37.0  -7.2   8.4  22.8  195.0  67.0  342.9  2
8.8   1.8  20.3   4.1  233.0  182.2  60.0   2.2  22.2  207.0  40.9  347.9  2
10.4   5.1   6.2   5.5  203.0  175.9  84.0  11.8  16.7   3.7  165.0  151.3  72.0  2
23.5  42.9   0  113.0  -11.3   0  32.4   0  292.1   0  1
```